The Birth of PICL: New Laboratory Experiments for Understanding Ocean Worlds

Thesis by
William Thomas Plent Denman

In Partial Fulfillment of the Requirements for the
Degree of
Doctor of Philosophy in Chemistry

Caltech

CALIFORNIA INSTITUTE OF TECHNOLOGY
Pasadena, California

2024
Defended March 29th, 2024

© 2024

William Thomas Plent Denman
ORCID: [0000-0003-4752-0073]

All rights reserved

ACKNOWLEDGEMENTS

I would like to thank my parents, William "Pepper" Denman and Stephanie Plent, for their support; for providing me with the resources and encouragement to continuing my academic endeavors, for not telling me that the school didn't think I would graduate high school and always supporting my science. I want to thank my father for building an innate curiosity within me and always trying to figure out how things work. I want to thank my mother for her advice and the countless hours of edits starting in 4th grade until the culmination of this thesis. She has read more rough drafts than either of us can count. Thank you for allowing me to fail and helping me to get back up. To my sister, Laura, thank you for encouraging me to step out of the family business and for being a sounding board for my future. I would like to thank my grandfather, Alan Plent, for fueling my artistic endeavors; I wish he could see some of my terrible CAD diagrams. To my grandmother, Margaret-Love Denman, thank you for all the edits and reminding me to keep my PhD in context; here's to getting the union card. Thank you to the rest of my family, to those who are here and no longer here, especially Uncle John for being part of the limited West Coast contingency.

Thank you to my advisor, Mike Brown, for taking a gamble on a chemist. His support and guidance have made me a better scientist. I want to thank him for allowing me to explore new questions and at times keeping me focused on the questions at hand. Thank you for allowing me to try new things and allowing these things to fail. Thank you to the past and present members of the Brown group for tolerating my planetary ignorance and helping me learn. While we have been through many iterations of group meeting, they have continued to be a highlight of graduate school. I would like to thank Geoff Blake for the intellectual and professional guidance and having someone to talk sports with. I would also like to extend a thank you to the Planetary science office, especially Ruth Loisel, whose support made this PhD possible.

This PhD would not have been possible without the support of numerous friends who have visited over the years and the trips we have taken. To my non-Caltech Pasadena friends, thank you for the bike rides and trips and getting me out of the bubble. I would like to extend gratitude to the Caltech Men's Soccer team for giving me a team for my first three years here and the triathlon club for giving me a team for the next three. None of this would have been possible without the support of my partner, Hayley Bates. We met at a time of utter world wide chaos and I don't think

we have ever looked back from there. Thank you for all the support and the belief.

ABSTRACT

A laboratory set up was built analogous to that of the environment of the Galilean system. Previous work has focused on vapor deposition and shied away from bulk samples which more closely resemble the surface of Europa. The focus of this research has been the relationship between laboratory data to observational spectra collected. Data from various telescopes has given an indication of the species which exist on the surface of Europa. Linear spectral modeling has not been effective in identifying these species due to a lack of viable candidates. Chapter 2 focuses on the instrumentation and sample preparation for the laboratory set up. In Chapter 3 data is presented on the irradiation of sodium chloride at Europa like conditions and the features that arise with cryogenic irradiation. This data is compared to observational data from HST and provides strong evidence for the presences of sodium chloride (NaCl) on Europa's leading hemisphere. Chapter 4 presents FTIR and UV/VIS data for the irradiation of sulfate salts suspected to be present on Europa. This presents one of the first instances of cyrogenic electron irradiation of sulfates compared to new data from JWST. Mechanisms for the trapping of carbon dioxide at both Europa and Ganymede have also been investigated. These experiments are paramount for understanding the composition of Europa's ocean and can be utilized by the Europa Clipper team. Future experiments involving laboratory spectroscopy of carbon dioxide trapping are also highlighted. The use of cyrogenic gamma irradiation experiments and their feasibility are explored.

PUBLISHED CONTENT AND CONTRIBUTIONS

1. Denman, W. T. P., Chandra, S. & Brown, M. E. Laboratory evidence for Sulphates. *[Manuscript]* (2024).
   W.T.P.D participated in the formulation of the project, constructed the instrumentation, collected the spectra, prepared the data, and participated in the writing of the manuscript.

2. Denman, W. T. P., Trumbo, S. K. & Brown, M. E. The Influence of Temperature and Photobleaching on Irradiated Sodium Chloride at Europa-like Conditions. *The Planetary Science Journal* **3,** 26. doi:`10.3847/PSJ/ac4581` (Feb. 1, 2022).
   W.T.P.D participated in the formulation of the project, constructed the instrumentation, collected the spectra, prepared the data, and participated in the writing of the manuscript.

TABLE OF CONTENTS

LIST OF ILLUSTRATIONS

LIST OF TABLES

NOMENCLATURE

Bremsstrahlung. Braking Radiation. The electromagnetic radiation produced by the deceleration of a charged particle when deflected by another charged particle.

Galilean System. The four largest moons of Jupiter discovered by Galileo including Io, Europa, Ganymede, and Callisto.

Raman Spectroscopy. Used to determine the vibrational modes of molecules via Raman Scattering of an incident beam.

Roentgen. Non-SI unit of exposure for gamma irradiation converted to $2.58 \times 10^{-4}\,\mathrm{C/kg}$. Commonly used for Roentgen Equivalent Man (REM) when dealing with effective dosage.

Chapter 1

INTRODUCTION

1.1 Europa Background

Jupiter's Magnetosphere

Jupiter's strong magnetic field creates the unique environment in which the Galilean satellites exist. The magnetospheric plasma of Jupiter corotates with the planet at close to a 10-hour spin period. This magnetospheric plasma flows over the satellites from the trailing hemispheres and sweeps ahead of them. Europa's mean orbital radius is 9.4 RJ and is tilted relative to Jupiter's equator. Because Jupiter's magnetic dipole is tilted, Europa makes excursions from the spin plane. The energy spectrum of Jupiter's magnetosphere is most easily divided into two categories: the plasma range and the single-particle approach. The plasma range — in this instance the 'cold' plasma — can be studied with magnetohydrodynamic (MHD) approximation. Under this theory, the plasma is thought to flow like a fluid onto and around an object. The second category, when energies are roughly keV energies, the individual particle motions are significant, so a single-particle approach is better suited. Part of this single-particle approach comes about from the increased gyroradius with increased energy. In this region, more energetic particles are sensitive to spatial gradients of the magnetic field. Charged particles have three principal motions in the inner magnetosphere: gyration about the field lines, the bounce along the field lines and longitudinal motion. Due to gradient curvature drift, ions flow slightly faster than the plasma while electrons travel slower. At 25 MeV, the gradient-curvature drift of the electrons becomes comparable to the drift caused by the magnetic field, known as E X B [1]. As the gradient curve drift surpasses that of the drift from the magnetic field, the motion of the electrons becomes opposite to the path of both Europa and the plasma. All charged particles, except 25 MeV and greater electrons, impact from the trailing side to the leading side of Europa.

Europa's Plasma Environment

The electron density at Europa's orbital distance spans between 12 to 250 cm^{-3} [2]. The number of protons between 50-200 KeV near Europa is about one-thousandth the total plasma density. Europa's location within Jupiter's Magnetosphere and Io's torus creates a unique radiolytic environment at Europa's surface. The ejection of species from Io's surface are ionized by collisions with Jupiter's magnetic field. These charged particles either undergo collisions in the magnetosphere and become energetic neutral particles or remain as ions. The ions impacting Europa are made up of predominately sulfur, oxygen, and protons. The sulfur to oxygen ratio is 2 to 1 due to the dominant species coming from Io's volcanism being SO_2. There also exists a large number of electrons of varying energies which interact with Europa's surface. The electrons and their positively charged compatriots have preferential interaction with Europa's surface based on charge, mass and energy. This creates a difference in the surface chemistry between Europa's leading and trailing hemisphere. The spatial distribution of the bombardment is determined by the plasma's rate of flow past the satellite and by the velocities of the plasma particles relative to the local magnetic field lines [3]. The thermal plasma ions typically have gyroradii smaller than the satellite reading and preferentially impact the satellite's trailing hemisphere. Energetic ions with significant velocities along the field lines or with gyroradii similar to Europa's dimensions can bombard the entire surface. For electrons, the energy of interaction is between 10 to 30 eV with 2-10 % being hot electrons at 250 eV. The energy of ions is between 50 to 500 eV with the major ions being [S^{++}] and [O^{+}] [4]. This data was collected by various Galileo and Voyager transits within the plasma sheet. It presents a good indication of the energy of bombardment present on Europa's surface.

Flux at Europa

The energy imparted on the surface of Europa differs for the trailing and the leading sides. The total average flux is 78×10^{12} eV cm^{-2} s^{-1} [5], as based on data collected via the Galileo Orbiter. The dose rate observed at Europa can be predicted from the near upstream region of the plasma environment. The dose rate decreases versus depth but is not linear and differs for different impact species. The average power per unit area, in W m^{-2}, at the surface for ions between 10 keV and 10 MeV is $P_P = 0.012$, $P_{OX} = 0.0025$, and $P_{Su} = 0.0048$ [4]. The energy for electrons across the same energy range is $P_e = 0.057$. This calculation does not include the more energetic ions which would increase energy at the surface by roughly 15%. The range of impacts of the higher energy ions are more asymmetric than the low energy ions. The difference in the trailing and leading side bombardment is important while the mechanism for the preferential bombardment is not discussed in this work. High energy electrons (above 25 MeV) have preferential bombardment of the leading hemisphere due to their anti-rotation to the plasma disk. Protons with energies of 100 eV and below impact all positions on Europa while higher energy protons are preferential to the trailing side of Europa due to their path within the corotating plasma disk. For sulfur, 1 keV energy ions heavily favor the trailing hemisphere with some reaching the leading hemisphere [3]. At higher energies, there is some leading-hemisphere asymmetry for sulfur, though to a lesser degree. Sulfur implantation rates on the trailing side are an order of magnitude higher than that of the leading hemisphere [6]. Sulfur bombardment is key as an energy source and has importance for sulfate chemistry. The exogenic implantation of sulfur to the surface drives many of the reactions on the surface. Low energy electrons as well as sub 100 keV protons are capable of hitting the polar regions of Europa. This creates significantly less radiolytic reactions in the polar regions compared to equatorial positions. Majority of energy imparted on the surface of Europa comes from electrons. Electrons impact the moon close to the point of intersection between the moon and the guiding center field lines [7]. Higher energy electrons that fall below the 25 MeV threshold are centered around the equatorial regions of the trailing hemisphere between 60° latitude north and south. This, in conjunction with ion bombardment, creates what is known as the 'bulls-eye' pattern on the trailing equatorial region of Europa. Lower energy electrons (less than 20 keV) are capable of intersecting Europa's polar regions. These differing energies and impact locations cause unique surface features on Europa. They also provide us with differing spectroscopic features on the surface.

The radiation penetration depth differs greatly depending on the incident object. Attempting to mimic the irradiation environment of Europa requires special consideration of the depth of penetration. To first order approximation, the energetic ions and the electrons lose their energy to the solid by producing excitations and ionization. Ions also lose energy by momentum transfer collisions to atoms in the solid. The two points of interest are (1) the stopping power, which is total energy loss per unit path length and (2) the dose vs. depth, dose being the energy per unit volume. The second order reactions are as follows: knock-on collisions which set atoms in motion, ionizations which produce electrons as well as excitations, and bremsstrahlung photons. These photons are created as the kinetic energy of the electrons is decreased, thus causing a release of energy. This bremsstrahlung energy is released as a photon which penetrates further within the ice lattice due to its smaller size. These second order reactions greatly increase the depth of penetration. The immediate surface layer, around 0.01 μm, is dominated by the corotating thermal plasma ions and low energy electrons. At meter depths, the energy is dominated by bremsstrahlung gamma-rays produced by higher energy electrons [4]. Because of the spatial variation of incident collisions, dose vs. depth differs greatly. The leading hemisphere and polar regions will have dose rates 1000 times smaller at 0.1 mm when compared to the trailing hemisphere. The charge state of the incident O and S ions affects their interaction. If the total kinetic energy of the ion is compared to the energy needed to fully ionize the ion, on the order of a few keV for O and S, then the ion will only penetrate the first few microns of ice. The larger the ion the shallower the penetration depth.

Surface

The surface of Europa is marked by intense radiation bombardment, regions of turn over, and cracks which mar its surface. The surface is composed of a mixture of both crystalline and amorphous water ice with a number of constituents in smaller fractions [8]. The surface temperature on Europa is between 80 to 130 K based on location and time of day. Observations from NIMS show disrupted and chaotic terrain on Europa, which exhibits distorted and asymmetric absorption features. These absorption features suggest a number of differing constituents. One of the major components is that of hydrate water ice which produces a distorted feature. Various salts, as well as radiolytic products have been observed. This mixture of both exogenic and endogenic species paints an interesting picture of Europa's landscape. The exogenic and iogenic species are present in the magnetosphere and can alter the endogenic species of Europa. The purest H_2O is found on the leading hemisphere while the trailing hemisphere contains the highest concentration of the next most prevalent species, a hydrated material of unknown composition. The water ice on the leading side is amorphous on the upper surface, with crystalline ice present at submillimeter depths. The trailing hemisphere contains water ice as well as hydrated components of varying origin. The hydrated components are thought to be derived from ocean brine and exogenic implantation. Radiolytic products are also present on both the trailing and leading hemispheres. The ability to characterize subsurface ocean fluids will rely on understanding these endogenic components' expression on the surface. The periodic resurfacing of Europa via processes like spreading, rifting, subduction, and cryovolcansim gives great insight into the ocean [9]. These processes bring material from the ductile ice layer up to the brittle crust of the surface. Regions that are geologically young and exhibit many changes are known as 'Chaos Regions'. These chaos regions have not undergone the intense bombardment that other parts of the surface have. This is due to the higher rate of turnover at these sections. This turnover indicates that these regions are most likely endogenic and can offer insight into the subsurface ocean. The chaos regions of the leading hemisphere are predicted to be spectroscopically different from the icy high latitudes of the leading hemisphere as well as the altered terrain of the trailing hemisphere [10]. The young regions on the leading hemisphere are shielded from sulfur implantation and may be the best representation of Europa's endogenous material [11]. The polar regions and distinct features, like lineae, are also of interest. Both these locations possess unique spectroscopic features. Early spectroscopy from the Galileo spacecraft NIMS instrument suggested that the surface was hydrated sulfate salts [12]. Further study of the NIMS data indicated that hydrated sulfuric acid [13] could also account for the spectra. Sulfuric acid is an expected species on the surface as a product of bombardment. Due to its relationship to iogenic species, the sulfuric acid would have a preferential appearance on the trailing hemisphere [4]. The issue with the NIMS data was that it lacked sufficient spectral resolution to identify distinct spectral features. This led researchers to turn to ground-based adaptive optics. By measuring the depth of the 2.0 µm water absorption feature, one can infer the proportion of icy to non-icy material. The spectra showed that the low latitude trailing hemisphere contains the largest fraction of non-water ice. The low latitude leading hemisphere also contains a significant amount of non-icy material but less than that of the trailing hemisphere. The high-altitude regions have the highest abundance of water ice. The higher resolution data focused on the low latitudes of the trailing side and the bright low latitude of the leading hemisphere. A feature at 2.07 µm was observed in the equatorial spectra of the trailing hemisphere but not observed in either the leading hemisphere or the polar spectra of the trailing hemisphere. This would indicate that it is created by strong irradiation. This 2.07 µm feature correlates well with locations on the trailing hemisphere that have non-water ice components as well as UV absorption from Voyager that have been attributed to the presence of radiolytic SO_2. The sulfur allotropes involved in the radiolytic sulfur cycle (H_2SO_4, SO_2, S, and H_2S) do not possess the 2.07 µm absorption feature. This feature has been attributed to either $MgSO_4$ brine or its hydrated counterpart, Epsomite ($MgSO_4 \cdot 7\,H_2O$), which is forming via an analogous magnesium radiation cycle alongside the radiolytic production of sulfuric acid [14]. While further investigation of magnesium hydrates is needed, the presence of this peak alludes not to a sulfate dominated ocean but one composed of other salts. There have not been observations of magnesium sulfate absorption in regions that do not undergo sulfuric bombardment. Magnesium sulfates on the surface could indicate endogenic magnesium in the subsurface ocean and could represent the presence of a magnesium radiolytic cycle on the surface.

The chaos regions mentioned above are believed to be of salty composition, most recently suggested as chloride salts [11]. This is due to the smooth spectra they produce at infrared wavelengths. Alkali chlorides are further confirmed as the likely candidate due to their spectral features in the visible wavelength range under particle irradiation. These salts develop ‘color centers’ due to anion vacancies in the crystal structures under bombardment. Color centers are light absorption bands that correspond to electronic transitions in the defects in the crystal lattice caused by irradiation. The simplest color center is an F center, which corresponds to an electron trapped in an anion vacancy. For NaCl, this is a monovalent Cl anion vacancy. Under certain conditions aggregation of F centers can occur creating binary, ternary, and quaternary F centers referred to as M, R, and N centers, respectively. Larger defects and dislocations can occur under intense irradiation within the crystal lattice. More recent studies have shown the presence of a 450 nm peak that can be attributed to irradiated NaCl on the surface of Europa [15, 16]. This is due to the formation of the F center within the lattice. This 450 nm feature is exclusively on the leading hemisphere and correlates to chaos terrain, with the largest absorption feature being found in Tara Regio. This terrain is sheltered from sulfur radiolysis and is thought to be dominated by endogenous material [11]. The distribution of the signal was found to be separate from sulfur radiolysis. The presence of endogenous NaCl and thus a chloride dominate subsurface ocean would suggest hydrothermal oceanic circulation [17].

Subsurface Ocean

One of the more fascinating aspects of Europa is its subsurface ocean. The intense bombardments from Io and Jupiter’s magnetosphere cause sputtering and radiolytic chemistry on the surface. The variability of the impacts and the underlying surface create differing spectroscopic regions. By measuring the different surface regions, we are able to infer the underlying composition. Data from Galileo suggest that Europa possesses a roughly 150 km thick ice crust and a rocky interior [18]. A large salty subsurface ocean exists between the ice sheet and the rock core. This is unique when compared to other celestial bodies. The majority of planetary subsurface oceans reside between two layers of varied water ice types. Where as on Europa there is interaction between Europa’s silicate rock core and its subsurface ocean. Via erosion mechanisms, minerals are transported into the ocean and this creates a chemical gradient which has only been observed previously on Earth. The surface of Europa exhibits blocks of different texture which appear to have moved and rotated while maintaining some older topological features [18]. The mechanism for the movement of ice sheets is not fully known but the gaps between blocks are most likely of different composition. The gaps are believed to be subsurface ocean or viscous ice. The lineae, which crisscross Europa, suggest that there is tidal deformation of the outer ice shell. These lineae are expressed in a darker color than the surrounding ice indicating a differing composition. In some instances, striations cross blocks indicating that they are newer geolocical features. Some linea possess dark red portions which would be indicative of even more recent resurfacing. This linea could be endogenic species from the subsurface ocean. This fact, coupled with Europa's reliable tidal heat source, may lead to activity at the silicate-ocean boundary layer. This interaction can produce reductants while the intense bombardment that occurs on Europa surface produces oxidants.

1.2 Radiolytic Chemistry

The combination of reductants from the subsurface ocean and impingement of electrons and ions creates radiolytic chemistry on the surface of Europa. Hydrogen peroxide H_2O_2 has been observed on the surface. Hydrogen peroxide was found to be preferential to low altitudes on the leading side and correlated to chaos terrain [19]. Hydrogen peroxide is important for radiolytic reactions on Europa and may be a source of oxidants for the subsurface ocean. Both the destruction of hydrogen peroxide and the creation of hydrogen peroxide has been studied via irradiation [20–22]. The presence of sulfuric acid (H_2SO_4) has also been confirmed spectroscopically [14]. It has also been produced experimentally with Europa analogous conditions [23]. The presence of sulfuric acid suggests a sulfur cycle occurring at Europa with radiolysis of water species. Carbon dioxide has recently been observed on Europa's surface [24]. Its production has been hypothisized as endogenic but radiolysis may play a role in its location and longevity. The delivery of metal cations, like calcium, sodium, and magnesium, in large quantities is not observed at Europa. If these elements are present at the surface they are most likely endogenous and transported from the subsurface ocean. The interaction with species on the surface via radiolytic cycles greatly changes their spectroscopic features.

1.3 Tying Observations to Experiments

Throughout this thesis mention will be made of the previous and ongoing fantastic observational work conducted by current and former members of the Brown Group. There is also a myraid of observational data from telescopes that has been collected by other members of the scientific community. Visible spectra is used from the Hubble Space Telescope using the Space Telescope Imaging Spectrograph [11]. NIR to mid IR data was collected by the Galileo Near Infrared Mapping Spectrometer (NIMS) spanning from 0.7 to 5.2 µm. This data has been processed and reduced on multiple occasions and continues to provide new insights. Ground-based observations from NIRSPEC on the Keck II telescope provided hemispherically resolved spectra from 3.1 to 4.13 µm [15]. This offered an in depth look at the 3.78 µm band which is highlighted in Chapter 4. New data from the James Webb Space Telescope (JWST) has provided higher resolution spectroscopy as well as data in ranges previously unavailable. Data from Trumbo & Brown [24] was the impetus behind the experimental design in Chapter 5.

References

1. *Europa* (eds Pappalardo, R. T., McKinnon, W. B. & Khurana, K. K.) (University of Arizona Press, Dec. 15, 2017). doi:`10.2307/j.ctt1xp3wdw`.
2. Kivelson, M. G. *et al.* Magnetospheric Interactions with Satellites, 24.
3. Pospieszalska, M. & Johnson, R. Magnetospheric ion bombardment profiles of satellites: Europa and Dione. *Icarus* **78,** 1–13. doi:`10.1016/0019-1035(89)90065-1` (Mar. 1989).
4. Paranicas, C., Ratliff, J. M., Mauk, B. H., Cohen, C. & Johnson, R. E. The ion environment near Europa and its role in surface energetics. *Geophysical Research Letters* **29,** 18–1–18–4. doi:`10.1029/2001GL014127` (2002).
5. Moore, M. IR Detection of H2O2 at 80 K in Ion-Irradiated Laboratory Ices Relevant to Europa. *Icarus* **145,** 282–288. doi:`10.1006/icar.1999.6325` (May 2000).
6. Johnson, R. E. & Leblanc, F. Energy Distributions for Desorption of Sodium and Potassium from Ice: The Na/K Ratio at Europa, 7.
7. Paranicas, C. *et al.* Europa's near-surface radiation environment: EUROPA'S NEAR-SURFACE RADIATION ENVIRONMENT. *Geophysical Research Letters* **34.** doi:`10.1029/2007GL030834` (Aug. 2007).
8. Dalton, J. B. Linear mixture modeling of Europa's non-ice material based on cryogenic laboratory spectroscopy. *Geophysical Research Letters* **34.** doi:`https://doi.org/10.1029/2007GL031497` (2007).
9. Johnson, P. V., Hodyss, R., Vu, T. H. & Choukroun, M. Insights into Europa's ocean composition derived from its surface expression. *Icarus* **321,** 857–865. doi:`10.1016/j.icarus.2018.12.009` (Mar. 2019).

10. Fischer, P. D., Brown, M. E. & Hand, K. P. SPATIALLY RESOLVED SPECTROSCOPY OF EUROPA: THE DISTINCT SPECTRUM OF LARGE-SCALE CHAOS. *The Astronomical Journal* **150,** 164. doi:`10.1088/0004-6256/150/5/164` (Oct. 30, 2015).
11. Trumbo, S. K., Brown, M. E. & Hand, K. P. Sodium chloride on the surface of Europa. *Science Advances* **5,** eaaw7123. doi:`10.1126/sciadv.aaw7123` (June 2019).
12. McCord, T. B. *et al.* Non-water-ice constituents in the surface material of the icy Galilean satellites from the Galileo near-infrared mapping spectrometer investigation. *Journal of Geophysical Research: Planets* **103,** 8603–8626. doi:`10.1029/98JE00788` (E4 Apr. 25, 1998).
13. McCord, T. B. *et al.* Hydrated salt minerals on Europa's surface from the Galileo near-infrared mapping spectrometer (NIMS) investigation. *Journal of Geophysical Research: Planets* **104,** 11827–11851. doi:`10.1029/1999JE900005` (E5 May 25, 1999).
14. Brown, M. E. & Hand, K. P. SALTS AND RADIATION PRODUCTS ON THE SURFACE OF EUROPA. *The Astronomical Journal* **145,** 110. doi:`10.1088/0004-6256/145/4/110` (Mar. 14, 2013).
15. Trumbo, S. K., Brown, M. E., Fischer, P. D. & Hand, K. P. A New Spectral Feature on the Trailing Hemisphere of Europa at 3.78 *micro* m. *The Astronomical Journal* **153,** 250. doi:`10.3847/1538-3881/aa6d80` (May 11, 2017).
16. Hand, K. P. & Carlson, R. W. Europa's surface color suggests an ocean rich with sodium chloride. *Geophysical Research Letters* **42,** 3174–3178. doi:`10.1002/2015GL063559` (2015).
17. Kargel, J. S. *et al.* Europa's Crust and Ocean: Origin, Composition, and the Prospects for Life. *Icarus* **148,** 226–265. doi:`10.1006/icar.2000.6471` (Nov. 2000).
18. Carr, M. H. *et al.* Evidence for a subsurface ocean on Europa. *Nature* **391,** 363–365. doi:`10.1038/34857` (Jan. 1998).
19. Trumbo, S. K., Brown, M. E. & Hand, K. P. H$_2$O$_2$ within chaos terrain on Europa's leading hemisphere. *The Astronomical Journal* **158,** 127. doi:`10.3847/1538-3881/ab380c` (Aug. 27, 2019).
20. Loeffler, M., Raut, U., Vidal, R., Baragiola, R. & Carlson, R. Synthesis of hydrogen peroxide in water ice by ion irradiation. *Icarus* **180,** 265–273. doi:`10.1016/j.icarus.2005.08.001` (Jan. 2006).
21. Loeffler, M. J., Teolis, B. D. & Baragiola, R. A. Decomposition of solid amorphous hydrogen peroxide by ion irradiation. *The Journal of Chemical Physics* **124,** 104702. doi:`10.1063/1.2171967` (Mar. 10, 2006).

22. Kumagai, Y. Decomposition of hydrogen peroxide by gamma-ray irradiation in mixture of aqueous solution and Y-type zeolite. *Radiation Physics and Chemistry* **97,** 223–232. doi:`10.1016/j.radphyschem.2013.12.006` (Apr. 2014).

23. Loeffler, M., Hudson, R., Moore, M. & Carlson, R. Radiolysis of sulfuric acid, sulfuric acid monohydrate, and sulfuric acid tetrahydrate and its relevance to Europa. *Icarus* **215,** 370–380. doi:`10.1016/j.icarus.2011.06.008` (Sept. 2011).

24. Trumbo, S. K. & Brown, M. E. The distribution of CO_2 on Europa indicates an internal source of carbon. *Science* **381,** 1308–1311. doi:`10.1126/science.adg4155` (Sept. 22, 2023).

Chapter 2

INSTRUMENTATION

2.1 Introduction

A significant portion of the work for this thesis was constructing the Planetary Icy Chemistry Laboratory (PICL) at the California Institute of Technology. Construction began in January of 2020 with multiple iterations occurring over the the past four years. This section is focused on the current iteration of the instrument highlighting the building and troubling shooting of the physical instrument, as well as the sample preparation methods to utilize similar instrumentation.

2.2 UHV System

The majority of the experiments present in this thesis were conducted in a high vacuum system. The main chamber is a Kimball Physics 4.5" Spherical Cube expanded version. This geometry allows for additional 1.33" input ports as compared to the previous 4.5" Spherical cube. These ports are used for the addition of a residual gas analyzer (RGA), additional fiber optic UV/VIS spectroscopy, and a camera. To keep the system carbon free an Agilent Dry Scroll ID3 roughing pump is connected to an Agilent TwisTorr 84 $\mathrm{l\,s^{-1}}$ turbo molecular pump. This pump is slightly oversized for the volume of our chamber, with the internal volume of the chamber being 2838 cc. Since we perform in-situ measurements on bulk samples compared to vapor deposition on cold plates, the system is opened up between each run. Having an over-sized pump allows for us to get back down to working pressures faster. The turbo is directly mounted to the chamber, thereby increasing conductance, as compared to connection via a set of bellows. All flanges, excluding the access door, are ConFlat (CF) with oxygen-free high thermal conductivity (OFHC) gaskets. This is common practice with UHV systems. This system is able to maintain vacuum of 10^{-7} torr without cryogenic cooling and below 10^{-9} torr when maintaining below 10 K. This is in the transition range between high vacuum and ultra-high vacuum. At this range the gas is in free molecular flow resulting in collisions occurring with the walls of the chamber, not between gas molecules. The pressure is measured using an Agilent FRG-700 Full RangePirani Inverted magnetron Gauge. These base pressures were achieved without performing a bake out and the system is periodically leak tested with various solvents. When the vacuum system is not running the access hatch is either closed or a positive pressure of nitrogen is run into the chamber. This decreases condensation within the system and limits frosting with cryogenic cooling. We have observed oxidation of the copper gasket on the base port of the chamber due to interaction with salt samples. When bringing the system back up to atmospheric pressure, purged nitrogen is flowed into the system which can cause the sample to be blown out of the sample cup and into the chamber. The interaction causes the formation of copper oxides which can limit the ultimate vacuum that can be maintained. This problem was easily mitigated with leak testing and replacement of the bottom gasket.

2.3 Irradiation

Due to Jupiter's magnetosphere the Galilean satellites undergo intense electron and ion bombardment. This bombardment creates spectroscopic features which allow for identification of the compound. To mimic this environment we have used two different forms of irradiation.

Electron Irradiation

As mentioned in the section on Europa Background (1.1) majority of the chemistry at Europa's surface occurs via secondary electrons. Accelerators are able to produce similar high energy electrons to those observed in Jupiter's magnetosphere but these electrons are not the main drivers of chemistry. The secondary electrons that are produced by these high energy electrons are predicted to be around 10 keV [1]. These secondary electrons also have an increased penetration depth into the ice shell. Our experiments are focused on the spectroscopy and chemical changes that these secondary electrons cause. For our electron irradiation we utilize a Kimball Physics EGG-3101C which can produce electrons between 100 eV and 10 keV via a Tantalum cathode. Electrons are emitted from the cathode and then accelerated via a wehnelt (Grid) and a grounded anode. The beam is then further focused via an einzel lens and a 4-pole deflection unit. Our cathode is a refractory thermionic emitter which is directly heated by the voltage source. The high temperature of the cathode requires vacuum to prevent oxidation. The wehnelt or grid is a tubular structure that houses the cathode and has an aperture fixed at one end. If the potential of the wehnelt is increased the aperture becomes more negative compared to the cathode, and the electric field between the cathode and the wehnelt increases. This suppresses electron emission from the cathode perimeter. This grid potential is used to shut the beam on and off while maintaining cathode temperature and is used for beam alignment. Adjusting the grid voltage varies the electron trajectory. We utilize the grid voltage to create an electron pattern that fully covers our sample. Post the cathode, a Einzel lens is used to focus the beam. It consists of three tubes of equal diameter with two tubes being grounded and the middle tube having variable current. The negative focusing potential of the center tube controls the position of the beams second axial crossover point. We operate at a working distance of 320 mm with a spot size of 10 mm. As noted in the previous (1.1) section majority of the energy imparted to the surface of the Galilean moons is from electron impingement. Our 10 keV electrons are at varied source voltages from 1 to 500 nA as measured by a Faraday cup. We only utilize up to 10 keV electrons because at higher electron energies X-rays are produced, meaning other precautions are needed. At our electron energy range the majority of the spectroscopic changes are due to the secondary or Bremsstrahlung electrons. The lower energy electrons that we utilize mimic the effect of the secondary electrons produced by the high energy electrons present at Europa. We are also able to generate higher electron fluxes than those observed on some portions of Europa. Current estimations place electron impingement on Europa at $1.89 \times 10^{-4}\,\mathrm{ev/16amu/minute}$ [2] where our range of irradiation is from 4.84×10^{-3} to $2.62\,\mathrm{eV/amu/minute}$. This allows us to produce the equivalent thousands of years of irradiation on Europa in minutes. Due to the energy of the electrons we cannot produce the same penetration depth or sputtering as occurring in the Galilean system. Even with this decreased penetration depth and limited secondary electrons spectroscopic changes are observed. Electron sample impingement is measured with a Kimball Physics faraday cup. The faraday cup measures the number of electrons hitting the cup thus producing a current. This current is measured in nanoamperes (nA). By using the electron energy, the area of the faraday cup, and this measured current we calculate the irradiation occurring. I designed and machined a custom adapter for our faraday cup to allow it to be placed into the electron beam path via a linear actuator. A phosphorus screen is installed with an opening for the faraday cup. The phosphorus screen glows when electrons hit its surface and therefore can be used for alignment and shaping of the beam. The phosphorus screen is imperative because the cathode produces a thermal glow when emitting electron. The thermal glow does not align with the electron path since it is not effected by the alignment mechanisms. Differentiating between the signal from the thermal glove and the signal for the electrons can be difficult when aligning. The phosphorus screen makes it possible to see the beam size and the alignment.

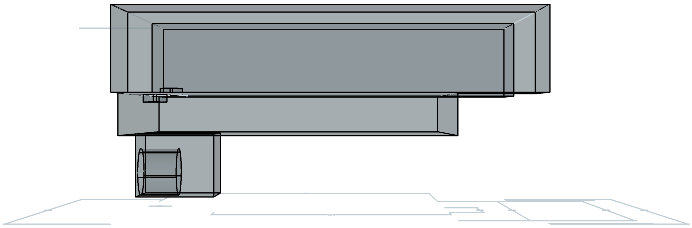

Figure 2.1: A sideview of the schematic for the custom adapter built to allow for the faraday cup and phosphorus screen. The bottom section is notched to interface with the linear actuator. The two step design allows for centering the faraday cup above the sample cup.

Gamma Irradiation

The diverse irradiation environment at Europa can be simulated with various methods including gamma irradiation. Gamma irradiation is used to simulate long term irritation on Europa. Salt response with gamma irradiation has been studied but this was focused on applications for the storage of nuclear waste [3, 4]. In relation to Europa, gamma exposure studies focuses on spacecraft missions and maintaining instrument integrity in the caustic environment of space [5].

Gamma decay is a nuclear decay mechanism which is the relaxation of an element from its excited state to a lower state. This relaxation culminates in the release of energy either as a photon or packet of energy. For our experiments we utilized Cesium-137 decay. The majority of Cs-137 (94.6%) decays via beta emission to metastable Barium-137m which then undergoes further decay to ground state Barium-

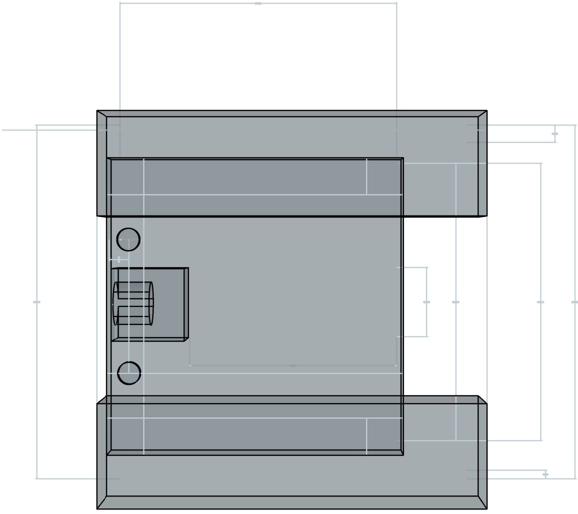

Figure 2.2: A schematic of the the custom adapter built to allow for the faraday cup and phosphorus screen. The faraday cup sits in between the two stations with the phosphorus screen on top.

137. Barium-137m decays to the ground state via emission of photons at 0.6617 MeV. This emission is distinctly different from electron irradiation and causes different spectroscopic changes.

2.4 Spectroscopy

For comparison to observational data our instrument uses two unique spectroscopic methods. We utilize the ultraviolet (UV) and visible (VIS) wavelengths, and the infrared (IR) region of electromagnetic region. These two regions use distinct detectors and sources.

UV/VIS

Many of the suspected salts present on Europa exhibit no spectral features in the UV and visible wavelengths. This makes identification of various species difficult via observational astronomy. However, many of these same species when irradiated

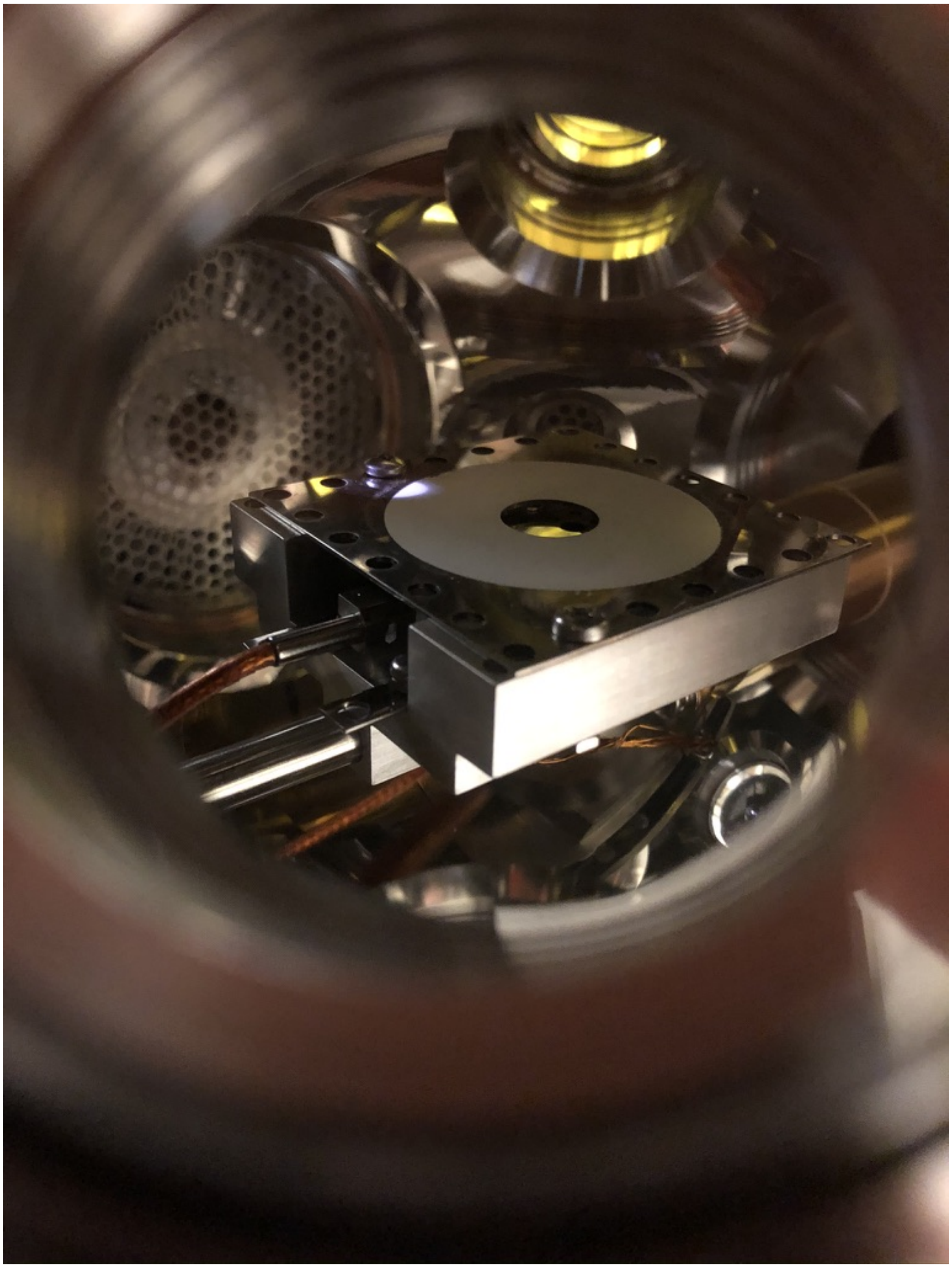

Figure 2.3: Phosphorus screen (white screen mounted on steel plate) above the faraday cup in the sample chamber.

develop distinct absorption features. The wavelength position and intensity of these changes are dependent on temperature and radiolytic conditions. These spectroscopic changes allow us to identify potential species and then compare our laboratory work to observational work collected by the Hubble Space Telescope. [6, 7]. The laboratory spectra is collected using a diffuse reflectance geometry. The sample is illuminated at 45° from the surface normal and the diffuse reflection is collected at 90° from the specular direction and 45° from the surface normal. This removes spectral reflections but decreases our signal. This geometry is akin to that of telescopes, with our lamps being the sun and the collection lens the telescope. Two different optical standard were used for the UV/VIS experiments. Labsphere Spectralon® and Polytetrafluoroethylene (PTFE) are used for background division. PTFE powder is ground and packed into a sample cup before being place in the chamber. It does not have the same organic absorption that is present in Spectralon ® since there is no binding agent. Neither Spectralon or PTFE can be used in vacuum due to out-gassing. This has little effect on the spectroscopic signal since standard atmosphere does not have adsorptions in the UV/Vis wavelengths used.

Lamps

UV illumination is provided by a Thorlabs SLS204 deuterium lamp. This provides continuous UV spectrum from 200 to 400 nm via gaseous deuterium. The deuterium is excited via an electrical arc causing molecular emission. These bulbs are replaceable and a decrease in signal is observed when the end of the lifetime is reached. The distinct deuterium peak is observed at 656 nm, making the data redward of this point inconsistent due to saturation issues. The visible portion of the spectra is provided by a Thorlabs SLS201L. This provides continuous spectra from 360 to 2800 nm with similar shape to blackbody irradiation at 2796 K. Signal is provided by a tungsten-halogen filament with replaceable bulb. The light is coupled via SMA fiber patch.

Previously we used a Y-splitter and ran both UV and visible spectroscopy simultaneously. This caused issues with our UV signal due to the fiber used after recombination within the Y-splitter being rated for visible light but having poor transmission of UV. We instead now run a single fiber from each lamp to the focusing lens. The fibers are swapped based on the wavelength range being collected. For the collection of the diffuse reflection, a lens is tethered to a fiber optic cable which runs directly into our spectrometer. We collect spectra for each each wavelength range from the two lamps and then the resulting spectra are spliced together. Due to the loss of light at 360 nm from the visible lamp the stitching is done at approximately 380 nm. The detector recognizes counts sub 360 nm for the visible lamp meaning this region shows incorrect absorption features when compared to the UV absorption spectra. This issue was found to occur within the dark spectra and was not linear with exposure time. For some of our spectra we observed an absorption at 216 nm. This feature has been attributed to our copper sample cups and slight misalignment of the input beam. Due to the diffuse reflectivity geometry of our set up and the high reflectivity of copper the spectral reflection of the copper surface was not observed.

Detector and Data Processing

The UV/VIS spectral range is collected with a StellarNet Inc Black Comet SR spectrometer with a range from 200 to 1080 nm. It utilizes a dual blaze 40 mm diameter concave grating with aberration correction. It is a mirror free construction and the concave grating produces a flat field on the CCD detector for uniform resolution. A focusing lens is coupled to a SMA905 fiber. We observed corrections occurring in the provided StellarNet software as well as limited export capabilities, so instead created a python script and interface that produced .FITS files. FITS files allow information to be stored in the headers of the files for characterization and multiple spectra to be stored in the same file. This is the same file format that many telescopes use thus allowing for easier manipulation and comparison. All data processing is done manually post collection. Files were dark subtracted and then divided by reference spectra as either unirradiated cryogenic salt or one of the optical standards, Spectralon and PTFE.

IR

Infrared spectroscopy spans a large range of electromagnetic energy and is focused on the vibrations of molecular bonds. IR spectroscopy is used extensively for the identification of molecules and observing the distinct vibrations. In observational astronomy and planetary science, the IR light is used extensively both for ground-based and space-based telescopic observations. The W.M. Keck Observatory on Mauna Kea in Hawaii and the James Webb Space Telescope (JWST) are the predominate telescopes used by our group to observe the Galilean System. Data from the near-infrared spectrometer NIRSPEC on the Keck II telescope [8] as well as data from the JWST Near-Infrared Spectrograph (NIRSpec) [9] are both referenced within this work for comparative analysis to laboratory based spectroscopy. Both these observational methods provide data from 1 to 5 microns with the ground-based observations interrupted by the water windows within our atmosphere.

IR instrumentation

For our laboratory data we utilize a commercially available Thermofischer Nicolet IS50 allowing for comparative analysis to the observational data. This instrument utilizes two sources, the Polaris® IR source with a range from 1.04 to 500 µm and a Tungsten-Halogen NIR/Vis source ranging from 0.37 to 5.0 µm. The fourier transform system is based on a Michelson interferometer with a movable mirror. The source provides a polychromatic light which is collimated and interacts with a KBr beam splitter for our instrument. The beam is then directed to either the fixed mirror or the moving mirror and reflected back to the beam splitter. A portion of the original light then passes into the sample compartment where it interacts with sample. After hitting the sample the light is refocused onto a Mercury Cadmium Telluride detector (MCT-A). The difference in the optical path length between the two arms of the interferometer is called the optical path difference (OPD). An intergerogram is created by varying the OPD and recording the signal at various mirror positions. It is integral for the system that the beams recombine exactly as the system scans. The intergerogram is converted to a spectrum by Fourier transformation, hence the nomenclature [10]. Instead of utilizing the sample chamber interior to the Nicolet IS50, the beam is focused into the UHV chamber with two off axis parabolic mirrors. Two focusing mirrors are needed due to the divergence of the source and to allow for our geometry restrictions. After interaction with the sample, the light is captured using a flat mirror and then focused onto the detector using a parabolic mirror. The sensor for the detector is located roughly 1 cm within the optic and the beam is optimized to fill this sensor. Custom hardware was machined and built to ensure stability of the mirrors and the detector. The 3D printing resources at Caltech were used to prototype fits before machining. This system allowed for multiple iterations of parts at low cost. A Labsphere® infragold puck is used for background and alignment. Alignment was an issue due to the low signal produced with diffuse reflectance spectroscopy. We expected a collimated beam when directed out of the spectrometer but unfortunately this did not occur. When using the internal sample chamber and the standard DLaTGS detector we were able to produce a small spot size and high signal to noise. When directing the beam external to the spectrometer there was large divergence of the incident beam. A large portion of our signal was lost before entering our sample chamber. The catching mirror which was originally

50 mm in diameter was replaced with a 75 mm parabolic mirror with 100 cm focal length. This ratio produced a collimated beam at our second parabolic input mirror. For preliminary alignment, the white light halogen tungsten source was used. This allowed for rough alignment but caused chromatic dispersion due to the IR coating on the optics. To counteract the low signal-to-noise and improve alignment the aperture was opened up as large as possible on the spectrometer. The resolution was decreased to 8 cm^{-1} and the beam scan range was decreased. This allowed for the largest amount of light to reach the detector but at cost of resolution. We then iterated from this point adjusting the beam path with the two steering mirrors, mirrors 1 and 3, until we were able to reach peak signal for that configuration. The aperture was then decreased slightly and the iteration process was continued. Due to the nature of the beam path the mirror position for the peak value when the aperture is fully open and the mirror position for our desired aperture position differed. The aperture was kept as large as possible to maximize signal for our required resolution, 2 cm^{-1}. We did not utilize the "Bench Align" setting internal to the OMNIC® software due to complications with how it found signal. The internal alignment system only seemed to work when the beam was in the main sample compartment. When working with the liquid nitrogen cooled MCT-A detector positioning of the beam into the window on the detector was key. Since the detector is mounted external to the spectrometer both height and position is variable. A stabilized height adjustable post mount holds the custom base plate allowing for fine tuning of the position. When cooling the detector frost forms on the window and must be removed with compressed air. We also observe a change in signal with detector warming. Once the detector begins to warm, even before the software recognizes it as above ideal temperature a slight drop in signal occurs. Upon cooling with liquid nitrogen a test spectra was run to ensure stability since we observed a delayed response on cooling as well. The software registers the detector as cold before it has reached optimal operational temperature. The addition of a nitrogen purge box 2.5 allows for accurate measurement of water ice and carbon dioxide without atmospheric effects. This purge box also removes the frosting issue on the window of the detector.

2.5 Cryogenics

The PICL lab has utilized two forms of cryogenics with the internal cryostat for sample cooling. A Lake Shore ® Model 335 cryogenic temperature controller is used for temperature control. It contains heaters at 50 W and 25 W allowing for precise temperature control with with a closed feedback loop to two Lake Shore DT-670

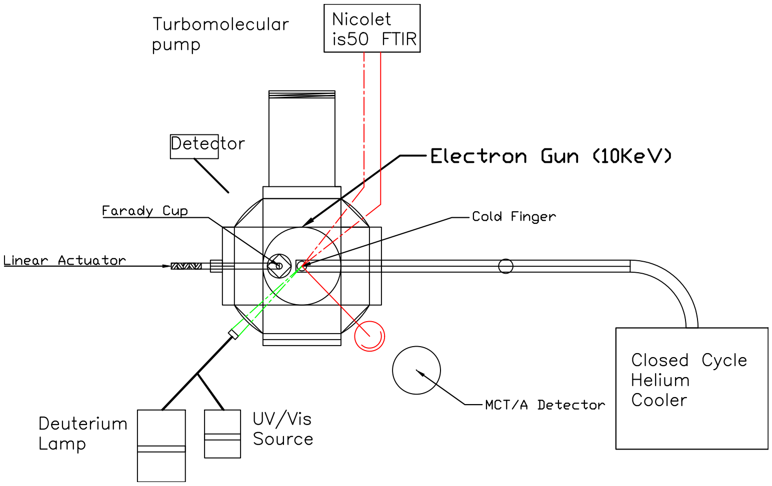

Figure 2.4: Schematic of PICL from a top down view. The visible beam path is shown in green while the IR beam path is shown in red. The main chamber is to scale while the connections to the detectors and closed cycle cooler are not

Silicon diodes, one diode is located at the end of the cold finger the other is internal to the cryostat supple arm. For the first iteration of cryogenic systems a 35 liter liquid nitrogen dewar with an ST-400 Lake Shore SuperTran cyrostat was used. It integrates into the UHV environment via a conflat flange and uses a capillary for the transportation of liquid nitrogen to the cold head. It offered fast cooling as compared to other systems but lacked reliability when precooling the system. Since it works via capillary action if vacuum is not maintained while the system is cooling, moisture can condense in the capillary and then freeze. We found that using a 24-gauge steel wire was able to remove the obstruction but the cryostat had to be removed from the dewar and the UHV system. There was also the risk of the wire breaking within the capillary and thus causing a larger obstruction. Precooling the system is paramount when working with hydrated salts as well as frozen samples such as brines, carbon dioxide, and water. To allow for precooling, an Advanced Research Systems DE 202 cryostat with closed cycle helium compressor (ARS-4HW) was installed. This uses helium instead of liquid nitrogen but requires a large compressor and water cooling. This system does not function with capillary action and vacuum is not required for reliable cooling. For the system to reach the minimum temperature vacuum is still required. The closed cycle cyrostat does not require refilling of the liquid nitrogen dewar allowing for longer term experiments to be conducted. The water cooling was provided by the in-house chilled water supply at Caltech, air chilling was not an option due to limited air turn over and ventilation in the laboratory space. Liquid helium allows for a lower minimum temperature as compared to liquid nitrogen. We observed a minimum temperature of 8 K for closed cycle helium and 77 K for liquid nitrogen. This range expands the possible species we can investigate like CO_2 as discussed in Chaper 5. Due to colder base temperature and the smaller thermal load of the DE-202 coldhead, longer cool down times occur with the closed cycle system. The closed cycle system is able to maintain temperatures between 8 K and 120 K with the heaters and has expanded the range of samples that we can study.

2.6 Nitrogen Purge Box

An enclosure for the UHV system, including the FTIR spectrometer was constructed to remove atmospheric signals from both water and carbon dioxide. The original consideration for experiments probing CO_2 signals was to measure the CO_2 concentration during collection of the reference spectrum and attempt to maintain the same concentration for the sample spectrum. This method was measured with a portable carbon dioxide monitor. The air turn over in the room and the exhalation of researchers meant that this method of maintaining consistent CO_2 concentrations was not possible. We observed fluctuations of over 300 ppm depending on the time of measurement. A modular enclosure was built to purge the FTIR spectrometer and the full IR beam path. Because samples have to be introduced to the UHV chamber a method of opening the purge box had to be possible. For the structural frame, 80/20 aluminium T-slot 1.00" x 1.00" bars were used. The walls are made of clear acrylic sheets which slot into the grooves of the structural support. The clear acrylic can be cut to allow for the irregular shape of the the UHV components. Both the support and the acrylic were cut in the CCE machine shop, first on a band saw and then with a CNC machine to ensure a secure fit. The various protrusions from the UHV chamber were sealed with caulk and rubber gaskets. Non-hardening caulk allows for removal of the front acrylic plate vs sealing caulk which is used on the more permanent pieces. Electrical and fiber optic cables are sealed with rubber grommets. The system is purged with nitrogen flows via a swagelok connection allowing for nitrogen to flow into the chamber or into the enclosure via a gate valve. Figure 2.5 shows the enclosure from above. This set up is able to decrease the concentration of CO_2 to below 1 ppm, which is the limit of detection for the carbon dioxide monitor. Spectra for pre and post nitrogen purge is shown in Figure 5.1.

With a fully enclosed beamline we are unable to adjust the beam path when the system is closed. Water concentration within the purge box is measured by using desiccant and monitoring the color change. The purge system eliminated frosting on the window to the MCT-A detector. The MCT-A detector is filled via a funnel through the top of the purge box and then covered with a lid.

2.7 Sample Preparation

One of the main motivations for the creation of PICL was to perform experiments that utilized bulk sample properties for understanding observational spectroscopy as compared to previous laboratory data. The majority of cryogenic irradiation experiments utilize vapor deposition and create thin film samples [11–13]. These sort of experiments grow ice via a mixture of gases, usually in a pressure manifold, on a reflective surface creating isolated ice films. This method is fantastic at creating well coupled samples but lacks the bulk characteristics that are present on icy bodies. Vacuum does not have to be broken for sample deposition allowing for lower ultimate pressures. When investigating bulk sample properties experiments are usually performed at room temperature and without irradiation. While some work has included cryogenics [14–18] or irradiation [19] rarely are these techniques coupled. The research performed in the PICL has shown the importance of these two elements when doing spectral analysis. The lack of previous experimental work with these unique sample parameters meant sample preparation was a critical aspect.

Copper Sample Cup

To avoid contamination of the cold finger and allow for complete removal of the sample post experiment procedure, samples cups were designed and machined. These needed to be UHV compatible, non-reactive with the samples, and have good thermal conductivity. Low oxygen copper rod was chosen because it allowed for easy manufacturing on a lathe and fit within our requirements. Thermal conductivity was still an issue between the sample cup and the cold finger so tolerance was kept to below 1 mm. A lip was left to allow for removal of the sample cup with kelly clamps. This flange also increased thermal contact with the cold finger. To further increase thermal coupling indium foil was placed under the sample and between the flange

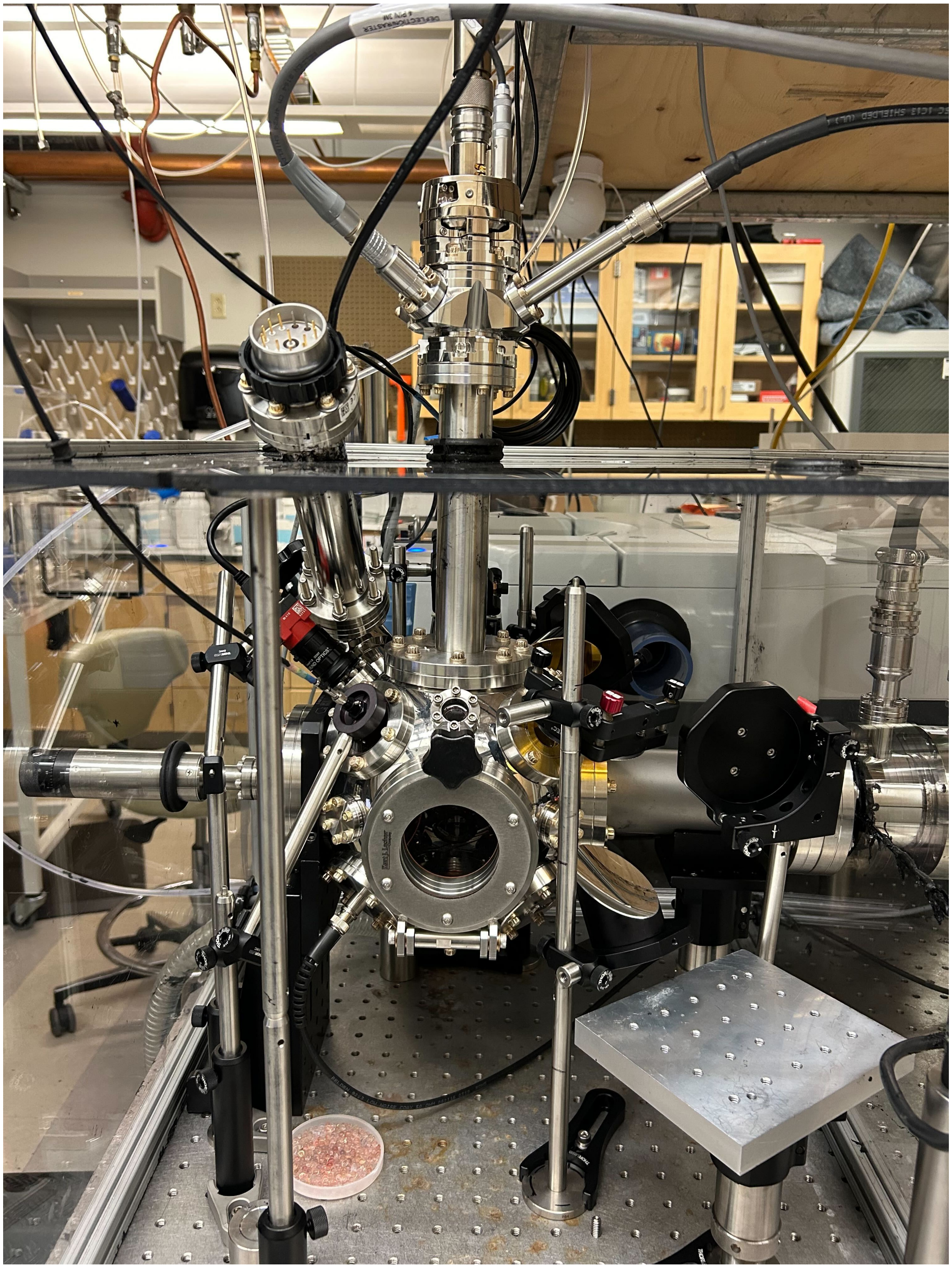

Figure 2.5: The Planetary Icy Chemistry Laboratory UHV Chamber with nitrogen purge box. The front panel is removed for sample introduction to the chamber. The top piece is split into two sections with the front section removable for access to the off axis parabolic catching mirror.

and cold finger. Indium foil is a soft sheet with very high thermal conductivity at 86 W/m/K. Coupling between the copper cup and our samples was another area of thermal loss. When working with bulk grains, either as salt crystals or ice samples, temperature is an important parameter. Thermal conductivity between grains is poor and there is poor stacking efficiency. When in a high vacuum environment there is limited thermal conductivity between grains leading to a large thermal gradient between the bottom grains, which are in contact with the copper cup, and the surface grains, which experience more exposure to thermal radiation of the exterior. Thermal emission from the room is the main source of heating. To counteract this issue indium foil was placed in the bottom of the sample cup and the ground sample was pressed into the indium foil. The excess sample was brushed off to ensure that any sample remaining was thermally coupled. The thermal coupling with and without indium foil was tested with sodium chloride and a significant improvement in temperature was observed. K-type thermal couples were placed in the sample and on the flange of the sample cup. The addition of secondary thermal couples allowed for testing the range of temperatures at different locations within sample chamber. Irradiation was not possible when measuring the sample temperature with a secondary thermocouple due to destruction of the thermocouple with exposure to irradiation. Corrosion is an issue and we found the thermocouples were sensitive to exposure in brine solutions which could lead to destruction of wires. We observed strong correlation between sample temperature and sample cup temperature.

Cryogenic preparation of solid samples

The cryogenic sample preparation capabilities of our laboratory differ greatly for different samples. A nitrogen glove box is used to sample preparation of hydration sensitive samples. Utilizing a mortar and pestle samples are ground in an inert environment at liquid nitrogen temperatures. For salt samples, the metal mortar is suspended in a cryovessel filled with liquid nitrogen. The sample is then ground and sieved to the desired grain size, with precooling of both the pestle and the sieves occurring before introduction to the salt. This method has been found to maintain hydration state. The sample cup is precooled by liquid nitrogen submersion, as is the sample presser, a custom copper tool allowing for uniform compaction and depth of the samples. The sample presser was designed as to be functional with the limited dexterity provided by the glove box gloves. The sample is then removed from the glove box, in a nitrogen head space from evaporation of liquid nitrogen, for transportation into the UHV chamber. Transportation in this manner greatly limited

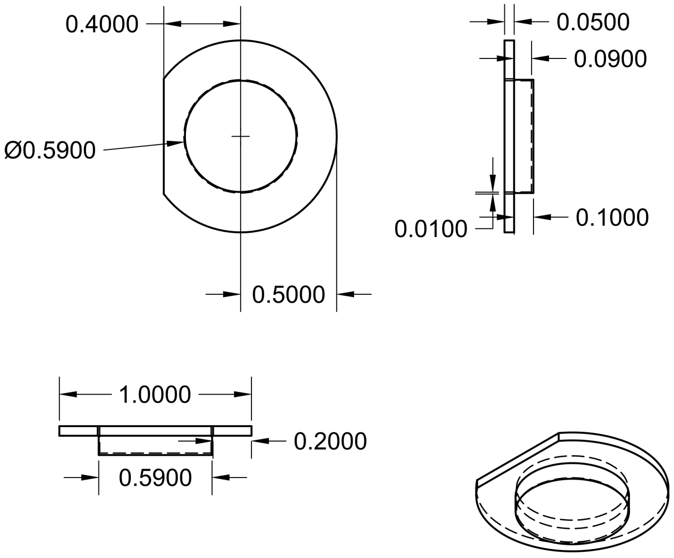

Figure 2.6: Schematic of the OFHC copper sample cup. Units are imperial in this instance. The cup is notched so as to not interfere with the mounting hardware for the silicon diode.

water condensation on the sample surface, as observed with FTIR. The sample cup was placed into a precooled chamber with a positive pressure of nitrogen. The UHV hatch is left slightly open as to not over pressure the chamber. Once the sample is inserted, the door is closed and nitrogen flow is stopped. Depending on the sample conditions, rough vacuum is not started until the thermocouple has reached a set temperature. The temperature is then allowed to decrease under rough vacuum before the turbo molecular pump is switched on. This experimental parameter set up allows us to maintain the hydration state of various salt species predicted on Europa, which at vacuum and in terrestrial environments would not be stable.

Cryogenic sample preparation of brines and ices

Due to the fact that majority of cryogenic brine chemistry and ice irradiation is performed via vapor deposition there exists little previous sample preparation methods. In the course of this research brine sample preparation was attempted with multiple experimental parameters. One of the first parameters changed was pre- or post-freezing recombination. We were interested if the combination as a solid salt with water ice at cryogenic temperatures would exhibit the same visible spectroscopic features as brines. For the first tests, Milli-Q ultrapure® water (hence forth referred to as sample water) was flash frozen under liquid nitrogen and ground to 100 microns.

Halite (NaCl hydrate) was then ground to 100 microns under liquid nitrogen and the species were mixed. For the brine solutions, saturated brines of sodium chloride at 357 mg/ml were made by weight. These brines were then frozen in three different manners.

1. Slow freezing at 193 K in vials in a freezer
2. Flash freezing via squeeze bottle into liquid nitrogen cooled mortar
3. Flash freezing via submersion into liquid nitrogen

The slow freezing method created two distinct issues. The first being separation of the brine during freezing. A gradient was clearly observable between the water ice and the frozen brine. The solution froze from the outside inwards causing varied salinity. While the concentration of brine within the ice was known the varied consistency could prove spectroscopically significant. The second issue was removal of the ice sample from the cuvette without melting. Strong adhesion was found between the ice and the plastic vessel. Various cryogenic sample vessels were tested but none offered repeatable sample removal. The squeeze bottle technique provided promising results in terms of consistent saturation of ice. The issue derived from coating on the walls of the mortar. A shell formed with the liquid and at liquid nitrogen temperatures becomes quite resistant to grinding. The addition of a spatula for scraping of the sides did allow for grinding but was time consuming and not feasible due to the lack of dexterity within the glove box. Submersion within liquid nitrogen of the brine removed the issue of shell formation but presented an interesting problem in terms of differentiation. If a large amount of brine was submerged in liquid nitrogen, a white crystalline crust formed on the exterior. Upon breaking the outer crust a saturated salty amorphous-like brine was found in the center. This central portion was too viscous to be ground and even after exposure to liquid nitrogen sample consistency was compromised. The slurry and puck can be seen in Figure 2.7. A combination of methods 2 and 3 was found to produce the most uniform sample conditions. A squeeze bottle was used to deposit a small amount of brine into liquid nitrogen. This creates small granular spheres which seemed to have limited differentiation. This allowed for grinding but stops the formation of a shell on the mortar. This method was used for various salt samples all producing consistent grains. These grains are then sieved to the desired micron size using precooled sieves and packed into the copper sample cups in the same manner as solid salt samples.

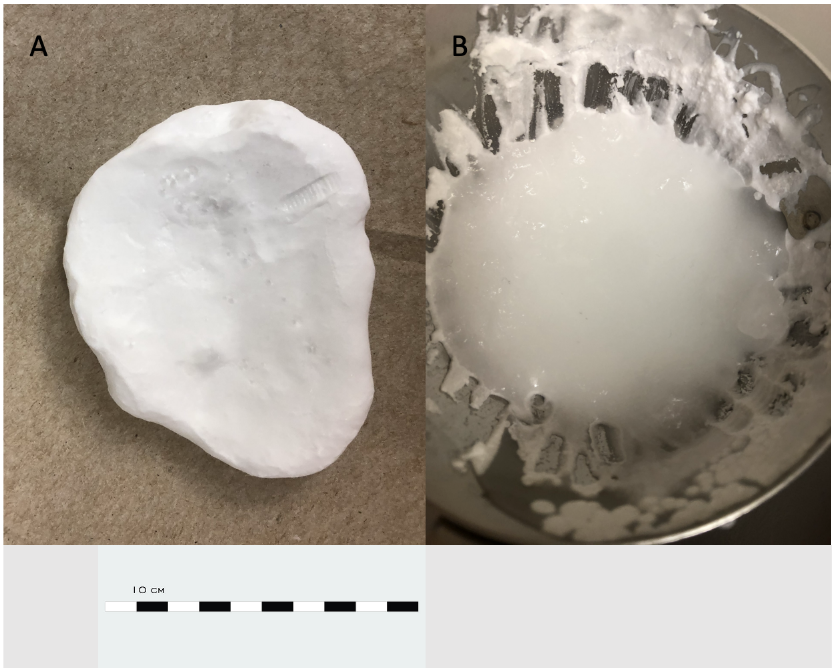

Figure 2.7: Brines frozen at liquid nitrogen temperatures in an inert nitrogen environment. A. $MgCl_2$ brine flash frozen via submersion in liquid nitrogen. The outer layer has a lower water concentration with the interior existing as a vicious fluid. B. $MgCl_2$ frozen by squeeze bottle spray into a liquid nitrogen cooled mortar. Flash freezing via this method causes ice build-up on the walls as well as slurry formation.

Chamber Precooling

When working with brines or other ice samples it is important that temperature is maintained as to prevent thawing and refreezing of the samples. Since electron penetration and UV/VIS photon penetration is in the sub-μm range, homogeneity is important. The thawing of brine samples causes differentiation of the samples and can change the surface concentration. Sublimation of samples is also a possibility at vacuum. Because we create bulk samples vacuum is broken to insert the samples. If the cryostat is run without vacuum, deposition from the atmosphere forms on the cold finger and limits the base pressure the system is able to obtain. To prevent this, house nitrogen is pumped into the UHV chamber with the chamber access door open. This prevents deposition by creating back pressure of the system and removing water vapor from the chamber. This method limits the base temperature of the cryostat because warm nitrogen gas is being introduced to the system. To increase precooling and prevent deposition, we designed and built a precooling sample cup. This cup was then filled with liquid nitrogen and placed within the chamber. As the liquid nitrogen

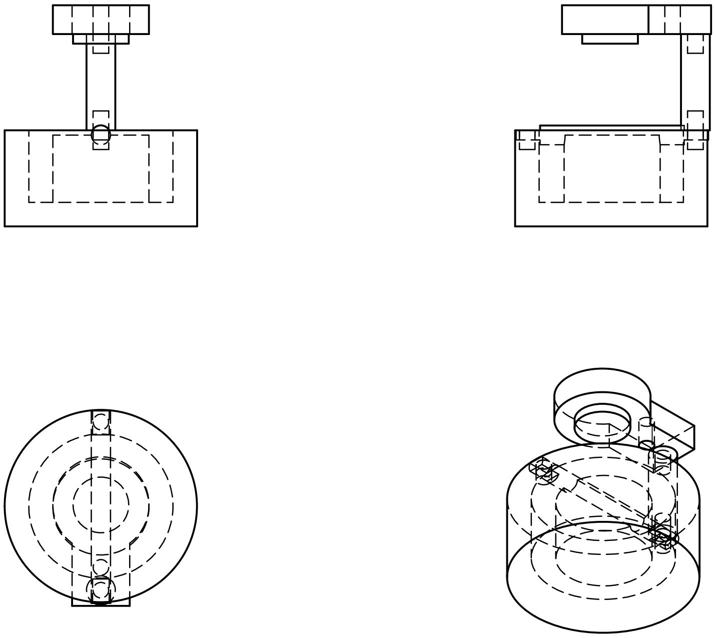

Figure 2.8: Schematic of the assembled liquid nitrogen precooling hanging sample cup. It is constructed from OFHC copper with vented hardware and is constructed of four separate pieces.

vaporized it cooled the cryostat finger as well as displacing water vapor within the chamber. The hanging design allowed for us to add the precooling system through the access door while maximizing the volume of liquid nitrogen. The schematic for the system is shown in Figure 2.8. This system decreased the amount of deposition of water vapor with cooling but was unable to completely eliminate deposition. Due to the expansion of liquid nitrogen during vaporization the access door remained open to prevent over pressuring of the chamber. This pre-cooling copper cup, in conjunction with the closed cycle helium cooler, allows us to maintain below 180 K before vacuum.

Carbon Dioxide Ice Samples

To study the trapping of carbon dioxide in water grain samples, as discussed in Chapter 5, pure CO_2 was tested. This was to ensure thermal conductivity and band position of solid CO_2. The vapor pressure of bulk CO_2 has been measured previously

[20], and at our rough vacuum settings temperature below 102 K allows for bulk sample stability while for high vacuum, 5×10^{-8} torr, bulk sample temperature must remain below 81 K. Carbon dioxide ice samples were tested various ways using a Burkle Dry Ice Maker, which connects directly to a Airgas 99.99% CO_2 cylinder. This creates high purity CO_2 ice without the use of other cooling systems. The resulting ice is transferred into a sample cup in an inert nitrogen environment within the glove box where it is loaded into a precooled copper sample cup. The expansion method of ice formation creates very small grains which are pressed into indium foil. The samples are then transferred to the precooled chamber. Precooling in this instance is critical due to the sublimation of CO_2. With the dry ice maker we were able to keep carbon dioxide up to 65 K as measured by our thermocouple at 2.3×10^{-7} torr, suggesting a variation of 19 K between bulk CO_2 and the thermocouple. The samples are in contact with cryogenic cooling on three sides but is exposed to thermal emission heating from chamber on the top. For samples undergoing irradiation, only vacuum can exist between the sample and the electron gun. Since carbon dioxide samples will not be irradiated and thermal coupling between the sample cup and CO_2 is not as strong as with brines or salt samples due to carbon dioxides decreased thermal conductivity [21, 22], we designed a new sample cup with taller walls to allow for sapphire windows to be placed above the sample. Sapphire crystals have high transmission from 0.2 to 5 µm while blocking the thermal emission in the 10 µm range. The uncoated sapphire windows are layered with a metal spacer in between to increase thermal isolation from the walls of the chamber. This method improved the stability of carbon dioxide at high vacuum within the chamber.

2.8 Electronic Integration

The instrument set up relies on several controllers for the varied components. For integration of the controls a python script, shown in Appendix B, is used. This allows us to pull data from multiple instrument controllers into a single GUI and export the data as a text file. The electron gun requires 10^{-6} torr for the cathode to function properly and a fail safe was coded to shut off the electron gun if the pressure exceeded this value. The operating temperature of the cathode is 2200 K and the temperature must cool to below 700 K to prevent oxidation. This fail safe works in the instance of pressure rising from sample evaporation or with pump failure but did not work in the instance of power failure. In the instance of power failure, all systems shut down and the pressure increase within the chamber is faster than the temperature decrease of the cathode leading to oxidation of the cathode. In conjunction to this fail safe, an uninterrupted power supply (UPS) was installed for the computer as well as both vacuum pumps. This ensures that with power loss the pressure will remain below the oxidation point of the cathode. The electron gun controller was placed on a separate circuit with additional surge protection due to issues with power instability in the laboratory. These modifications were made sequentially as issues arose with the system, such as cathode oxidation and blown fuses within the electron control unit. An Allied Vision Alvium 1800 U-240c camera has also been installed allowing us to monitor the samples remotely and capture images of changes with irradiation in-situ.

2.9 Conclusion

This portion of the thesis outlines the construction, sample preparation and capabilities of the PICL laboratory. Irradiation of bulk samples at cryogenic temperatures can be performed coupled with UV/Vis and FTIR spectroscopy. The addition of a purge enclosure allows for more accurate measurement of both hydration state and carbon dioxide absorption. The subsequent chapters within this thesis highlight the previous experiments conducted using the instrumentation outlined in this section and outline future work that will be conducted.

References

1. Cooper, J. Energetic Ion and Electron Irradiation of the Icy Galilean Satellites. *Icarus* **149,** 133–159. doi:`10.1006/icar.2000.6498` (Jan. 2001).
2. *Europa* (eds Pappalardo, R. T., McKinnon, W. B. & Khurana, K. K.) (University of Arizona Press, Dec. 15, 2017). doi:`10.2307/j.ctt1xp3wdw`.
3. Ramos-Ballesteros, A. *et al.* Gamma radiation-induced defects in KCl, $MgCl_2$, and $ZnCl_2$ salts at room temperature. *Physical Chemistry Chemical Physics* **23,** 10384–10394. doi:`10.1039/D1CP00520K` (2021).
4. Tani, A., Hasegawa, N., Norizawa, K., Yada, T. & Ikeya, M. Radiation-induced radicals in hydrated magnesium sulfate. *Radiation Measurements* **47,** 890–893. doi:`10.1016/j.radmeas.2012.03.006` (Sept. 2012).
5. Carlson, R. W. & Hand, K. P. Radiation Noise Effects at Jupiter's Moon Europa: In-Situ and Laboratory Measurements and Radiation Transport Calculations. *IEEE Transactions on Nuclear Science* **62,** 2273–2282. doi:`10.1109/TNS.2015.2460674` (Oct. 2015).
6. Trumbo, S. K., Brown, M. E. & Hand, K. P. Sodium chloride on the surface of Europa. *Science Advances* **5,** eaaw7123. doi:`10.1126/sciadv.aaw7123` (June 2019).

7. Trumbo, S. K. *et al.* A New UV Spectral Feature on Europa: Confirmation of NaCl in Leading-hemisphere Chaos Terrain. *The Planetary Science Journal* **3,** 27. doi:`10.3847/PSJ/ac4580` (Feb. 1, 2022).
8. Trumbo, S. K., Brown, M. E., Fischer, P. D. & Hand, K. P. A New Spectral Feature on the Trailing Hemisphere of Europa at 3.78 *micro* m. *The Astronomical Journal* **153,** 250. doi:`10.3847/1538-3881/aa6d80` (May 11, 2017).
9. Trumbo, S. K. & Brown, M. E. The distribution of CO $_2$ on Europa indicates an internal source of carbon. *Science* **381,** 1308–1311. doi:`10.1126/science.adg4155` (Sept. 22, 2023).
10. Griffiths, P., De Haseth, J. & Winefordner, J. *Fourier transform infrared spectrometry* (Wiley, 2007).
11. Yocum, K. M., Milam, S. N., Gerakines, P. A. & Widicus Weaver, S. L. Sublimation of Laboratory Ices Millimeter/Submillimeter Experiment (SubLIME): Structure-specific Identifications of Products from UV-photolyzed Methanol Ice. *The Astrophysical Journal* **913,** 61. doi:`10.3847/1538-4357/abf14e` (May 1, 2021).
12. Materese, C. K., Gerakines, P. A. & Hudson, R. L. Laboratory Studies of Astronomical Ices: Reaction Chemistry and Spectroscopy. *Accounts of Chemical Research,* acs.accounts.0c00637. doi:`10.1021/acs.accounts.0c00637` (Dec. 31, 2020).
13. Mahjoub, A. *et al.* ELECTRON IRRADIATION AND THERMAL PROCESSING OF MIXED-ICES OF POTENTIAL RELEVANCE TO JUPITER TROJAN ASTEROIDS. *The Astrophysical Journal* **820,** 141. doi:`10.3847/0004-637X/820/2/141` (Mar. 30, 2016).
14. De Angelis, S. *et al.* Temperature-dependent, VIS-NIR reflectance spectroscopy of sodium sulfates. *Icarus* **357,** 114165. doi:`10.1016/j.icarus.2020.114165` (Mar. 2021).
15. De Angelis, S. *et al.* VIS-IR spectroscopy of magnesium chlorides at cryogenic temperatures. *Icarus* **373,** 114756. doi:`10.1016/j.icarus.2021.114756` (Feb. 2022).
16. Dalton, J. B. & Pitman, K. M. Low temperature optical constants of some hydrated sulfates relevant to planetary surfaces. *Journal of Geophysical Research: Planets* **117.** doi:`10.1029/2011JE004036` (E9 2012).
17. Dalton, J. B. Linear mixture modeling of Europa's non-ice material based on cryogenic laboratory spectroscopy. *Geophysical Research Letters* **34.** doi:`https://doi.org/10.1029/2007GL031497` (2007).
18. Dalton, J. *et al.* Spectral comparison of heavily hydrated salts with disrupted terrains on Europa. *Icarus* **177,** 472–490. doi:`10.1016/j.icarus.2005.02.023` (Oct. 2005).

19. Hibbitts, C., Stockstill-Cahill, K., Wing, B. & Paranicas, C. Color centers in salts - Evidence for the presence of sulfates on Europa. *Icarus* **326,** 37–47. doi:`10.1016/j.icarus.2019.02.022` (July 2019).

20. Bryson, C. E., Cazcarra, V. & Levenson, L. L. Sublimation rates and vapor pressures of water, carbon dioxide, nitrous oxide, and xenon. *Journal of Chemical & Engineering Data* **19,** 107–110. doi:`10.1021/je60061a021` (Apr. 1974).

21. Sumarokov, V. V., Jeżowski, A., Stachowiak, P. & Freiman, Y. A. The thermal diffusivity of molecular cryocrystals. *Low Temperature Physics* **45,** 343–346. doi:`10.1063/1.5090093` (Mar. 1, 2019).

22. Huang, W. *et al.* Effective thermal conductivity of reservoir freshwater ice with attention to high temperature. *Annals of Glaciology* **54,** 189–195. doi:`10.3189/2013AoG62A075` (Jan. 2013).

Chapter 3

THE INFLUENCE OF TEMPERATURE AND PHOTOBLEACHING ON IRRADIATED SODIUM CHLORIDE AT EUROPA-LIKE CONDITIONS

1. Denman, W. T. P., Trumbo, S. K. & Brown, M. E. The Influence of Temperature and Photobleaching on Irradiated Sodium Chloride at Europa-like Conditions. *The Planetary Science Journal* **3,** 26. doi:`10.3847/PSJ/ac4581` (Feb. 1, 2022).

3.1 Abstract

Europa's leading hemisphere chaos regions have a spectral feature at 450 nm that has been attributed to absorption by crystal defects in irradiated sodium chloride, known as F-centers. Some discrepancies exist between the laboratory data of irradiated sodium chloride and the observations, including a ~10 nm shift in central wavelength of the F-center band and the lack of the prominent 720 nm absorption on Europa from M-centers, which result from the coalescence of pairs of F-centers. Here, we perform irradiation experiments on sodium chloride in an attempt to understand these discrepancies. We show that careful control of the temperature of the sample at a temperature of 120 K yields F-centers with an absorption wavelength comparable to that of Europa. In addition, we measure the effect of photobleaching — the destruction of F-centers by photons — and show that at the energetic particle and photon flux on Europa, an equilibrium will be reached where only a modest F-center absorption develops. The density of F-centers never reaches high enough values for the creation of secondary M-centers. Our experiments predict that F-centers grow during the night on Europa in the absence of photobleaching and then partially decay during the daytime. We show observations from the Hubble Space Telescope consistent with this prediction. All observations of the 450 nm F-center on Europa are now consistent with laboratory measurements of sodium chloride, confirming the presence of this salt on Europa.

3.2 Introduction

Jupiter's moon Europa has a young, icy surface which undergoes high energy radiation bombardment and covers a salty liquid water ocean [1–3]. The salts in the ocean presumably derive from the interaction between the liquid water and the silicate seafloor [4], and the composition of the salts offer insight into the manner of this interaction. While no direct access to the ocean is currently possible, Europa's geologically young chaos regions have likely been resurfaced by material ultimately derived from the interior ocean and thus could provide information on its composition [5–8]. On the trailing side of Europa these chaos terrains are bombarded by sulfur plasma, confusing the interpretation of their initial composition; the leading side chaos terrains are thus the most likely to retain signatures of the original composition.

Trumbo *et al.* [9] recently reported *Hubble Space Telescope* (HST) observations that showed the existence of an absorption feature at 450 nm in Europa's leading-side chaos terrains and proposed that this feature is due to sodium chloride salts. While salts are generally indistinct in the visible wavelength range, irradiation of alkali halides, in particular, produce multiple defects and dislocations within the crystal structure, giving rise to distinct "color center" absorptions. For NaCl, the most prominent color center is the F-center, occurring at approximately 450 nm [10].

F-centers occur when radiation ejects a chlorine atom from its location in the crystal lattice and an electron fills the hole. More complicated color centers also form, including M-center absorption at 720 nm, which appear when the density of F-centers is sufficiently high that pairs begin to coalesce. This F-center coalescence can eventually lead to macroscopic sodium colloids which broadly absorb in the 580 nm region. F-centers can be destroyed by absorption of photons within the 400 to 500 nm band of the absorption feature in a process called photobleaching, which excites the electron into the conduction band [11].

Experiments performed in order to understand the possibility of NaCl color centers on Europa [12–14] suggested that irradiation at conditions similar to those on Europa would form both F-centers and M-centers. The HST data, however, did not completely match the laboratory data. In the laboratory, the central wavelength of the F-center was measured to be 460 nm, rather than the $\sim$450 nm seen on Europa, and the HST data showed no hint of the predicted absorption near the 720 nm M-center. Trumbo *et al.* [9] noted that when the irradiation of the NaCl stopped in the Poston *et al.* [13] experiments, the F-center wavelength quickly shifted blueward as the absorption rapidly decayed. They hypothesized that irradiation at the lower flux level seen on

Europa could lead to the shorter wavelength feature. They further hypothesized that the lack of M-centers on Europa is the result of solar photobleaching which would destroy F-centers at nearly the same rate as their creation through irradiation. This destruction would lead to an equilibrium with a low number of F-centers that would not have a high enough density for M-centers to form.

Here, we perform experiments to test these hypotheses. Our goal is to determine if the differences in appearance between the HST spectra and the laboratory data can be reconciled with the interpretation that the ~450 nm absorption feature seen on Europa is indeed due to irradiated NaCl.

3.3 Method

Our experiments were designed to measure the spectral changes in sodium chloride from electron and photon bombardment at temperatures similar to Europa. For each experiment, fresh hydrated sodium chloride powder, USP (CAS-7647-14-5) was pressed into a layer of indium foil inside of a copper sample cup. Excess salt was brushed off to ensure good thermal coupling between the remaining grains and the sample cup. The sample cup was then loaded onto a cold finger inside of a Kimball Physics ultrahigh vacuum chamber. The chamber was pumped down to 10^{-8} torr using an Agilent ID3 backing pump and TwisTorr 84 molecular turbo pump. The cold finger was cooled with a Janis ST-400 liquid nitrogen cryostat. Once the desired temperature was reached, the grains were irradiated with 10 keV electrons from a Kimball Physics EGG-3101 electron gun. The current is measured with a Kimball Physics Faraday cup mounted on a linear actuator that can be inserted into the electron beam path. Electron currents used in the different experiments and their relationship to the approximate energy flux on Europa are shown in Table 3.1. We obtained spectra of the samples from 300 to 1000 nm by illuminating the sample via an external lens fed by a fiber optic connected to both a stabilized deuterium and a stabilized tungsten-halogen lamp from Thorlabs. We illuminated the sample at 45° from the surface normal and collected the diffuse reflection 90° from the specular direction and 45° from the surface normal. Since NaCl is nearly featureless through the spectral range, unirradiated salt at the desired temperature was used as a spectral reference for the our samples.

For our series of experiments the electron flux and illumination conditions were varied. In our initial experiments, we simply tested the system to ensure that we could create and measure F- and M-centers. Our initial electron flux, as measured in the

Table 3.1: Sodium Chloride Experiments

	current density (nA/cm^2)	electron flux ($electrons/cm^2/s$)	450 nm irradiance ($mW/m^2/nm$)	dose rate (eV/16amu/yr)	temperature (K)
Low	12	8×10^{10}	6.0	2.5×10^3	120
Low	12	8×10^{10}	–	2.5×10^3	120
–	48	3×10^{11}	6.0	1×10^4	120
Medium	505	3×10^{12}	6.0	1×10^5	120
Medium	505	3×10^{12}	–	1×10^5	120
Medium	505	3×10^{12}	6.0	1×10^5	120(no indium foil)
Medium	505	3×10^{12}	–	1×10^5	200
High	3410	2×10^{13}	6.0	7×10^5	120
High	3410	2×10^{13}	–	7×10^5	120
Europa	n/a	n/a	78	10	120

Note: The energy deposited is for the top 1.2 μm micron of the sample. For the experiment without indium foil the temperature of the salt is unknown. The irradiance of our spectral lamp is estimated at 450 nm. For Europa, the photon flux and temperature are given for equatorial noon.

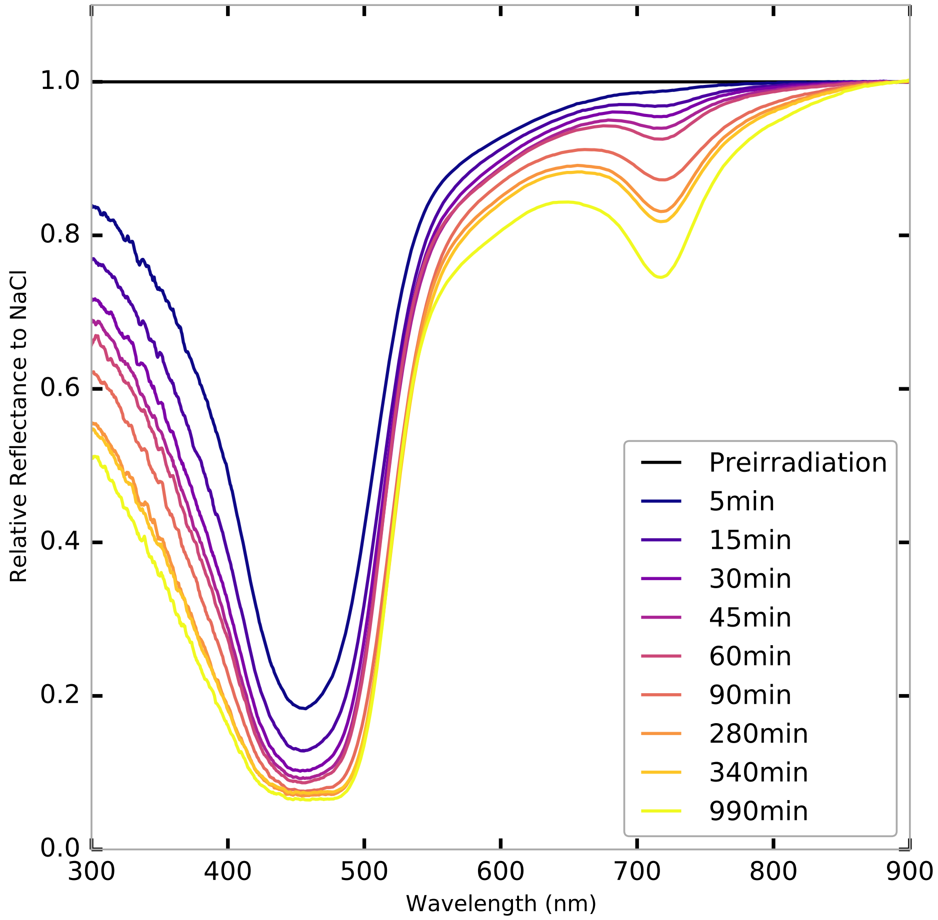

Figure 3.1: Spectra of irradiated sodium chloride at 120K with our high irradiation dosage and no photobleaching. M-center growth is observed after F-center saturation.

Faraday cup, was 2×10^{13} electrons/cm^2/s. Since the penetration depth of 10 keV electrons is around 1.2 μm [12] such a flux gives the equivalent of 7×10^5 ev/16amu deposited each year into the NaCl. The energy deposited on the apex of Europa's leading hemisphere is estimated to be 10 ev/16amu/yr [15]. Our initial experiments are at a dosage rate approximately 70000 times that of Europa. The true dosage rate on Europa is both poorly determined and variable, so this ratio is only an approximation. Additional experiments were run at fluxes 7 times lower and nearly 300 times lower than our initial experiment. These three settings are referred to as high, medium, and low flux. It should be noted that even the low flux is $\sim$ 250 higher than that of Europa. Figure 3.1 shows the results of our first experiment at high flux. F-centers are quickly created and become saturated within approximately 30 minutes. As the density of F-centers increases, coalescence of these defects begins to form M-centers, which begin to absorb at 720 nm by 30 minutes. By the end of the experiment both F- and M-center absorptions are prominent.

In some experiments, we test the effects of photobleaching by leaving our spectral lamp illuminated during the irradiation. While we have no means of measuring the absolute flux density of our spectral lamp inside of the chamber at 450 nm, we estimate this parameter by using the spectral curve and total output provided by the manufacturer as well as the illumination spot size on the sample. We find the irradiance of the lamp at 450 nm to be 6 mW/m^2/nm. This irradiance is approximately 8% of the flux density at Europa from solar illumination.

3.4 Experiments

The visible spectrum of the leading side chaos regions on Europa differs from laboratory spectra of irradiated NaCl in two important ways. First, the Europa feature appears at ~450 nm, rather than the 460 nm wavelength found for NaCl F-centers in the laboratory [12, 13]. Second, the laboratory spectra all show the formation of an M-center at $\sim$ 720 nm, which the HST data strongly rule out. We perform a set of experiments to explore these phenomena.

Wavelength Shift

Trumbo *et al.* [9] noted that, in experiments by Poston *et al.* [13], the F-center spectral feature quickly decayed and shifted blueward when irradiation ceased. They hypothesised that the higher irradiation flux for the laboratory spectra caused the mismatch in wavelength between the Europa and the laboratory spectra. Our first set of experiments were designed to test that hypothesis.

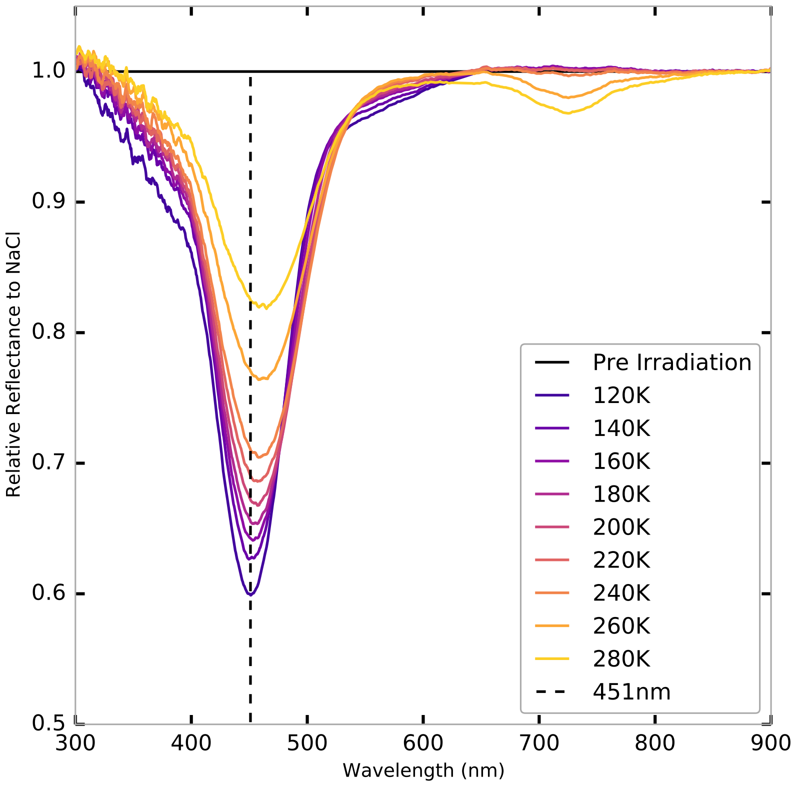

Figure 3.2: Irradiation at 120K with systematic warming of the sample. This shows the redward shift of the F-center with temperature. The central wavelengths from 120 to 280 K are 451.2 nm, 453.1 nm, 454.1 nm, 456.1 nm, 457.6 nm, 459.0 nm, 460.5 nm, 461.9 nm, and 463.4 nm. The minimum values were found by doing a parabolic fit to the F-center range (400 to 500 nm) and then finding the wavelength minimum of the parabola.

We first attempted to reproduce some of the key results of Poston *et al.* [13]. We irradiated a NaCl sample at a temperature of 120 K at our medium flux level, which is approximately 6 times that of the initial Poston *et al.* [13] irradiation, with no photobleaching. This flux is approximately 10^4 times the flux level at Europa. We irradiated for 2 hours, periodically obtaining spectra, to measure the growth of both the F-center and the M-centers. This 2 hour irradiation is equivalent to 2.3 years on Europa. We observed a central wavelength for the F-center of 451 nm, which is significantly shifted from the Poston *et al.* [13] results and much closer to the spectra from Europa (Figure 3.2), even though our flux level was 6 times higher. At the end of the irradiation sequence, the samples were left in the dark at 120K overnight. In contrast to Poston *et al.* [13], we observed no change in the spectrum after ceasing irradiation. We then systematically warmed the sample, allowing the sample to stabilize at each new temperature, and obtained a spectrum at each, in order to examine the effects of temperature. As noted by [16], the wavelength of the F-center systematically shifts redward with increasing temperature. As well as shifting, the depth of the F-center decreases with increasing temperature. By 240 K the peak of the F-center absorption is at 460 nm, and at 260 K, M-centers begins to spontaneously grow, as the higher temperatures allows the F-centers to mobilize and begin to coalesce (Figure 3.2).

The difference between these experiments and the results of Poston *et al.* [13] are striking. We obtain a significantly shorter wavelength for the F-center, and we see no spontaneous spectral change post-irradiation until we purposely raise the temperature. We hypothesize that these differences are due to a lack of adequate thermal coupling between the salt grains and the cold finger in the Poston *et al.* [13] experiments. The angular grains have little contact with each other or with the cold finger and are exposed to thermal emission from the walls of the experimental chamber. These grains could be at a significantly higher temperature than the copper sample cup and the cold finger. By embedding the samples in indium foil, as was done in the present experiments, the thermal coupling is greatly increased. To test this theory, we irradiated salts in the same manner as before, but without pressing the sample into indium foil. We found that the central wavelength shifted to 460 nm, and the growth of both the F-center and M-center occurred on much faster time scales when compared to spectra at 120K (Figure 3.3). As a final test, we irradiated indium-pressed thermally coupled salt grains at 200K. For these spectra the central wavelength was observed at 458 nm. There was no discernible shift in the central wavelength post irradiation but a slight growth in the M-center was observed post irradiation. The peak of the absorption for these 200K experiments was blueward of both the Poston *et al.* [13] spectra as well as our experiments without pressing the salt into the indium foil (Figure 3.3). Based on these experiments, we hypothesis that the grains in the Poston *et al.* [13] experiments were not well coupled to the cold finger. We believe they were approximately $\sim$ 240K, based on the central wavelength and the growth of the M-center. This higher temperature would naturally lead to the redward shift of the F-center and the post-irradiation spectral changes observed in those experiments but not observed in our thermally coupled 120 K experiments. We conclude that the shift in the F-center between Europa and laboratory data is not due to the increased irradiation in the laboratory, but rather from the inadvertently elevated sample temperature in the previous laboratory data. For thermally coupled samples at 120K, the central wavelength of 451 nm is within the uncertainty of the positional measurement of the feature on Europa. The position we observed also coincides with the central wavelength previously measured for these temperatures [10, 16].

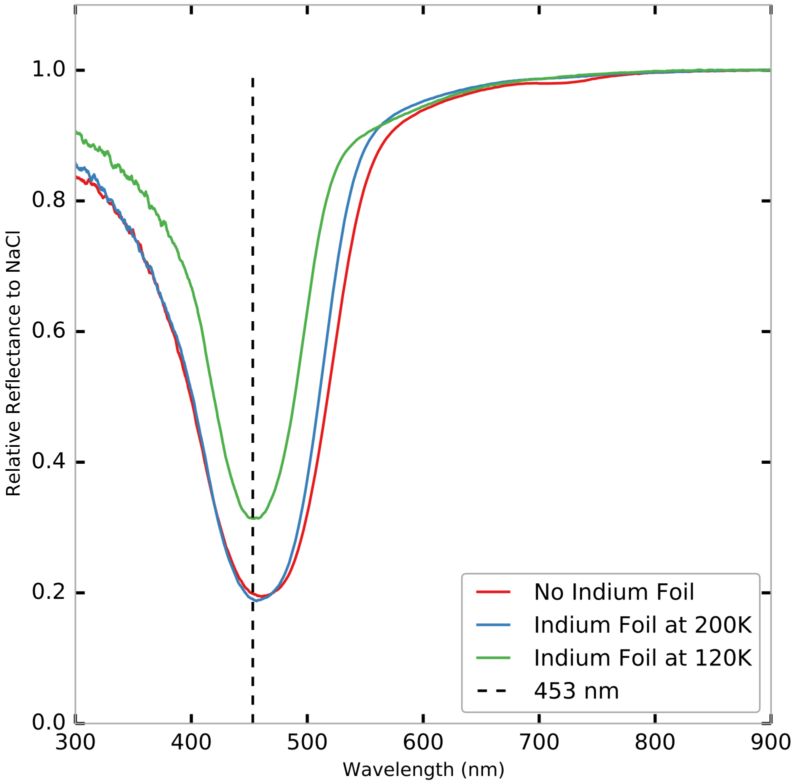

Figure 3.3: Spectra of NaCl irradiated at medium irradiation for 15 minutes. Significant differences are seen in samples with indium foil at 120K, and 200K, and without indium foil. F-center growth is significantly faster for the 200 K and no-indium foil samples, while the F-center wavelength is also shifted redward. For the no-indium foil sample, M-center growth can already be seen. We conclude that the sample sitting on a 120 K cold finger but without indium foil to thermally couple it is even warmer than 200 K.

M-Center Formation

The second critical difference between the laboratory and HST data is the strong growth in the laboratory of the M-center absorption feature located at 720 nm compared to its non-detection from HST. Trumbo *et al.* [9] hypothesized that photobleaching, the destruction of F-center color centers by photons, could suppress the formation of F-centers sufficiently that M-centers, which require a certain density of F-centers in order to coalesce, might never form. To test the magnitude of this photobleaching effect, we performed two sets of experiments. The first was a series of experiments with and without photobleaching at three different irradiating levels. For photobleaching we use the same lamp as is used for spectral reflection. Our lamp provides roughly 8% of the photon flux density in the 400 to 500 nm wavelength span of the F-center compared to noon at Europa's equator. At all irradiation levels, photobleaching slowed the growth of the F-centers, as can be seen in the comparison between photobleached and non-photobleached spectra with otherwise identical conditions in Figure 3.4. To additionally examine this effect, we measured the mean absorption depth of the F-center from 425 to 475 nm as a function of time for each of our irradiation experiments. As seen in Figure 3.5, the average absorption depth of the F-center is dependent on both electron flux and whether or not there is photobleaching. The growth rate of the F-centers, without photobleaching, is approximately linear until saturation occurs and the formation of M-centers begins. This linear region is poorly resolved in the medium and high irradiation experiments, but if we take the 5.6% absorption growth in the first 20 minutes of the low irradiation experiment to be typical of the quasi-linear growth regime, we find a growth rate of 17% hr^{-1}. Scaling by the irradiation flux gives consistent results for the medium and high irradiation levels. We thus assume that for small F-center absorption depths, the growth of the absorption depth, A, can be described as a simple linear growth, $dA/dt = aF$. Here, F is the irradiation flux in units of $\text{ev}/16\text{amu}/\text{yr}$, where the flux at Europa is ∼10, and a is a constant, here found to be 6.8×10^{-5} in the same units as F and with t in hours. At the flux of Europa, a ∼7% absorption feature would grow in a little more than one orbital period in the absence of competing effects.

It is difficult to simultaneously match the photon and electron flux at Europa with our experimental setup. Even our lowest level of irradiation is ∼250 times that experienced at Europa, while our photobleaching photon flux density is ∼13 times *l*ess. Moreover, every time we take a spectrum we are photobleaching for the ∼1 minute duration of the spectral exposures. Thus even the unbleached spectra have actually had some amount of photobleaching. For these reasons, it is difficult to extrapolate the results of Fig. 3.5 to estimate the effect at Europa.

To attempt to obtain a better estimate of the effect of photobleaching on Europa, we performed one additional experiment. We irradiated a sample at four times our low

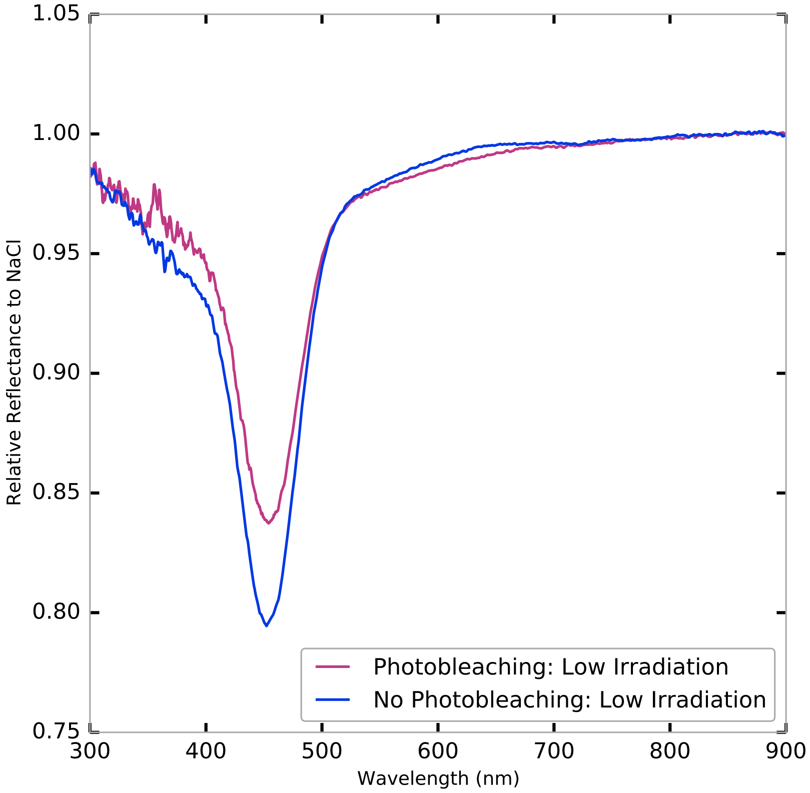

Figure 3.4: Spectrum of NaCl irradiated at low irradiation for 40 minutes with and without photobleaching. The central wavelength is the same for both spectra.

irradiation flux for 10 minutes, leading to an F-center with a fractional absorption depth of about 20%, approximately three times that seen on Europa. We then ceased irradiation and began photobleaching. The F-center absorption decayed rapidly for the first few hours (Fig. 3.6). By the time it reached values more comparable to those seen on Europa, the decay slowed, and we fit this section of the curve to the theoretically derived and experimentally verified equation for photobleaching of lightly irradiated NaCl, $dA/dt = -bIA^2$, where A is the fractional absorption depth of the F-center, I is the intensity of the light, and b is a constant. [11]. We find a value of 0.035 for the product bI for our lamp, which scales to 0.46 for the noon time equatorial solar flux at Europa.

We used this photobleaching equation and an assumed linear growth rate of F-centers with irradiation to estimate an equilibrium value of F-center absorption depth. We model the F-center growth rate as $dA/dt = aF - bIA^2$. In steady-state and

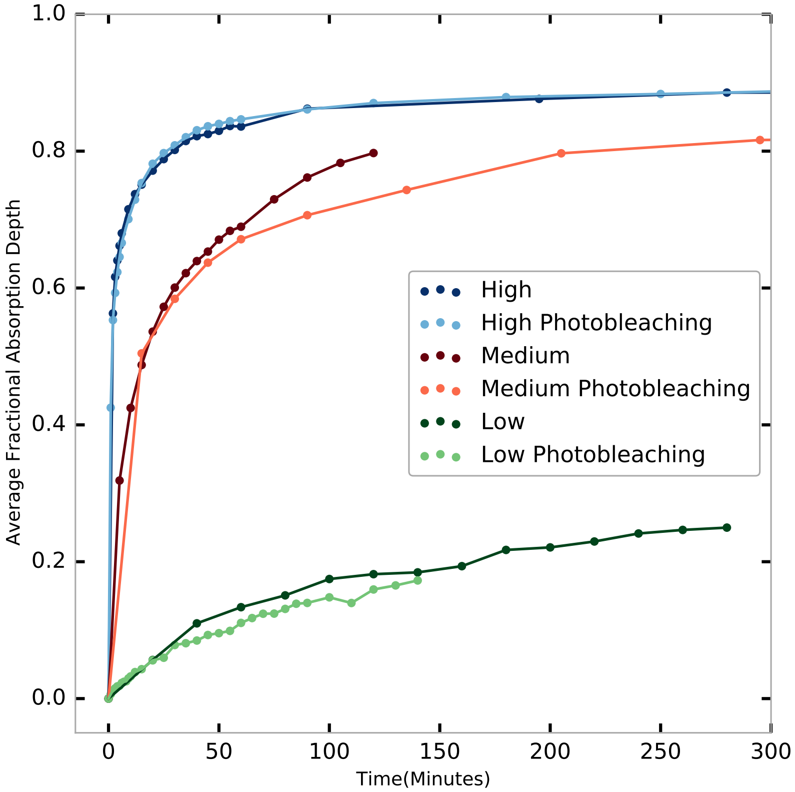

Figure 3.5: The average fractional absorption depth of the F-center from 425 to 475 nm vs time of irradiation for our three irradiation levels, with and without photobleaching. In all cases, photobleaching slowed the growth of the F-centers, though the lamp is too weak to completely balance even the lowest electron irradiation level.

assuming continuous photobleaching at the average equatorial day/night irradiance, this equation predicts an absorption depth of 6.8% for Europa. This calculated value is remarkably similar to the depth seen in the HST data. Crucially, such an equilibrium value for the F-center is much lower than that seen to be required for formation of M-centers. In reality, photobleaching is not constant on Europa, but ranges from zero during the night to a maximum at noon. Incorporating this changing photobleaching rate into a simple numerical model which accounts for nighttime and sinusoidally varying illumination in the daytime suggests that, in equilibrium, the F-center absorption depth would grow to 8.7% overnight, decay to 5.6% by the end of the day, and regrow overnight (Figure 3.7).

Intriguingly, the HST data on Europa show evidence for this precise photobleaching effect. While Trumbo *et al.* [9] report only average values for the F-center strength across the disk, we note that a portion of Tara Regio was observed both in the morning and in the afternoon. Reproducing their data reduction, but examining overlapping spectra separately, we find that the morning absorption depth is indeed deeper than that of the afternoon. These absorption depths are well fit by our simple time-dependent mode. Given the crudeness of the modeling and the difficulty of extrapolating laboratory conditions to those at Europa, we believe that the extremely close agreement between the precise values of the model and of the data must be mainly coincidental. Nonetheless, we find the fact that the relative change in the F-center absorption depth from HST agrees with the model to be an encouraging sign that our extrapolations to Europa's surface conditions and crude modeling are capturing the real behaviour at Europa.

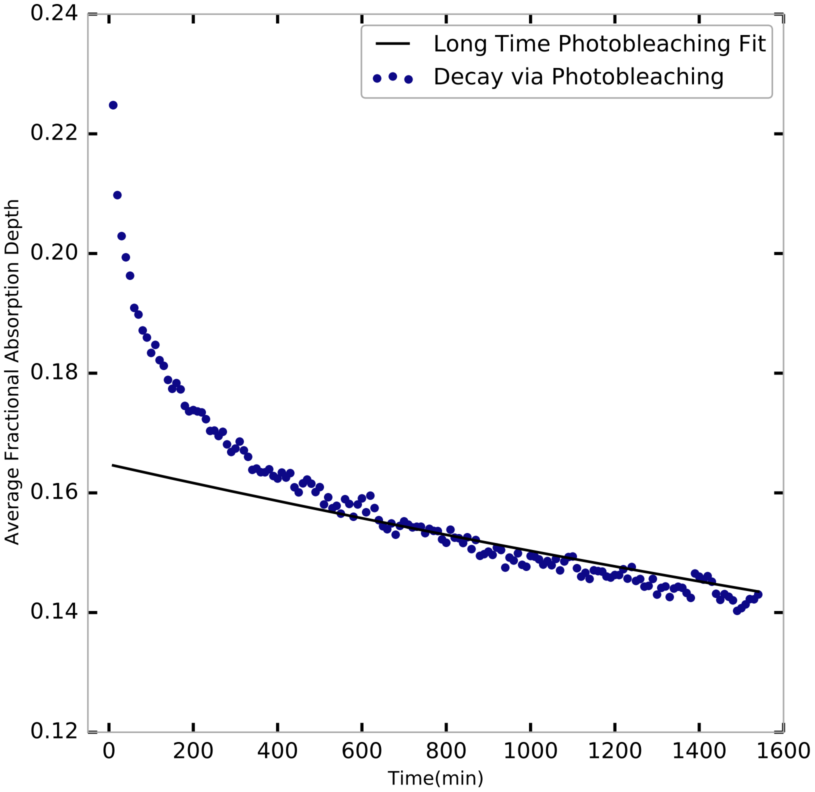

Figure 3.6: The average fractional absorption depth of the F-center from 425 to 475 nm with photobleaching post irradiation.

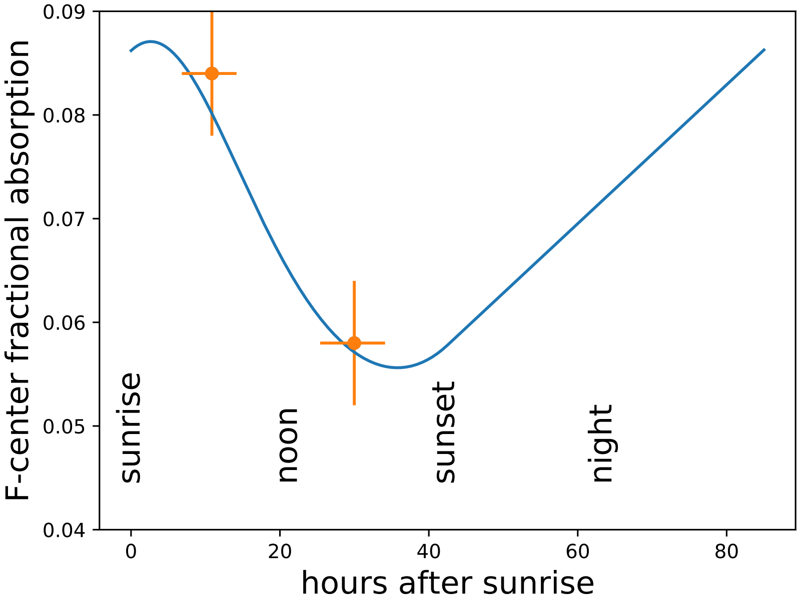

Figure 3.7: A simple numerical model showing the F-center fractional absorption as a function of Europa's 85 hour rotation period, including the effects of continuous irradiation on Europa with solar flux dependent photobleaching during the daytime. The F-center grows over the course of the night and begins decaying soon after sunrise before recovering after sunset. The data points show the absorption depths of two HST measurements of identical regions within Tara Regio taken at different local times. The horizontal error bars show the geographic extent of the observed region. The F-center decay predicted by the model is observed on Europa.

3.5 Conclusions

We used new laboratory data with carefully controlled temperature and photon illumination conditions to examine the discrepancy between the spectrum of the Tara Regio region on Europa measured with HST and the spectrum of irradiated NaCl found in previous laboratory work. We found that in our experiments irradiated NaCl grains, which are thermally coupled to a 120 K cold finger by pressing them into indium foil, develop F-center absorptions at 451 nm, matching the spectral feature on Europa, rather than at the 460 nm wavelength seen in previous experiments. Absorption at 460 nm is, however, seen when samples are placed on the cold finger without pressing into the foil and when thermally-coupled samples are heated to 240 K. We conclude that previous experiments had poor thermal coupling between the cold finger and the angular salt grains resting on a cold finger, resulting in a raised sample temperature of approximately 240 K. At the appropriate temperature, the

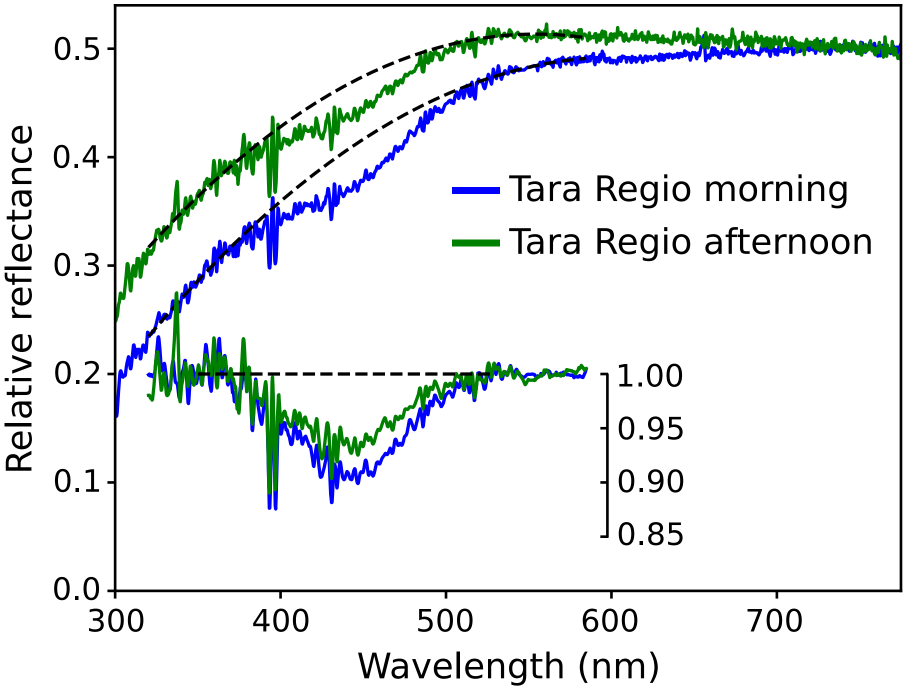

Figure 3.8: HST observations of overlapping regions of Tara Regio in the morning and in the afternoon. Dashed lines are second-order polynomial continuum fits, which facilitate band-strength comparison. The continuum-removed absorption bands are shown below. The observed decay in the F-center absorption is consistent with the photobleaching decay predicted here.

band position of laboratory-irradiated NaCl at 451 nm falls within the uncertainty of the band position on Europa.

Previous laboratory data also predicted the presence of M-center absorption at 720 nm on Europa for typical irradiation doses expected, but the HST data put strong upper limits on the existence of such an absorption. Here we found that photobleaching — the destruction of F-centers by photons — can nearly precisely balance the irradiation-induced creation of F-centers, leading to a low equilibrium value for F-center density and a weak absorption strength, similar to that seen on Europa. This low equilibrium density is well below the density required for pairs of F-centers to begin to coalesce to form M-centers, explaining the lack of this additional absorption on Europa.

Our model for F-center creation and destruction predicts that the absorption will grow overnight in the absence of photobleaching and partially decay during the day under solar illumination. We show that morning and afternoon spectra of Tara Regio, when examined separately, show this effect at a similar level as predicted.

These new laboratory experiments show that the visible spectrum of Tara Regio is consistent with the presence of irradiated NaCl, including the wavelength of the F-center feature, the lack of an M-center absorption at 720 nm, and the change in the strength of the F-center feature over the course of the day. The existence of NaCl in a chaos region on the leading hemisphere of Europa strongly suggests that sodium and chlorine are dominant components of the subsurface of Europa.

3.6 Acknowledgements

This research was supported by a grant number 668346 from the Simons Foundation. The observations were made with the NASA/ESA Hubble Space Telescope, obtained at the Space Telescope Science Institute, which is operated by the Association of Universities for Research in Astronomy, Inc., under NASA contract NAS5-26555. These observations are associated with program #14650. This work is also associated with archival program #15789. This data was obtained from the Mikulski Archive for Space Telescopes (MAST). This specific observations analyzed can be accessed via dataset[10.17909/t9-awev-6407]https://doi.org/10.17909/t9-awev-6407. Support for program #15789 was provided by NASA through grants from the Space Telescope Science Institute, which is operated by the Association of Universities for Research in Astronomy, Inc., under NASA contract NAS5-26555. S.K.T. is supported by the Heising-Simons Foundation through a *51 Pegasi b* postdoctoral fellowship.

References

1. Kivelson, M. G. Galileo Magnetometer Measurements: A Stronger Case for a Subsurface Ocean at Europa. *Science* **289,** 1340–1343. doi:`10.1126/science.289.5483.1340` (Aug. 25, 2000).
2. Paranicas, C., Carlson, R. W. & Johnson, R. E. Electron bombardment of Europa. *Geophysical Research Letters* **28,** 673–676. doi:`10.1029/2000GL012320` (2001).
3. Paranicas, C., Ratliff, J. M., Mauk, B. H., Cohen, C. & Johnson, R. E. The ion environment near Europa and its role in surface energetics. *Geophysical Research Letters* **29,** 18–1–18–4. doi:`10.1029/2001GL014127` (2002).
4. Kargel, J. S. *et al.* Europa's Crust and Ocean: Origin, Composition, and the Prospects for Life. *Icarus* **148,** 226–265. doi:`10.1006/icar.2000.6471` (Nov. 2000).
5. Carr, M. H. *et al.* Evidence for a subsurface ocean on Europa. *Nature* **391,** 363–365. doi:`10.1038/34857` (Jan. 1998).

6. Glein, C. R. & Shock, E. L. Sodium chloride as a geophysical probe of a subsurface ocean on Enceladus. *Geophysical Research Letters* **37.** doi:`https://doi.org/10.1029/2010GL042446` (2010).
7. Schmidt, B. E., Blankenship, D. D., Patterson, G. W. & Schenk, P. M. Active formation of 'chaos terrain' over shallow subsurface water on Europa. *Nature* **479,** 502–505. doi:`10.1038/nature10608` (Nov. 2011).
8. Soderlund, K. M., Schmidt, B. E., Wicht, J. & Blankenship, D. D. Ocean-driven heating of Europa's icy shell at low latitudes. *Nature Geoscience* **7,** 16–19. doi:`10.1038/ngeo2021` (Jan. 2014).
9. Trumbo, S. K., Brown, M. E. & Hand, K. P. Sodium chloride on the surface of Europa. *Science Advances* **5,** eaaw7123. doi:`10.1126/sciadv.aaw7123` (June 2019).
10. Mador, I. L., Wallis, R. F., Williams, M. C. & Herman, R. C. Production and Bleaching of Color Centers in X-Rayed Alkali Halide Crystals. *Physical Review* **96,** 617–628. doi:`10.1103/PhysRev.96.617` (Nov. 1, 1954).
11. Herman, R. & Wallis, R. F. Optical Bleaching of F Centers in X-Rayed Alkali Halide Crystals. *Physical Review* **99,** 435–442. doi:`10.1103/PhysRev.99.435` (July 15, 1955).
12. Hand, K. P. & Carlson, R. W. Europa's surface color suggests an ocean rich with sodium chloride. *Geophysical Research Letters* **42,** 3174–3178. doi:`10.1002/2015GL063559` (2015).
13. Poston, M. J., Carlson, R. W. & Hand, K. P. Spectral Behavior of Irradiated Sodium Chloride Crystals Under Europa-Like Conditions. *Journal of Geophysical Research: Planets* **122,** 2644–2654. doi:`10.1002/2017JE005429` (2017).
14. Hibbitts, C., Stockstill-Cahill, K., Wing, B. & Paranicas, C. Color centers in salts - Evidence for the presence of sulfates on Europa. *Icarus* **326,** 37–47. doi:`10.1016/j.icarus.2019.02.022` (July 2019).
15. Nordheim, T. A., Hand, K. P. & Paranicas, C. Preservation of potential biosignatures in the shallow subsurface of Europa. *Nature Astronomy* **2,** 673–679. doi:`10.1038/s41550-018-0499-8` (Aug. 2018).
16. Schwartz, K. *et al.* Effect of electronic energy loss and irradiation temperature on color-center creation in LiF and NaCl crystals irradiated with swift heavy ions. *Physical Review B* **78,** 024120. doi:`10.1103/PhysRevB.78.024120` (July 30, 2008).

Chapter 4

LABORATORY SPECTROSCOPY OF SULPHATES PREDICTED ON EUROPA

4.1 Abstract

The alteration of epsomite ($MgSO_4 \cdot 7\,H_2O$), mirabilite ($Na_2SO_4 \cdot 10\,H_2O$) and thénardite (anhyd. Na_2SO_4), at conditions resembling the surface of Europa, has been studied spectroscopically. Diffuse reflectance spectroscopy across 230 to 900 nm and 1.25 to 6 µm is performed on salt grains of regulated sizes. UV-Vis spectra have been compared with observations of Eastern Annwyn and Dyfed chaos terrain regions on the trailing hemisphere of Europa by the Hubble Space Telescope while FT-IR laboratory spectra have been compared with observational data from NIRSPEC of Keck II. Sulphates are plausible species on Europa's trailing hemisphere given the presence of iogenic sulphur and abundant water ice on Europa, alongside chemistry driven by radiolysis and electron-ion bombardment. A characteristic darkening of Na_2SO_4 (anhydrous and hydrated) following irradiation with 10 keV electrons, has been observed, with the rate of spectroscopic changes having a dependence on temperature. Epsomite displays no such darkening. Irradiated epsomite resembles the HST observations in the Visible regime, although there is no exact match. Thénardite and progressively dehydrated mirabilite absorb at 3.8 to 3.85 µm which is slightly red-shifted with respect to the absorption at 3.78 µm observed on Europa.

4.2 Introduction

Europa's surface is radiolytically altered due to intense bombardment, causing new chemistry to occur, observable in terms of spectroscopic features. The salts present in Europa's ocean presumably arise from interactions between liquid water and the silicate seafloor [1]. A distinct color difference exists between the leading and trailing hemispheres, with the trailing hemisphere appearing significantly darker and redder. This appears to arise from the alteration via radiolysis involving exogenic sulphur [2, 3]. Sulfur ions from the volcanoes of Io co-rotate with Jupiter's magnetic field and are then deposited on Europa's trailing hemisphere, driving a radiolytic sulfur cycle on the trailing hemisphere [4]. Various other charged particles: electrons, ions, and protons also impact Europa. Chaos terrain (recently resurfaced areas) provide insight into the interaction of this radiolytic sulfur with species believed to be present in Europa's ocean. One of these suspected radiolytic species, sulfuric acid, has been observed on the surface of Europa [5]. The observation of salt products like sodium chloride [6] and the presence of sulfuric acid [5] suggests the presence of exogenic sulphates. The 450 nm sodium chloride feature seems localised to the leading hemisphere [7], apparently separated, from the radiolytic sulfur chemistry. Sulfates have been presented as a possible component of Europa's ocean [1, 8, 9] but the features localised to the trailing hemisphere suggest a lower abundance than previously suggested [10]. Spectra from NIRSPEC on the Keck II telescope presented a 3.78 µm feature which was localized to the trailing hemisphere [11]. This feature is suggested to be an unknown radiolytic product. The trailing hemisphere also exhibits a 2.07 µm feature which is spatially correlated with radiation products and presents a strong spectral match to either $MgSO_4$ brine or the mineral form epsomite ($MgSO_4 \cdot 7\,H_2O$).

Previous laboratory data produced sulfuric acid via electron bombardment [12]. Laboratory experiments have previously been conducted on possible sulfate salts at cryogenic temperatures [13, 14] and irradiation with electrons [15, 16] but not in tandem. In this work we performed cryogenic electron irradiation of suspected sulfate salts at temperatures and pressures akin to Europa.

4.3 Methods

Our experiments are set up to measure spectra of magnesium sulfate ($MgSO_4$) and sodium sulfate (Na_2SO_4). For sodium sulfates, mirabilite ($Na_2SO_4 \cdot 10\,H_2O$) and thénardite (anhyd. Na_2SO_4) are tested. The experimental procedure is adjusted to maintain hydration state. Magnesium sulfate could be present as epsomite ($MgSO_4 \cdot 7\,H_2O$) as well as an anhydrous species. Recent data shows the presence of meridianiite ($MgSO_4 \cdot 11\,H_2O$) at cold temperatures [17] which may also be present on Europa. All samples were pressed into indium foil in copper sample cups with excess salt removed to ensure strong thermal conductivity. Anhydrous samples were ground under nitrogen atmosphere and hydrated samples were ground under ambient atmosphere. Samples were then sieved to sub 100 microns. This allowed for consistent grain size across samples and comparison to De Angelis *et al.* [14]. The sample cups were transferred to the cold finger of a closed cycle helium cryo-cooler (Advanced Research Systems DE-202AB), housed in a Kimball Physics UHV system. The chamber was pumped down to below 10^{-8} torr using an Agilent ID3 backing pump and TwisTorr 84 turbomolecular drag pump. Once the desired temperature was reached, the grains were irradiated with 10 keV electrons from a Kimball Physics

EGG-3101 electron gun. The current was measured with a Kimball Physics Faraday cup mounted on a linear actuator that can be inserted into the electron beam path. Due to the likelihood of these sulfates arising from aqueous systems, control and consistency of hydration state are critical. To investigate the hydration state, the order of evacuation and cooling is varied. For anhydrous samples, the system is placed under vacuum without cooling until the water features, which are observed via infrared spectroscopy, are removed. Visible spectra is collected via an external lens fed by a fiber optic connected to a stabilized deuterium and a stabilized tungsten-halogen lamp from Thorlabs. We illuminated the sample at 45° from the surface normal and collected the diffuse reflection 90° from the specular direction and 45° from the surface normal. Infrared spectra are collected in the same geometry using a Nicolet IS 50 with an external liquid nitrogen cooled Mercury Cadmium Tellurium (MCT-A) detector.

4.4 Experiments

Sample Preparation

All experiments were conducted in the PICL (Planetary Ice Chemistry Lab) UHV chamber with 10 keV electron irradiation. Samples were ground to sub 100 μm grain sizes with a mortar and pestle. Due to experience on thermal coupling from previous experiments in the setup, the grains were packed into copper sample cups lined with a thin layer of indium foil [6]. This greatly improves thermal conductivity. Anhydrous samples were placed into the chamber at 293 K and then pumped down to sub $10^{-7}\,\mathrm{torr}$. The samples remained at vacuum for 36 hours to remove any water absorbed during preparation. Hydrated samples are placed in a precooled chamber under nitrogen atmosphere until the thermocouple is sub 223K at which point, the roughing pump is turned on. Once the thermocouple reaches 100 K the turbo-molecular pump is then turned on. This does cause the deposition of water vapor on top of the sample but helps maintain hydration state. Due to mirabilite's affinity for dehydration, the mirabilite samples were placed in an environment of 80% humidity to preserve hydration.

4.5 Visible Data

Sodium Sulfates

Electron irradiation was conducted on sulfate species assumed to be present on Europa. Thénardite (Na_2SO_4 An) was irradiated at 100 K as well as at 293 K while mirabilite ($Na_2SO_4 \cdot 10\,H_2O$) was irradiated at 100 K. At high vacuum, when not at

Table 4.1: Sulfate Experiments

	Current Density (nA/cm^2)	Electron Flux (electrons/cm^2/s)	dose rate (eV/16amu/yr)	temperature (K)	Wavelength Range (nm)
$Na_2SO_4 \cdot an$	3410	2.13×10^{13}	7×10^5	293	230-6000
$Na_2SO_4 \cdot an$	3410	2.13×10^{13}	7×10^5	100	230-6000
$Na_2SO_4 \cdot 10\,H_2O$	3410	2.13×10^{13}	7×10^5	100	230-6000
$MgSO_4 \cdot 7\,H_2O$	3410	2.13×10^{13}	7×10^5	100	230-6000
Europa	n/a	n/a	78	120	

Note - The energy deposited is for the top 1.2 μm micron of the sample. Hydration state is given for the purchased sample. For Europa, the photon flux and temperature are given for equatorial noon.

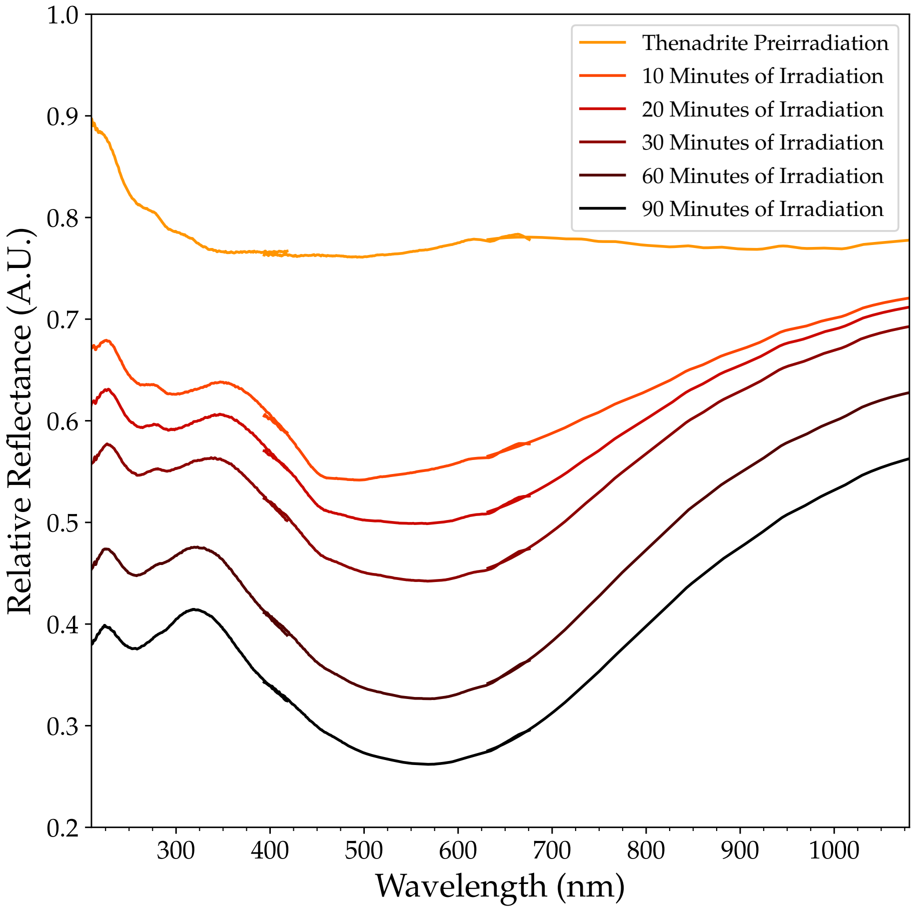

Figure 4.1: Irradiation of thénardite at 293 K with 10 keV electrons. Spectra are dark subtracted and divided by Labsphere Spectralon standards. Significant darkening is observed in the UV and Visible. The spectra is collected separately for the visible and UV regions and then combined with overlap occurring at approximately 400 nm.

cryogenic temperatures, mirabilite dehydrates quickly, implying that discriminating dehydration due to irradiation from that due to evacuation is not possible. Room temperature irradiation of thénardite showed a drastic decrease in reflectivity in both the visible and UV wavelengths as shown in Figure 4.1. Our spectra are in agreement with those reported previously following irradiation with Hibbitts *et al.* [15]. The downturn observed from 350 to 550 nm is unique to sodium sulfates and is not observed on Europa. The band-minimum shifts from 450 to 580 nm, with irradiation. Cryogenic irradiation of thénadrite produces a shape similar to room temperature experiments but at much longer time scales, in other words, irradiation causes changes more rapidly at room temperatures than at cryogenic temperatures. This is a phenomenon similar to that observed with sodium chloride. A decrease in absorption is observed with a stronger feature present at 277 nm. The strength of this feature decreases with irradiation compared to other irradiation changes. We observe a down turn from 350 to 550 nm but less prominent in comparison to warm thénardite. A shift in band minimum occurs for the 450 feature but it is less prominent than the shift observed for the room temperature irradiation. Spectral changes indicative of photobleaching were not observed. There was a change in band depth post irradiation but it remained consistent with and without photon impingement. A slow relaxation, more pronounced in the visible portion of the spectra compared to the UV, was observed when the irradiation was ceased. The degree of relaxation dropped with increased irradiation. On Europa, irradiation is continuous so no relaxation would be visible spectroscopically.

Mirabilite ($Na_2SO_4 \cdot 10\,H_2O$) is unstable on earth but with a high concentration of water ice and cryogenic temperatures its presence is possible on Europa. Due to dehydration at terrestrial conditions we rehydrated the samples at 80 % humidity and measured the hydration state, before irradiation, via FTIR. Mirabilite was not run at 293 K due to its propensity to dehydrate thus creating similar sample conditions to those exhibited by thénadrite. Cryogenic irradiation exhibited a smaller decrease in reflectivity as compared to cryogenic thénardite. A spectral feature at 265 nm is evident before irradiation which grows in strength with irradiation. The hydrated sodium sulfate seems to show an analogous but broader feature in comparison to thénardite. The downturn in the 300 nm range is slightly shifted blueward with respect to, both cryogenic and room temperature thénardite. This features broadens with increased irradiation. The wavelength center of the broad feature is relatively consistent across different hydration states but takes longer to develop with the hydrated sodium sulfate. This could be related to either temperature or hydration state. Hibbitts *et al.* [15] referred to the feature at 610 nm, which causes the spectral upturn to 300 nm, as a color center but did not identify its cause. Due to the broad nature of the features it is unlikely that these color centers are formed via interstitial holes. All species were irradiated until this feature reached a reflectivity of around 0.2 compared to spectralon, instead of a fixed duration of irradiation. Temperatures, as was seen in previous work [6], plays a large role in the effect of irradiation. Unlike with sodium chloride, there was no suppression of spectral features formation with irradiation at cryogenic temperatures. The presence of this spectral upturn from 500

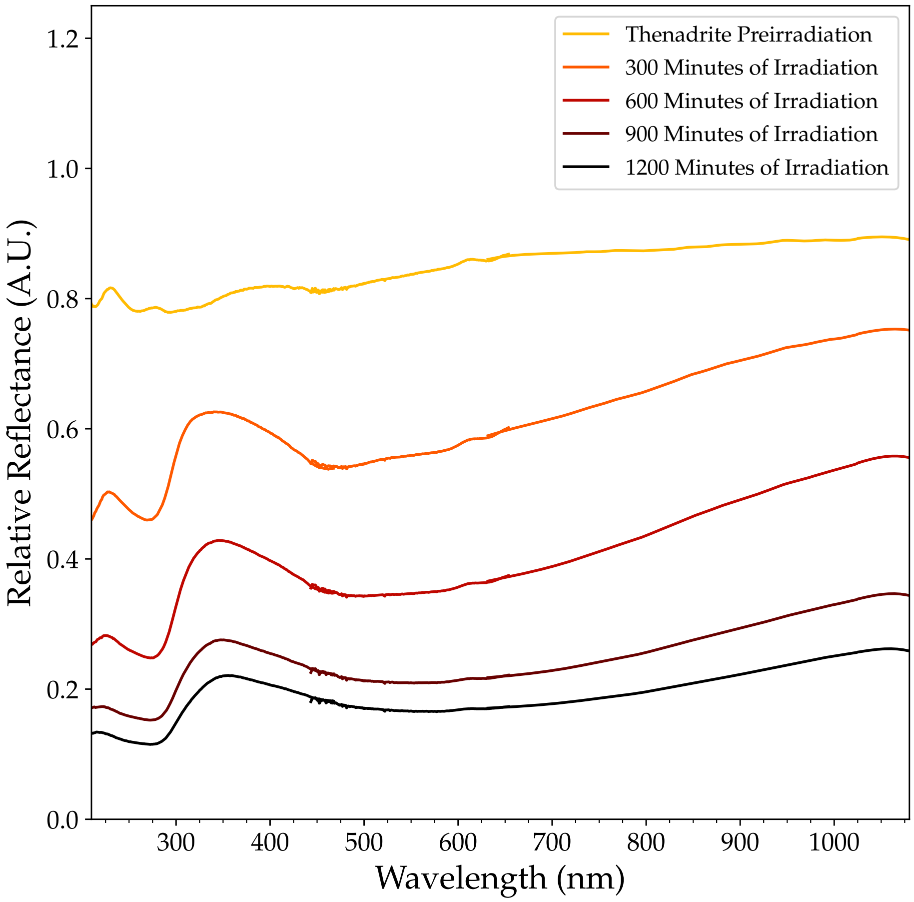

Figure 4.2: UV/VIS spectra for the irradiation of thénardite at 100 K with 10 keV electrons. Darkening is observed with irradiation with the strength of the 277 nm and the 466 nm peaks decreasing in intensity with longer irradiation compared to earlier time steps.

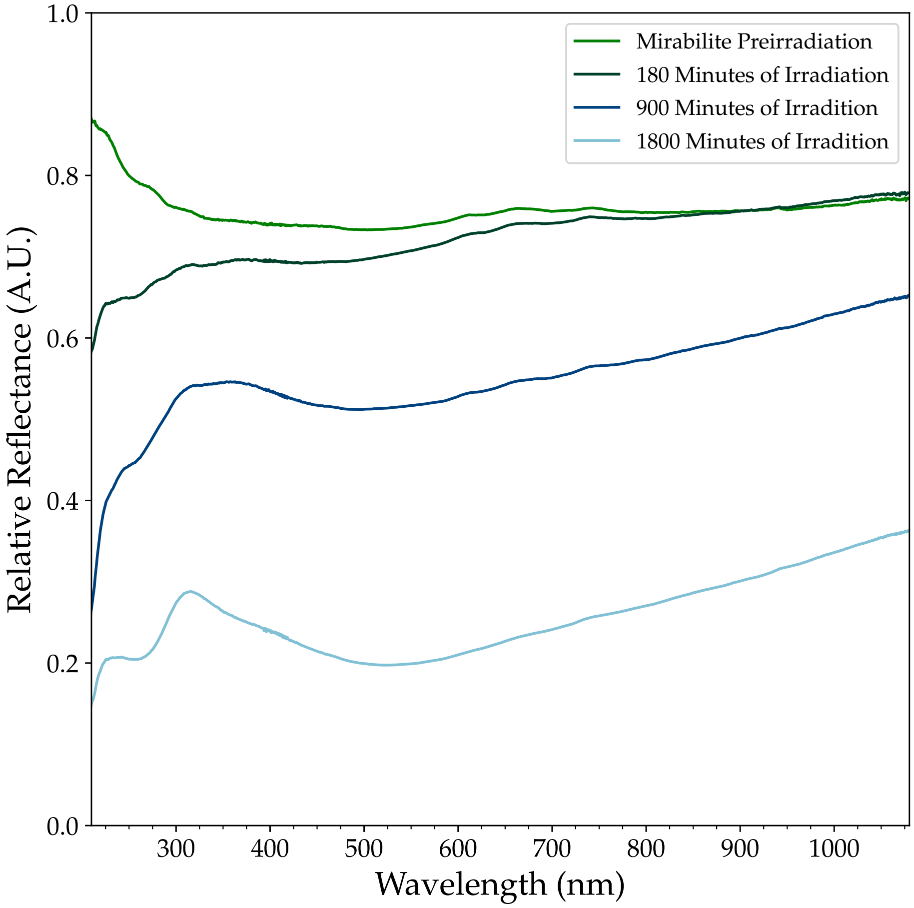

Figure 4.3: UV/VIS spectra for the irradiation of mirabilite at 100 K with 10 keV electrons. Hydration state does not seem to have a large effect on irradiation changes. The band minimum is red shifted compared to thénadrite but an upturn is still observed.

nm to 300 nm for all sodium sulfate is not observed on the trailing hemisphere of Europa. The reddish coloration of the trailing hemisphere does not agree with the irradiated sodium sulfate. All sodium sulfates take on a dark gray hue with irradiation. This evidence does not eliminate the possibility of sodium sulfate on Europa but does diminish its likelihood. Large scale and geologically-quick recycling of the surface would have to occur to eliminate the upturn we observe in laboratory spectra.

Epsomite

Irradiation of Epsomite ($MgSO_4$ 7 H_2O) was conducted at cryogenic temperatures. A systematic downturn was observed on continued irradiation, with a feature developing at 360 nm. A downturn begins at 700 nm as compared to spectralon but a larger effect occurs on the UV portion of the spectra with increased electron impingement. Relaxation was observed after irradiation stopped but spectral change indicative of photobleaching did not occur. After 1200 minutes of irradiation a 360 nm feature is visible, altering the spectral slope. The spectral slope in the region from 240 to 375 shifts from linear to almost parabolic at longer time-periods. A change in spectral slope also occurs at 560 nm. As compared to warm irradiation, we observe a blue shifted downturn in the spectra as compared with previous irradiation experiments. Hibbitts *et al.* [15] observed a slope change at 600 nm with dehydrated, warm magnesium sulfate. The change in downturn position could be due to difference in hydration or temperature. If temperature dependent, the irradiation mechanism that causes this feature would occur at higher temperatures and with higher electron impingement. This would suggest that there are two different mechanisms causing the spectral changes much like F-centers and M-centers present in sodium chloride. No distinct color centers are formed in the wavelengths measured making determination of the cause of the spectral features difficult. Gamma irradiation was able to produce SO_3^- radicals, as observed with ESR, but no visible spectroscopy was taken [18]. Sulfate radicals would cause a spectroscopic change but we are unable to confirm the production of these radicals with electron irradiation.

Anwynn and Dyfed Regions

The change in spectral slope that occurs with irradiation of sodium sulfates is not observed on Europa. Observational data from the trailing hemisphere of Europa collected by the Hubble Space Telescope focused on two portions of chaos terrain, Eastern Anwynn and Dyfed. This data has been published in Trumbo *et al.* [19]. A near-UV downturn mapped from 315 to 415, a 360 nm feature, and a 530 nm feature

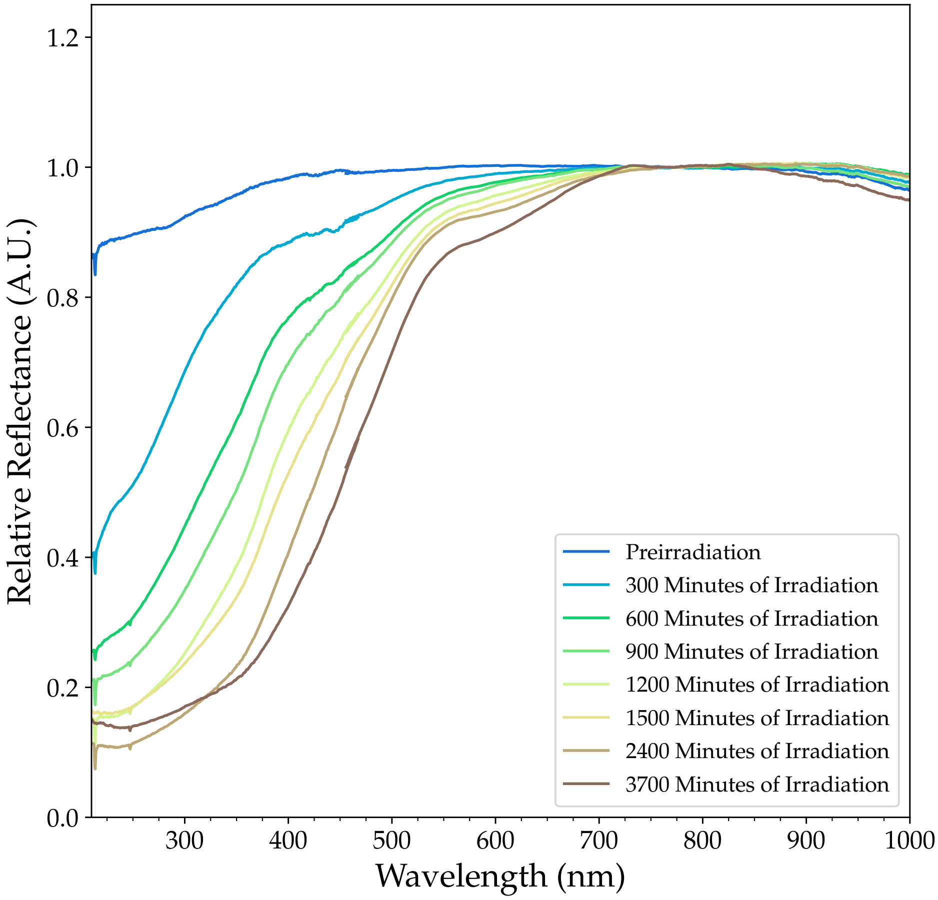

Figure 4.4: UV/VIS Spectra of epsomite at 100 K irradiated with 10 keV electrons. A downturn occurs with irradiation and a shoulder forms at 550 nm. This feature is shifted with irradiation and is blueward of the downturn exhibited on Europa. Flattening occurs in the UV range with high irradiation most likely due to saturation.

were all mapped on Europa's trailing hemisphere. The near-UV downturn appears to map with the exogenic irradiation pattern while the 360 nm feature is strongest in the Dyfed Region, Eastern Annwyn Region, and the intervening smaller-scale chaos terrain. This signal is most likely derived from endogenic species that have undergone sulfur bombardment. The 530 nm feature maps similar to the 360 nm feature but exists at the junction between two HST settings thus decreasing sensitivity. The spectra from Dyfed Region and Eastern Annwyn Region have been compared to our cryogenic laboratory spectra. The upturn observed in the irradiation of sodium sulfate does not agree with the observational data and is thus not included in our comparison. Long term irradiation of Epsomite does have agreement from 800 nm to 530 nm and is shown in Figure 4.5. There is no strong agreement in the UV region. Epsomite does show a downturn but seems to possess a larger absorption feature than the two trailing chaos regions. Our long term irradiation spectra have similar agreement with observational data but lack the extended spectral slope change from 500 to 540 nm. The change in spectral slope for irradiation of epsomite is slightly blueward of the chaos terrain. The growth of the 360 nm feature is a positive sign for spectral matching. The extension of the spectral shoulder on Europa could be due to a mixture of spectral signals due to a species possessing stronger reflectivity interfering with the downturn from sulfates.

4.6 Infrared Spectroscopy

We recently added the capabilities of off-axis diffuse reflectance spectroscopy for fourier transformed infrared (FTIR) light. A Thermofischer Nicolet IS50 spectrometer is the source with a mercury cadmium telluride (MCT/A) liquid nitrogen cooled detector. A custom nitrogen box was built to purge the entire system eliminating CO_2 and water vapor absorptions. Samples of the sulfate salts were prepared in the same manner as for the UV/Visible spectroscopy and also underwent irradiation. Infragold (Labsphere) was used as a spectral standard and the data is divided by Infragold. The infragold spectra were collected at high vacuum, 10^{-7} torr and the beam path was purged with nitrogen. We collected spectra from 1.25 to 6 μm. This allowed the identification of hydration features and comparison to both Keck II and JWST NIRspec observational data. None of the fundamental vibrations of SO_4^- are in this wavelength range but overtones and combinations from sulfate species can be observed. Grain sizes was kept sub 100 micron to maintain consistency as previous work showed variation with grain size for thénardite and mirabilite [14].

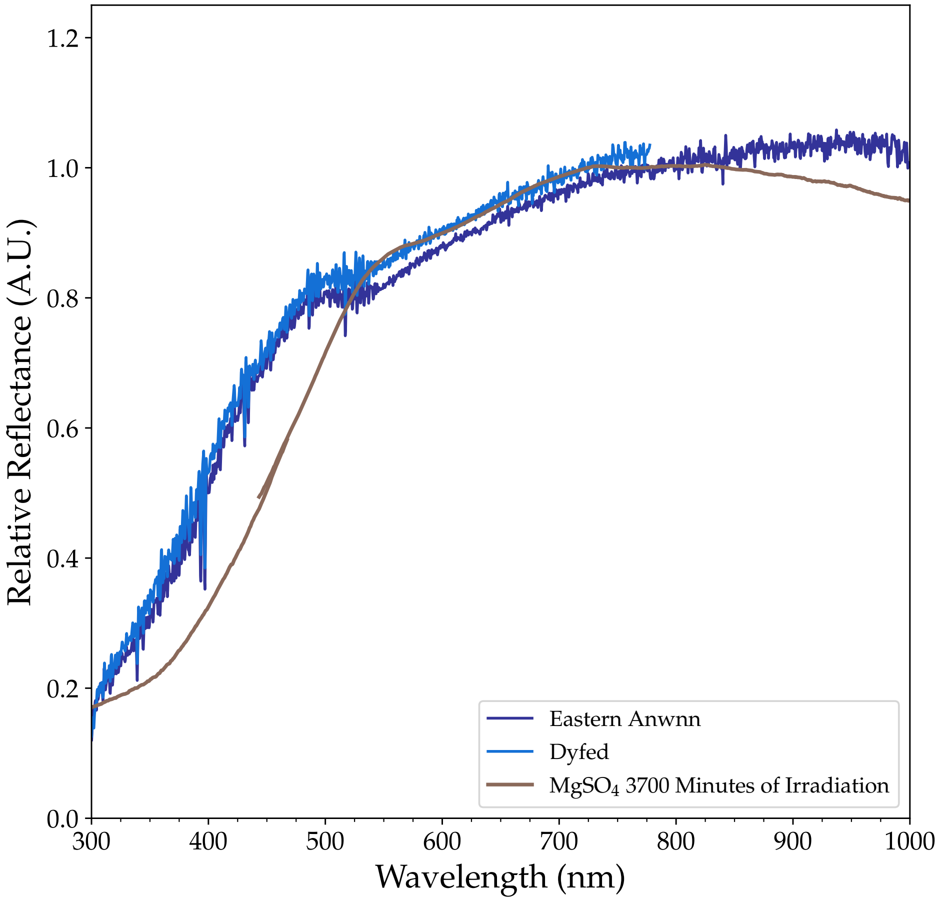

Figure 4.5: Spectra of irradiated epsomite compared with Europa spectra of two trailing chaos terrain spectra. The observational data was collected by the Hubble Space Telescope. Data has been normalized with the laboratory spectra divided by Spectralon. Similar agreement through the visible range and spectral slope in the UV.

Sodium Sulfate FTIR

Sodium sulfate was irradiated as both mirabilite and thénardite at cryogenic temperatures. Our thénardite spectra showed no hydration features and remained stable for 36 hours pre-irradiation. Very limited change is observed with irradiation. A slight decrease is seen at 3 µm after 1800 minutes of impingement which is attributed to the loss of water. For mirabilite, the features at 1.4, 1.75, and 1.95 µmeter decrease with irradiation. This decrease could be caused by irradiation or dehydration due to vacuum exposure. Very little spectroscopic change is observed when the sample remains at high vacuum at 100 K for 24 hours but longer time intervals could produce dehydration without irradiation. This suggests that, on Europa, sodium sulfate would be present as thénardite unless replenished by water. The 1.9 µm peak remains at similar band depth in relation to the 2.47 µmfeature, indicating that they are both from the same water feature. Our thénardite spectra possess no spectral features from 1.2 to 2.6 µm. A sharp feature exists at 2.7 µm. Thénardite does show water overtones feature at 3.42 and 3.5 µm 3.42 and 3.5 microns which is not observed in mirabilite. This is most likely due to the higher hydration masking the signal. This trend continues with thénardite presenting more spectral features with the decreased water bands. Mirabilite presents a feature centered at 5.05 µm with irradiation which is not observed in thénadrite. These features are not observed in USGS Spectral Library for mirabilite and are outside the range presented in De Angelis *et al.* [20]. This feature could be a function of irradiation that requires the presence of hydration within the sodium sulfate structure.

3.78 micron feature

On Europa, a 3.78 µm feature has been observed by the near-infrared spectrometer NIRSPEC on the Keck II telescope [11]. This feature is present on the trailing hemisphere and is consistent with that of a radiolytic product from electron or Iogenic ion bombardment. This absorption is coincident with SO_2 frost observed in both laboratory spectra and spectra of Io. The 4.07 µm feature from SO_2 frost is not observed on Europa. In our sodium sulfate spectra we observe two absorption features near this range. These adsorptions are centered at 3.8 and 3.85 µm, both red-shifted as to that on Europa. They are both more prominent in thénardite as compared to mirabilite due to the signals being masked from hydration in the 3.5 µm portion of the spectra. Mirabilite does start to form a 3.85 µm feature with irradiation, most likely from dehydration decreasing the water band strength. De Angelis *et al.* [20] also observed similar bands which they attribute to SO_4^{2-} (S-O overtones and

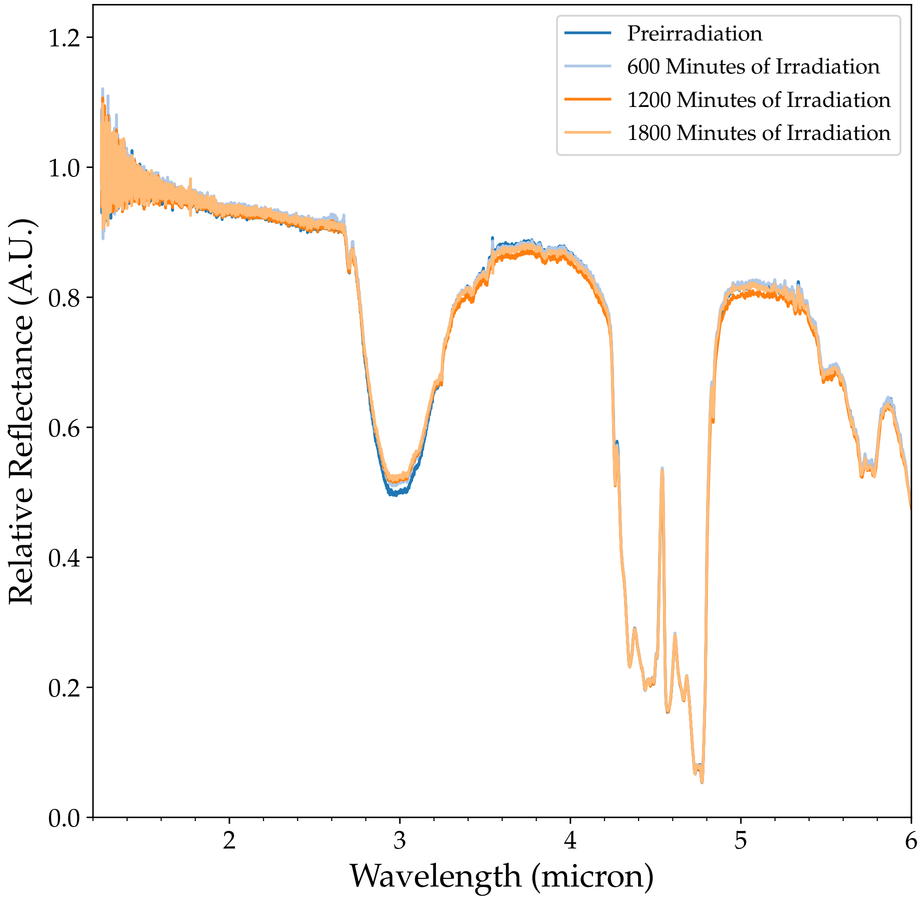

Figure 4.6: Infrared spectra of thénardite irradiated with 10 keV electrons at 100 K. There is limited change with irradiation. The double at 3.8 and 3.85 µm does not undergo changes with irradiation.

combinations). They do not observe two peaks in their mirabilite sample. To better highlight these two features we have applied a third order polynomial fit from 3.71 to 4.1 µm. This third order fit indicates the presence of these two features pre-irradiation and they do not undergo changes with irradiation. These two features do not correlate with SO_2 frost. Due to spectral resolution of the Keck II data a double peak could be present on Europa that is not resolved. The band position does not seem to be temperature dependent [20].

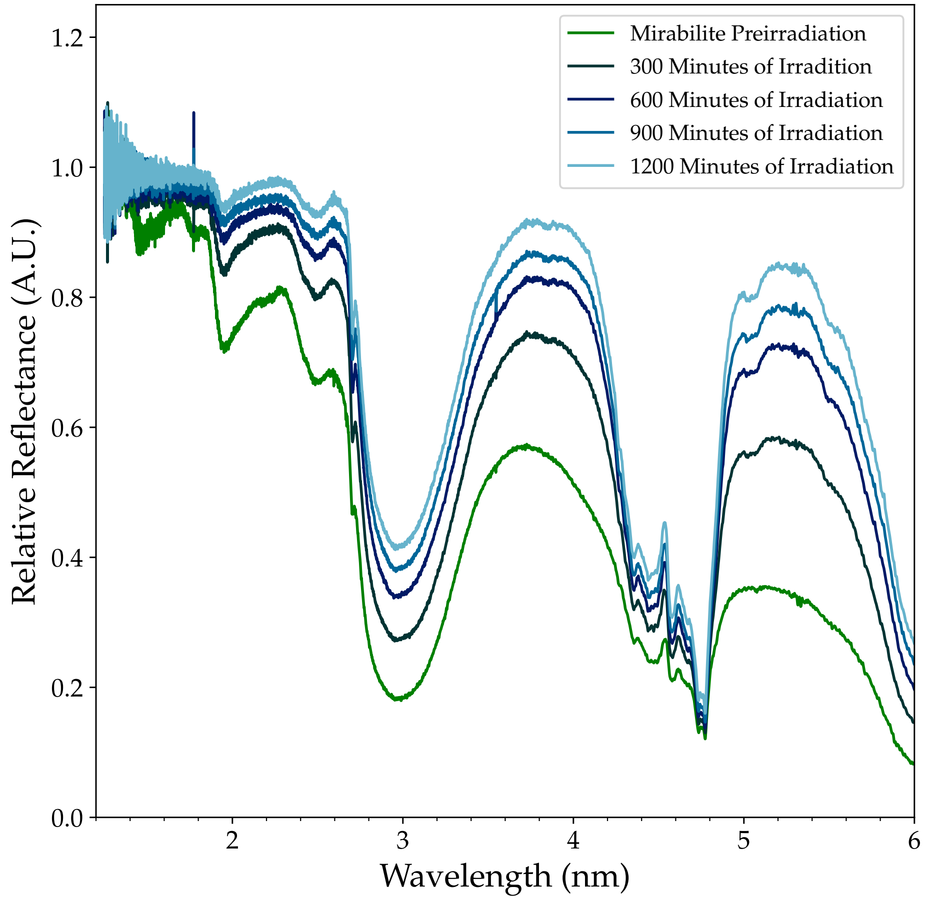

Figure 4.7: Infrared spectra of mirabilite at 100 K with 10 keV electrons. Due to the presence of a hydration feature at the leading edge of the spectra (1.2 µm) normalization, as conducted with thénadrite, was not possible. Dehydration is observed with irradiation but limited other spectral changes are observed.

Epsomite FTIR

Magnesium sulfate heptahydrate presented little change with irradiation in the NIR. It maintained hydration features from 1.2 to 3 µm with irradiation. At Europa, we expect magnesium sulfate to remain hydrated unlike sodium sulfates. There is a systematic shift in the shape of the 3.6 µm feature with irradiation. The maximum remains consistent, but the leading edge changes. This change in leading is a difficult marker to use for spectral identification due to the water band position existing for all hydrated species as well as the large amount of water ice present on Europa. This

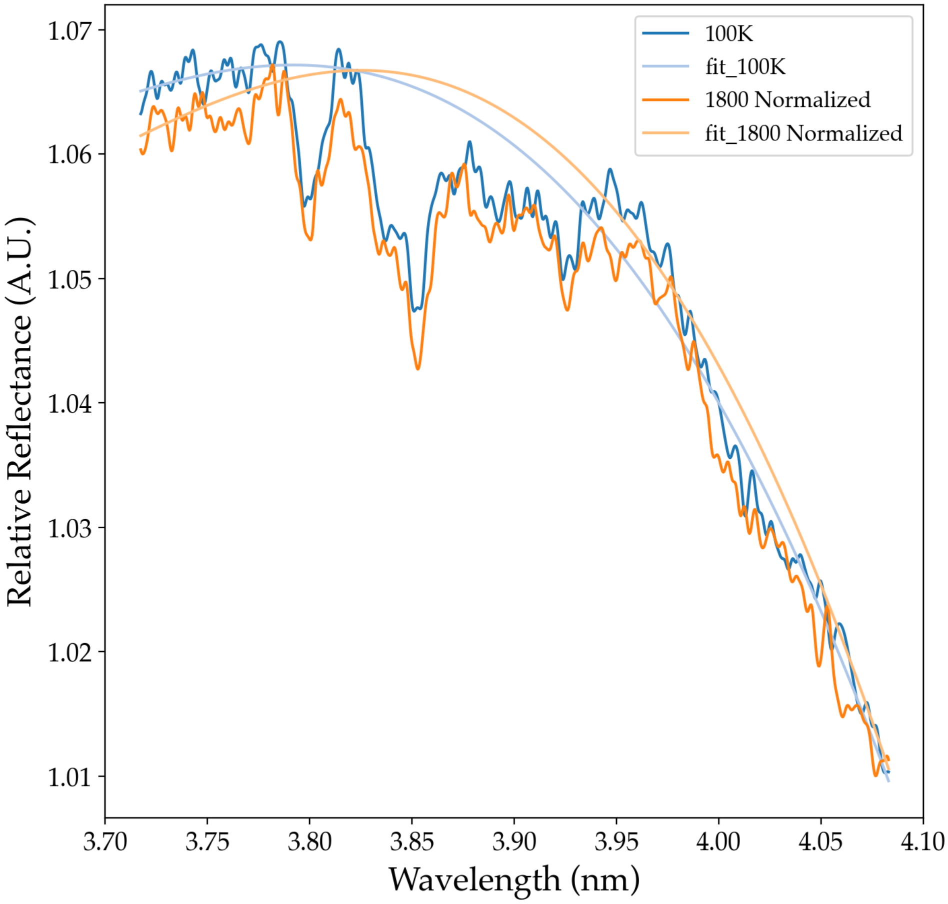

Figure 4.8: Infrared spectra of thénardite with a third order polynomial fit for unirradiated and 1800 minutes of irradiation of thénardite. The 3.8 and 3.85 µm features do not diminish with irradiation.

is most likely due to slight dehydration that is changing the 3 µm absorption. The shoulder absorption at 2.07 µm which has been attributed to magnesium sulfate on Europa is observed in our spectra [10]. This feature remains constant with irradiation, suggesting its presence would remain on Europa.

4.7 Conclusions

This work presents reflectance spectroscopy of sulfate samples, which are suspected to exist on Europa, irradiated at cryogenic conditions. Observational work has suggested the existence of sodium chloride [7] and sulfuric acid [4]. This combination, at

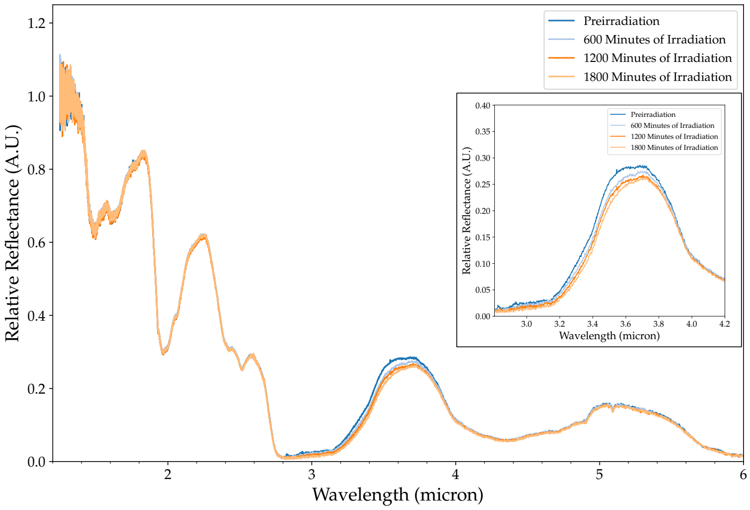

Figure 4.9: Infrared spectra of epsomite irradiated with 10 KeV electrons at 100 K. Spectra is shown for 600 minute timesteps. Insert: Observed change of the 3.7 µm feature with irradiation. The hydration is more tightly bound for epsomite as compared to mirabilite and dehydration does not occur as measured in the 1.2 to 3 µm range.

terrestrial temperatures and pressure, would lead to the formation of sulfate salts. On Europa impingement on the trailing hemisphere from Iogenic sources could provide the requisite energy to create sulfates from endogenic species. The measured spectra from the irradiated sodium and magnesium sulfates exhibited spectroscopic changes in the UV/visible range while presenting limited changes in the IR range. The upturn observed in sodium sulfates, both thénardite and mirabilite, is not seen in observational data of Europa. At very high fluxes, this feature may disappear due to a decrease in reflectivity. The change in spectral slope present in the HST data from figure 4.5 starting at 420 nm has no agreement with the irradiation response in sodium sulfates. Epsomite shows good agreement with the visible data through the visible range but does not exhibit the shoulder centered at 500 nm present on the trailing hemisphere of Europa. In the infrared spectra, thénardite exhibits two features that closely correlates with the observed 3.78 µm feature. The presence of water bands in the hydrated samples as well as the presence of water ice on Europa makes the identification of distinct spectroscopic features difficult. Based on our data we hypothesize that, on Europa, magnesium sulfates could remain hydrated while sodium sulfates would progress to its anhydrous state. This work highlights the need for spectroscopic study of species presumed to be on Europa following their irradiation at cryogenic temperatures, in terms of the large changes observed in the visible spectra. The addition of irradiation of sulfate brines is a key next step. Understanding the spectroscopic features with the inclusion of water ice is paramount for understanding observational data.

References

1. Kargel, J. S. *et al.* Europa's Crust and Ocean: Origin, Composition, and the Prospects for Life. *Icarus* **148,** 226–265. doi:`10.1006/icar.2000.6471` (Nov. 2000).
2. Nelson, R. M. *et al.* Spectral geometric albedos of the Galilean satellites from 0.24 to 0.34 micrometers: Observations with the international ultraviolet explorer. *Icarus* **72,** 358–380. doi:`10.1016/0019-1035(87)90180-1` (Nov. 1987).
3. Paranicas, C., Cooper, J., Garrett, H., Johnson, R. & Sturner, S. Europa's Radiation Environment and Its Effects on the Surface. *Europa* (Jan. 1, 2009).
4. Carlson, R., Anderson, M., Mehlman, R. & Johnson, R. Distribution of hydrate on Europa: Further evidence for sulfuric acid hydrate. *Icarus* **177,** 461–471. doi:`10.1016/j.icarus.2005.03.026` (Oct. 2005).
5. Carlson, R. W. Sulfuric Acid on Europa and the Radiolytic Sulfur Cycle. *Science* **286,** 97–99. doi:`10.1126/science.286.5437.97` (Oct. 1, 1999).
6. Denman, W. T. P., Trumbo, S. K. & Brown, M. E. The Influence of Temperature and Photobleaching on Irradiated Sodium Chloride at Europa-like Conditions. *The Planetary Science Journal* **3,** 26. doi:`10.3847/PSJ/ac4581` (Feb. 1, 2022).
7. Trumbo, S. K., Brown, M. E. & Hand, K. P. Sodium chloride on the surface of Europa. *Science Advances* **5,** eaaw7123. doi:`10.1126/sciadv.aaw7123` (June 2019).
8. Kargel, J. S. Brine volcanism and the interior structures of asteroids and icy satellites. *Icarus* **94,** 368–390. doi:`10.1016/0019-1035(91)90235-L` (Dec. 1991).
9. Fanale, F. P. *et al.* An experimental estimate of Europa's "ocean" composition independent of Galileo orbital remote sensing. *Journal of Geophysical Research: Planets* **106,** 14595–14600. doi:`https://doi.org/10.1029/2000JE001385` (E7 2001).
10. Brown, M. E. & Hand, K. P. SALTS AND RADIATION PRODUCTS ON THE SURFACE OF EUROPA. *The Astronomical Journal* **145,** 110. doi:`10.1088/0004-6256/145/4/110` (Mar. 14, 2013).

11. Trumbo, S. K., Brown, M. E., Fischer, P. D. & Hand, K. P. A New Spectral Feature on the Trailing Hemisphere of Europa at 3.78 *micro* m. *The Astronomical Journal* **153,** 250. doi:`10.3847/1538-3881/aa6d80` (May 11, 2017).
12. Carlson, R., Anderson, M., Johnson, R., Schulman, M. & Yavrouian, A. Sulfuric Acid Production on Europa: The Radiolysis of Sulfur in Water Ice. *Icarus* **157,** 456–463. doi:`10.1006/icar.2002.6858` (June 2002).
13. Carli, C. *et al. VNIR Spectral Change of Hydrated Sulfate Minerals at Different Low Temperatures* in (Mar. 2015).
14. De Angelis, S. *et al.* Temperature-dependent, VIS-NIR reflectance spectroscopy of sodium sulfates. *Icarus* **357,** 114165. doi:`10.1016/j.icarus.2020.114165` (Mar. 2021).
15. Hibbitts, C., Stockstill-Cahill, K., Wing, B. & Paranicas, C. Color centers in salts - Evidence for the presence of sulfates on Europa. *Icarus* **326,** 37–47. doi:`10.1016/j.icarus.2019.02.022` (July 2019).
16. Hibbitts, C., K., S., R. B., W., Shusterman, M. L. & Paranicas, C. *Irradiated Salts and the Color of the Nonice Material on Europa* in *Skating on Thin Ice: Europa and Enceladus* Lunar and Planetary Science XLVIII (Mar. 21, 2017).
17. Elif Genceli, F. *et al.* Meridianiite detected in ice. *Journal of Glaciology* **55,** 117–122. doi:`10.3189/002214309788608921` (2009).
18. Tani, A., Hasegawa, N., Norizawa, K., Yada, T. & Ikeya, M. Radiation-induced radicals in hydrated magnesium sulfate. *Radiation Measurements* **47,** 890–893. doi:`10.1016/j.radmeas.2012.03.006` (Sept. 2012).
19. Trumbo, S. K., Brown, M. E. & Hand, K. P. Endogenic and Exogenic Contributions to Visible-wavelength Spectra of Europa's Trailing Hemisphere. *The Astronomical Journal* **160,** 282. doi:`10.3847/1538-3881/abc34c` (Dec. 1, 2020).
20. De Angelis, S. *et al.* VIS-IR spectroscopy of magnesium chlorides at cryogenic temperatures. *Icarus* **373,** 114756. doi:`10.1016/j.icarus.2021.114756` (Feb. 2022).

Chapter 5

CARBON DIOXIDE EXPERIMENTS

5.1 Observation Data

The addition of observational data from JWST presented a carbon dioxide signal that was not previously observed on Europa [1, 2]. The spectroscopic signal seems to be strongest in the newly resurfaced Tara Regio region. Previous observational data had identified CO_2 on Europa but lacked the spatial resolution to map its distribution [3]. Carbon dioxide has also been observed on two other Galilean satellites, Callisto and Ganymede [4–6]. Unlike on Europa, the CO_2 on Ganymede is associated with dark non-ice material in heavily cratered terrain [4] and on Callisto it is associated with impact craters and has a distribution similar to that of exogenic processes believed to be associated with Jupiter's magnetic field [7, 8]. For CO_2 to be stable at Europa's surface temperatures and pressures, it must be trapped within a host material. This led to the consideration that carbon dioxide is produced uniformly across the surface from exogenic material but trapped more efficiently within chaos terrain. None of the current laboratory trapping methods of CO_2 [9–11] produced similar band position to that of JWST. Since the NaCl present in Tara Regio is not leading to increased trapping, we believe that CO_2 is endogenic to Europa. If CO_2 was externally delivered then the distribution would reflect external implantation, radiation intensity, or a combination of these two processes, not terrain formed via endogenic processing. If carbon dioxide was produced radiolytically from carbonates, an increased C-H stretch would be present in regions of high CO_2 concentrations. Trumbo & Brown [1] were unable to identify any 3.3 to 3.4 µm C-H stretches or 3.4 and 3.9 µm carbonate stretches. The trapped CO_2 would be sputtered from the surface of Europa and would require replenishment from the interior. The ν_3 band shows a doublet with peaks at 4.25 and 4.27 µm. The 4.25 peak implies CO_2 in a trapped form, thus shifting it to a higher frequency. The 4.27 µm is indicative of pure CO_2 ice, which is too volatile to be stable at Europa's surface conditions [1]. This band position does not match expected spectra for CO_2 trapped in amorphous water ice [9] or trapped in clathrates [12]. Absorption onto phyllosilicates produce a ν_3 that is similar to those observed on different satellites but no phyllosilicate minerals have been observed in Europa's salty terrain. On Europa, the 4.25 µm feature is strongest within Tara Regio and across the equatorial latitudes while the 4.27 µm feature is stronger in the northern latitudes. The northern latitudes are colder and possess higher water ice concentrations.

We suspect that there is distinct, unknown trapping mechanism that is producing this observed band splitting. This could be different trapping sites within a single host material similar to what is observed with clathrate trapping [12] or could be two different host materials both trapping CO_2. The carbon is presumed to be endogenic and supplied by the subsurface ocean. Emplacement could occur via a myriad of mechanisms including subsurface upwelling, melt-through, and ice collapse above the subsurface liquid. This would make sense based on the correlation between chaos terrain and the CO_2 feature. Since there is no evidence of additional carbon-bearing material on Europa it is interpreted that the observed CO_2 is delivered to the surface as CO_2. This would require CO_2 to be dissolved in the subsurface ocean and trapped in the upper level of the ice to be visible via observational spectroscopy. This carbon dioxide must be replenished due to loss via sputtering into the atmosphere. This tenuous CO_2 atmosphere would be lost via photoionization and interactions with Jupiter's magnetosphere. These observations of predicted endogenic carbon dioxide trapped in a unknown mechanism led us to design laboratory experiments that mimic the CO_2 conditions present at Europa.

5.2 Experimental Design

The first experimental tests we ran were transmission spectroscopy of thin ice samples. We were hoping to run experiments in the purged nitrogen box of the Nicolet IS50. To run these samples, I designed and 3D printed PLA molds in various shapes to allow for thin ice sheets of uniform thickness. These thin sheets were then mounted horizontally in the sample compartment with the internal IR beam. Unfortunately, the warm nitrogen purge did not allow for the samples to remain intact for long enough to collect consistent spectra. To counteract the warming of the water samples, I developed a liquid nitrogen purge bath to maintain sample integrity. This allowed for longer sample runs but transmission spectroscopy was not possible in this orientation. We were unable to produce thin sheets in a consistent manner that allowed for repeatability.

The next attempt at CO_2 trapping was to create a "Europa in a vial" set up. This design was based on top down freezing with CO_2 diffusing through an ice layer from underneath. A layer of water ice acts like a seal on the vessel while dry ice sublimates below. This has the added combination of creating high CO_2 concentration water ice as well as hopefully trapping CO_2 bubbles within the matrix. I designed and printed various sizes of square vials that would allow for top down freezing of the water. The solubility of CO_2 is 3.2 g/kg of water [13]. Various weight percents ranging from 0.32% (solubility) to 10 % of CO_2 were produced via a Burkle Dry Ice Maker. The dry ice maker creates high purity dry ice pucks from Air Gas tanks. This allows for dry ice on hand at much higher purity than is present with commercial delivery. Dry ice was placed in the bottom of the vessel and millipore water was then added. A metal cup with liquid nitrogen was placed on top of the square vials. This created top down freezing with a high concentration of CO_2 in the water. The CO_2 would bubble and hopefully be trapped in the ice layer. Once all the dry ice had either dissolved or escaped the frozen top layer was removed from the vials and then deposited into copper sample cups for measurement within the PICL UHV chamber. Some samples were ground under a nitrogen environment, while other samples were created by scraping the underside of the frozen water layer. This underside presumably had the highest concentration of CO_2. Other samples were placed in the chamber as sections without grinding. This was to remove the likelihood of CO_2 loss during sample preparation. In conjunction with top down freezing, water and CO_2 samples were prepared in 5 mL sealed vials and then placed in a $-80\,^{\circ}C$ freezer. This slow freezing method would hopefully create a more homogeneous ice sample. These samples were then ground under a nitrogen environment and placed into sample cups. Many of these vials exploded with the sublimation of dry ice which led to poor trapping of CO_2 within the water ice.

To test the our ability to both observe and maintain carbon dioxide within the UHV system, CO_2 ice was tested in the chamber. First, the Burkle Dry Ice Maker was used to make pure dry ice which was placed in the PICL UHV chamber. This spectra was used to test the validity of our thermal control. The chamber was precooled via a closed cycle helium to prevent sublimation of CO_2. A nitrogen purge box was designed and built to remove atmospheric CO_2 and water signals from the spectra. The purge chamber design is highlighted early in this work (2.6) and the PICL UHV chamber with nitrogen box is shown in Figure 2.5. This purge system allowed for less than 1 ppm of atmospheric carbon dioxide to be present in the beam path. This also decreased atmospheric water to allow for finer spectra resolution. We were able to maintain and measure dry ice within our chamber. The CO_2 monitor is able to measure to 1 ppm concentration while the actual levels are lower as shown in Figure 5.1. These experiments presented us with a proof of concept that we could maintain CO_2 in the chamber at vacuum and eliminate atmospheric CO_2 from our spectra.

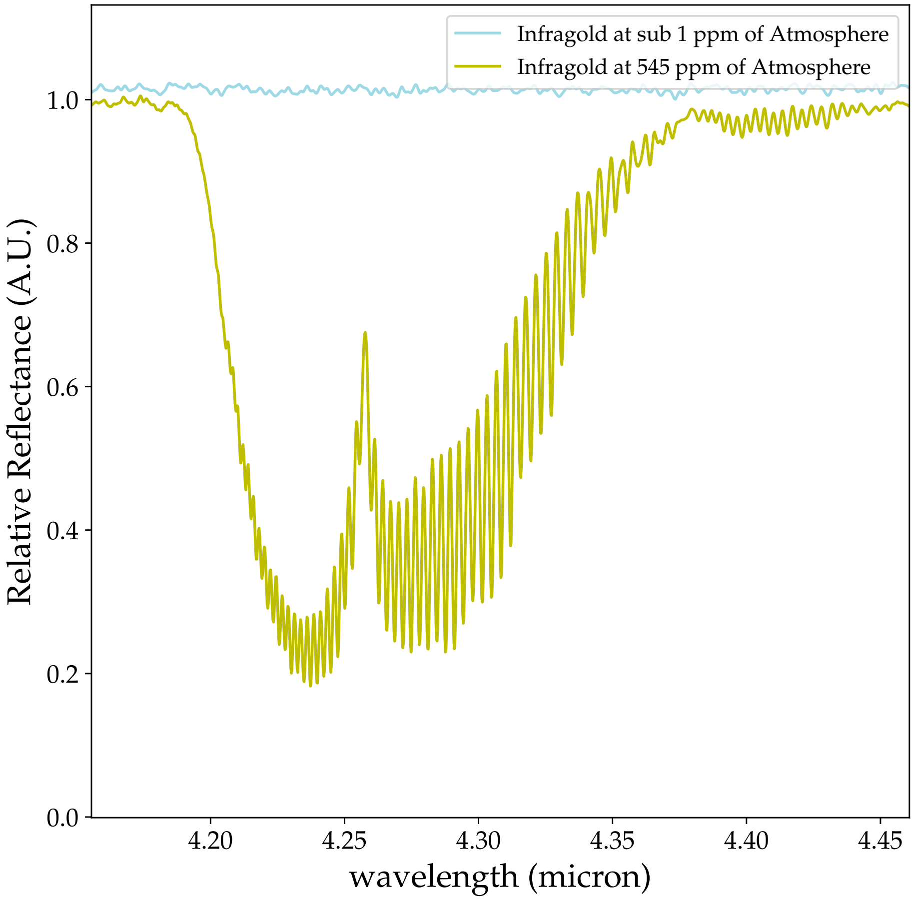

Figure 5.1: Atmospheric CO_2 spectra compared with our nitrogen purge system spectra. The two spectra were taken in the same orientation with the same infragold sample at 293 K.

Our previous attempts at trapping CO_2 in ice samples did not provide a high enough concentration for signal detection in the chamber. Carbon dioxide is unique in the fact that it increases in solubility in water with decreasing temperature. The limited solubility of CO_2 in water is due to its non-polar nature. The trapping of CO_2 is not the same as solubility, while diffusion is a critical aspect in both instances. By utilizing Henry's law previous research was able to show increases of the concentration of CO_2 in water from 1.003 to 1.320 g/L [14]. By increasing the pressure and then flash freezing the system we would be able to increase the concentration and likelihood of CO_2 trapping within our ice matrix. For this experiment, I designed a pressure chamber to increase diffusion. We purchased a custom Parr Instrument's Series 4740 reactor system with 25 mL volume. A CAD drawing is shown in Figure 5.2. Instead of using standard closure systems, a PTFE gasket that could withstand cryogenic temperatures was chosen. The vessel is rated to 3000 psi (204 atm) which is well above previous pressure experiments. Millipore water is placed in the system and then pressurized with CO_2 to 5 atm thus increasing the solubility. The system is then placed in either liquid nitrogen or dry ice as a cooling mechanism. The valves are not rated for temperatures below 235 K so only the reaction vessel is cooled. Liquid nitrogen is closer in temperature, 77K, to the temperatures observed on the Galilean satellites but at 5 atm CO_2 ice would form. At Europa and Ganymede, due to the low pressures, CO_2 ice is unstable which is why a trapping mechanism is needed. Liquid nitrogen does allow for faster freezing which could increase trapping likelihood. With dry ice cooling, we are unlikely to form solid CO_2. At 194 K and 5 atm, solid CO_2 is stable but due to the thermal conductivity of the pressure chamber the dry ice will be colder than the sample temperature. Dry ice submersion cooling will allow for the formation of water ice structure without the formation of CO_2 crystals, thus creating a more similar environment to Europa and Ganymede.

5.3 Future Work

Due to the unique nature of these experiments we will investigate the combination of water ice and carbon dioxide in a series of ways. To test the level of our detection, CO_2 will be mixed with water ice and ground to consistent grain sizes. The weight percent of CO_2 will be varied to set a limit for detection of the standard 4.30 µm CO_2 feature. We do not have the capabilities to do temperature programmed desorption (TPD) but with the recent addition of a residual gas analyzer (RGA) we will be able to measure the decrease in CO_2 within mixture samples. This will be used to set parameters for our CO_2 trapping experiments. The main considerations are what concentration of CO_2 is detectable with our system and at what temperature does CO_2 sublimate within our system. Sublimation can be tested with a combination of changes in pressure for the system as well as utilizing the RGA. For the trapping experiments, two methods for sample preparation exist for these ice samples. The reaction vessel has a diameter which will allow us to place the sample cup directly in the chamber and create the sample during the freezing process. This method increases the expectancy of producing trapped CO_2 and maintaining this CO_2 when transferring it to the chamber for IR spectroscopy. This method is not analogous to icy planetary surfaces because it creates a block of ice as compared to grains. Two methods have been proposed to alleviate this issue. The first is creating the sample and then grinding it at cryogenic temperatures as we have done previously in our laboratory for brine samples. This method allows us to control grain size and then transfer the sample into our sample cups. This method has been effective in maintaining sample integrity with deuterated water samples and brines but the act of grinding may destroy the trapping mechanism for CO_2. Another method for creating surface morphology and creating surface features similar to grains is with electron irradiation. Irradiation creates interstitial holes within the ice structure. This method is more akin to the reactions that occur on the surface of the Galilean satellites but creates other variables within the data. The irradiation of water ice at 16 K produces hydrogen peroxide as well as the irradiation of water ice in the presence of CO_2 at 80 K, hydrogen peroxide was not detected with ion irradiation of water at 80 K [15]. The type of ice created, either amorphous or crystalline, plays a role in the structural change with irradiation. Amorphous water ice undergoes compaction while crystalline ice transformed into amorphous ice at 20K [16]. With electron irradiation we expected changes to our spectra that could be unrelated to the CO_2 trapping. In conjunction with sample preparation the method for heating is critical. The temperature of the sample must be maintained to ensure that the system that is trapping the carbon dioxide is not destroyed. At the pressures of our vacuum chamber, 10^{-7} torr, CO_2 should be stable as a solid to around 75 K [16, 17]. To increase clarity of the mechanisms present with trapping, experiments will be run via two methods. The first method will involve lowering the cryosat temperature to 10K, taking spectra and then doing systematic warming from 10 to 80 K measuring the CO_2 signal at 10 K intervals. A change in spectra should be observed at the around 70K due to a lose of carbon dioxide gas and reveling a shifted carbon dioxide signal. The other method will be kept above 70 K preventing the formation of CO_2

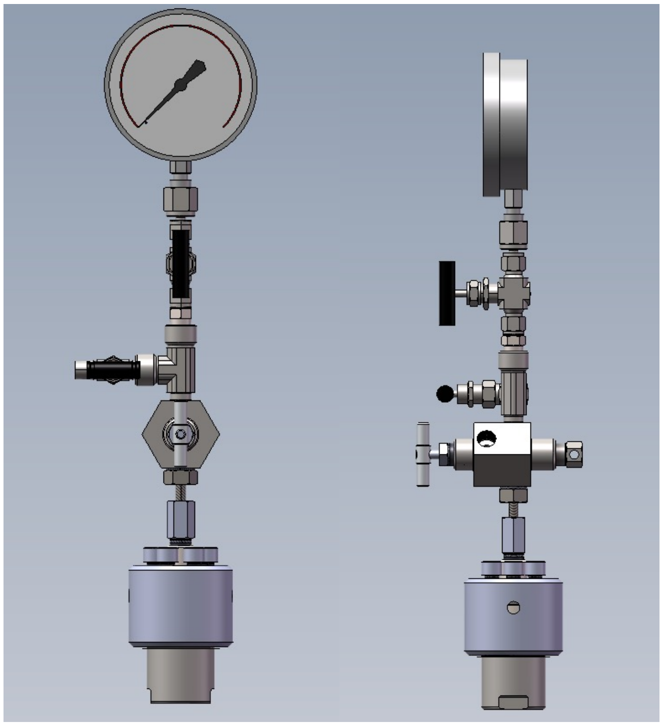

Figure 5.2: Schematic of custom Parr 4740 carbon dioxide pressure vessel.

ice. For this experimental procedure any CO_2 signal would be arise from a trapping mechanism.

These experiments are designed to illuminate the possible mechanism for the shifted signal attributed to carbon dioxides on the icy Galilean moons. There are substantial differences between the CO_2 observed on Europa compared to both Ganymede and Callisto suggesting a different host material. On Iapetus, Saturn's third largest satellite, carbon dioxide has been observed in its dark terrain. The notion of migrating CO_2 has been suggested and modelled allowing for cold trapping in the polar regions [18]. This method of transport and deposition could be visible on Europa. Due to the observations of CO_2 in Tara Regio, which has also been correlated to the presence of irradiated sodium chloride [19], sodium chloride could play a role in trapping of mobile CO_2. The irradiated brine could increase trapping efficiency and stability causing this correlation. This idea is not contrary to the theory of endogenous carbon dioxide to the internal ocean. There is still need for a carbon dioxide source which has not been observed. The role of sodium chloride in the solubility of carbon dioxide and the use of brines for the storage of carbon dioxide has been investigated [20, 21]. These investigations have not been tested at Europa-like environments but offer insight into the feasibility of these trapping mechanisms. The current laboratory set-up of PICL does not offer the capabilities to do irradiation of bulk brine followed by the introduction of a carbon dioxide species. These capabilities may become available with the addition of vapor deposition. Bulk sample properties, compared to thin film, are paramount for trapping experiments.

5.4 Conclusions

This section of the thesis presents new capabilities and an outline for future experiments within the PICL laboratory. The addition of a purge system allows for much higher resolution of water bands and the identification of carbon dioxide features within our samples. The addition of an RGA allows for increased understanding of sample state and finer control of CO_2 concentration. The outlined experiments provide much needed laboratory data for the newly observed carbon dioxide signals on Europa. This research is extremely topical with the immanent launch of Europa Clipper and future observational data from JWST of the other moons within the Galilean system.

References

1. Trumbo, S. K. & Brown, M. E. The distribution of CO $_2$ on Europa indicates an internal source of carbon. *Science* **381,** 1308–1311. doi:`10.1126/science.adg4155` (Sept. 22, 2023).
2. Villanueva, G. L. *et al.* Endogenous CO $_2$ ice mixture on the surface of Europa and no detection of plume activity. *Science* **381,** 1305–1308. doi:`10.1126/science.adg4270` (Sept. 22, 2023).
3. Hansen, G. B. & McCord, T. B. Widespread CO2 and other non-ice compounds on the anti-Jovian and trailing sides of Europa from Galileo/NIMS observations. *Geophysical Research Letters* **35.** doi:`10.1029/2007GL031748` (2008).
4. Hibbitts, C. A., Pappalardo, R. T., Hansen, G. B. & McCord, T. B. Carbon dioxide on Ganymede. *Journal of Geophysical Research: Planets* **108.** doi:`10.1029/2002JE001956` (E5 2003).
5. Hibbitts, C. A., Klemaszewski, J. E., McCord, T. B., Hansen, G. B. & Greeley, R. CO2-rich impact craters on Callisto. *Journal of Geophysical Research: Planets* **107,** 14–1–14–12. doi:`10.1029/2000JE001412` (E10 2002).
6. McCord, T. B. *et al.* Organics and Other Molecules in the Surfaces of Callisto and Ganymede. *Science* **278,** 271–275. doi:`10.1126/science.278.5336.271` (Oct. 10, 1997).

7. Cartwright, R. J. *et al.* Revealing Callisto's Carbon-rich Surface and CO $_2$ Atmosphere with JWST. *The Planetary Science Journal* **5,** 60. doi:`10.3847/PSJ/ad23e6` (Mar. 1, 2024).
8. Hibbitts, C. A., McCord, T. B. & Hansen, G. B. Distributions of CO2 and SO2 on the surface of Callisto. *Journal of Geophysical Research: Planets* **105,** 22541–22557. doi:`10.1029/1999JE001101` (E9 2000).
9. Gálvez, O. *et al.* A study of the interaction of CO$_{\mathsf{2}}$ with water ice. *Astronomy & Astrophysics* **472,** 691–698. doi:`10.1051/0004-6361:20077421` (Sept. 2007).
10. Gerakines, P. A., Schutte, W. A., Greenberg, J. M. & van Dishoeck, E. F. *The Infrared Band Strengths of H2o, Co and Co2 in Laboratory Simulations of Astrophysical Ice Mixtures* Mar. 14, 1995.
11. Hibbitts, C. & Szanyi, J. Physisorption of CO2 on non-ice materials relevant to icy satellites. *Icarus* **191,** 371–380. doi:`10.1016/j.icarus.2007.04.012` (Nov. 1, 2007).
12. Oancea, A. *et al.* Laboratory infrared reflection spectrum of carbon dioxide clathrate hydrates for astrophysical remote sensing applications. *Icarus* **221,** 900–910. doi:`10.1016/j.icarus.2012.09.020` (Nov. 2012).
13. Lucile, F. *et al.* Solubility of Carbon Dioxide in Water and Aqueous Solution Containing Sodium Hydroxide at Temperatures from (293.15 to 393.15) K and Pressure up to 5 MPa: Experimental Measurements. *Journal of Chemical & Engineering Data* **57,** 784–789. doi:`10.1021/je200991x` (Mar. 8, 2012).
14. Mulana, F., Munawar, E., Heldiana, H. & Rahmi, M. The effect of carbon dioxide gas pressure on solubility, density and pH of carbon dioxide – Water mixtures. *Materials Today: Proceedings* **63,** S46–S49. doi:`10.1016/j.matpr.2022.01.033` (2022).
15. Moore, M. IR Detection of H2O2 at 80 K in Ion-Irradiated Laboratory Ices Relevant to Europa. *Icarus* **145,** 282–288. doi:`10.1006/icar.1999.6325` (May 2000).
16. Mifsud, D. V. *et al.* Laboratory experiments on the radiation astrochemistry of water ice phases. *The European Physical Journal D* **76,** 87. doi:`10.1140/epjd/s10053-022-00416-4` (May 2022).
17. Öberg, K. I., Garrod, R. T., van Dishoeck, E. F. & Linnartz, H. Formation rates of complex organics in UV irradiated CH3OH-rich ices I: Experiments. *Astronomy & Astrophysics* **504,** 891–913. doi:`10.1051/0004-6361/200912559` (Sept. 2009).
18. Palmer, E. E. & Brown, R. H. The stability and transport of carbon dioxide on Iapetus. *Icarus* **195,** 434–446. doi:`10.1016/j.icarus.2007.11.020` (May 2008).

19. Trumbo, S. K., Brown, M. E. & Hand, K. P. Sodium chloride on the surface of Europa. *Science Advances* **5,** eaaw7123. doi:`10.1126/sciadv.aaw7123` (June 2019).

20. Moeini, H., Bonyadi, M., Esmaeilzadeh, F. & Rasoolzadeh, A. Experimental study of sodium chloride aqueous solution effect on the kinetic parameters of carbon dioxide hydrate formation in the presence/absence of magnetic field. *Journal of Natural Gas Science and Engineering* **50,** 231–239. doi:`10.1016/j.jngse.2017.12.012` (Feb. 2018).

21. Dziedzic, D., Gross, K. B., Gorski, R. A. & Johnson, J. T. Feasibility Study of Using Brine for Carbon Dioxide Capture and Storage from Fixed Sources. *Journal of the Air & Waste Management Association* **56,** 1631–1641. doi:`10.1080/10473289.2006.10464568` (Dec. 2006).

Chapter 6

GAMMA IRRADIATION ATTEMPTS

The use of gamma irradiation is made possible through collaboration with Sandia National Labs, using a JL Shepard Mark I 68A self-contained Cs-137 irradiator. It is capable of a dosage of 393 R/minute. The gamma irradiation offers much greater penetration depth than 10 keV electrons, and allows for longer exposure times to help replicate the environment of Europa. The unique energy of Cs-137 decay places it in a regime critical to biological samples. In this regime, Compton scattering occurs. Compton scattering is an inelastic interaction of high energy photons with electrons in which the photons transfer a portion of their energy to the charged electrons, causing it to recoil. This is analogous to the photoelectric effect that occurs at lower photon energies. In metals, without a defined band gap, these scattered electrons simply occupy the same conduction band without any discernible change in the materials properties. However, in insulators and semiconductors, with larger band gaps these electrons can be ejected and become trapped. With salt samples, Compton scattering increases the penetration of the radiation. Gamma irradiation offers an interesting method of studying changes with irradiation due to its high energy. Limited research has been done on cryogenic gamma exposure since the majority of work focuses on the storage of nuclear waste [1, 2] or understanding amino acid response with gamma exposure [3–5] though previous work has been conducted on salt samples [6, 7]. While simpler due to natural decay, as compared to electron irradiation, gamma irradiation offers considerable complications. Electronics can not be used in the sample chamber without significant shielding. There is also the additional health risks to researchers. We designed a method to measure the changes of brines predicted on Europa at below terrestrial temperatures with gamma irradiation. Longer term exposure is required to reach similar fluxes to that observed on Europa. Spectroscopy during irradiation is not possible, so UV-Vis spectroscopy with the StellarNet Black Comet will be conducted pre- and post-irradiation. IR spectroscopy will be conducted within our FTIR spectrometer utilizing a Harrick Praying Mantis® diffuse reflective accessory and the Praying Mantis low temperature reaction chamber. This apparatus allows for higher signal as compared to the diffuse reflectivity within the UHV system. It has the capability for nitrogen purge, and can maintain temperatures of 130 K. Sample preparation was conducted similarly to brine perpetration as outlined early within this work 2.7. These samples are cooled utilizing a custom-made cooler closed cycle cooler.

6.1 Cooler Design and Cooling

A custom cooler was needed for insertion into the gamma irradiator. For this design, a wooden mold was constructed and then filled with a 6-lb density polyurethane two-part expanding foam to create a sealed cooler in two parts. This allowed us to fill the inner reservoir with liquid nitrogen and maintain temperature. The foam utilized did not block the gamma emission like a metal cooler would or decay as thermalset insulating plastics would. This custom polyurethane cooler was able to keep liquid nitrogen present for over 6 hours and dry ice for up to 20 hours. This system worked well within the irradiator and no destruction of the cooler was observed with extended gamma exposure. The pitfall for this system was maintaining sample integrity within the cooler. The plastic sample holders, for either brine solutions or biological samples, which are used for other cryogenic applications could not be used due to their reactivity to gamma irradiation. Quartz glass samples were tested to eliminate plastic exposure. To maintain sample integrity, closed vials were purchased. The hope was to be able to seal the vials with the samples and collect the head space and investigating the solids via UV/Vis, Raman, and Infrared spectroscopy. Plastic threaded caps, which are standard for sample control, could not be used. The rubber gaskets tested also failed with exposure to liquid nitrogen temperatures and became brittle when undergoing gamma irradiation. While searching for a method for a closed system, we tested ampules which could be flame sealed and later broken to collect the head space. This method required fine tuning of sample preparations to not introduce thermal shock to the ampules. The samples would need to prepped frozen, placed in the ampules, and kept cold to then be flame sealed and placed back into the freezer. We found that a heated crimp method was faster compared to a roll sealing and decreased handling of the sample. With our sealed vials we were able to now place them into our cooler as individually sealed samples. The samples did not remain submersed in the liquid nitrogen instead floated on the surface due to the head space in the containers. Determining the flux of the samples was not possible due to the variability of gamma flux at different positions. Unfortunately, the thermal shock of introduction to liquid nitrogen even with precooling caused cracking and fracturing of the sealed ampules. This meant we were unable to ensure sample integrity.

After the failure of the submersion system, I set out to design a new way of cooling the samples in the irradiator. Since we do not require liquid nitrogen temperatures but are unable to use electronics within the irradiator, I designed a recirculating chiller system. Instead of using submersion cooling this system relies on an external USA Labs 30 liter −80 °C recirculating ethanol chiller. Ethanol is cooled in a series of copper coils and then pumped to the cooler. Using a closed cycle cooler created a more stable cooling environment as compared to the use of commercial dry ice or liquid nitrogen. This places the cooling system away from the gamma source allowing for monitoring of the system as well. We designed a secondary polyurethane cooler for use with recirculating cooler using ethanol as our submersion liquid instead of liquid nitrogen. This would remove the issue of thermal shock since the temperature difference was 100 K instead of 220 K. To allow for return of the ethanol metal stub pipe fittings were inserted into the polyurethane walls. They were positioned to limit the amount of tubing that was internal to the irradiator. After insertion of metal inlet and outlet tubing destruction of the closed cell foam was observed. The two part foam forms a sealed barrier on the edge of the expansion to create a water and ethanol proof barrier but is not internally closed cell. After the insertion of the stub pipe fitting we were unable to maintain a seal at the lower inlet. This issue led us to rethink the design of our system and remove the element of submersion cooling. I designed and then machined a full metal system using aluminium sheets to construct rigid frame. An opening was cut at the front which fit around the source as to not block any irradiation. Aluminium block with copper recirculating piping were attached to the metal frame for the coolant. The CAD schematic is shown in Figure 6.1 below. This plate design minimized the number length of the copper pipping and used a removable rear panel to access the samples. The copper pipes are soldered together with lead free solder thus eliminating any plastic fittings. An additional cooling plate was placed inside to ensure sample cooling. We used the same ampules as tested before and constructed a turnstile that allowed rotation of the samples. The turnstile allowed for the irradiation of 20 samples at the same dosage for higher through put. The interior of the constructed cooler during thermal testing with turnstile is shown in Figure 6.2. This system was able to maintain temperatures below 240K for water samples while in the gamma irradiator. We were unable to test the temperature of samples during irradiation due to the destruction of the thermal couples when exposed to gamma irradiation.

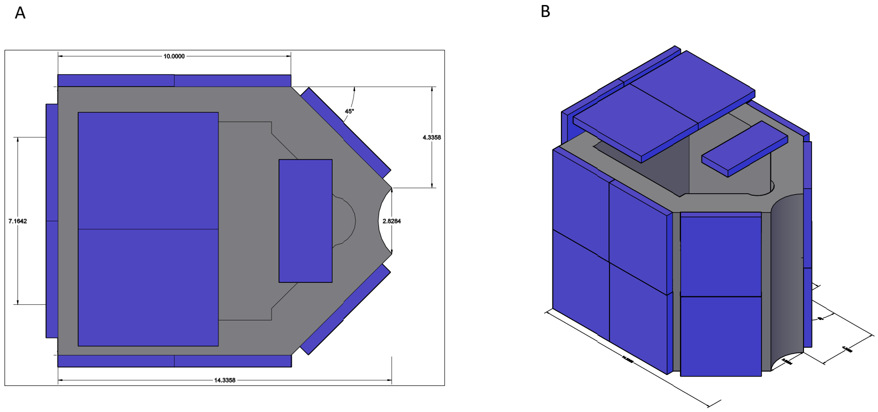

Figure 6.1: Schematic of cooler for gamma irradiation. (A) Top view (B) South East Isometric view. The blue panels represent the closed loop aluminium plates with copper piping. The plates are a standard size which decreased cost of construction.

6.2 Failure of System

As is visible in Figure 6.2 a large amount of frost formed on the cooling system. This was due to the high humidity in the location of the irradiation set up. With our previous polyurethane coolers we did not observe frosting on the outside of the system due to its insulation. No insulation was present for the metal system causing considerable frosting to occur. We attempted to mitigate this by circulating air exterior to the system when it was inside the irradiator but were unable to maintain airflow through the access ports. This long term frosting lead to issues of water forming when warming the system, which would cause oxidation of the interior hinge for irradiator. The ice also causes an expansion of the the cooler. This prevented us from being able to extracted the cooler from the irradiator. Lastly, the cooling caused issues with the actuation of the cesium source. While the pneumatic system is supposedly water-free, frosting occurred on the interior of the pneumatic tube, preventing the source from being raised for irradiation. Due to these complications we were unable to perform gamma cryogenic gamma irradiation.

Possible experimental solutions

In this section, I suggest possible solutions that could alleviate the issues in our gamma irradiation experiments. The simplest is to dehumidifier the irradiation room. By decreasing humidity we can decrease ice formation and hopefully limit the freeze-

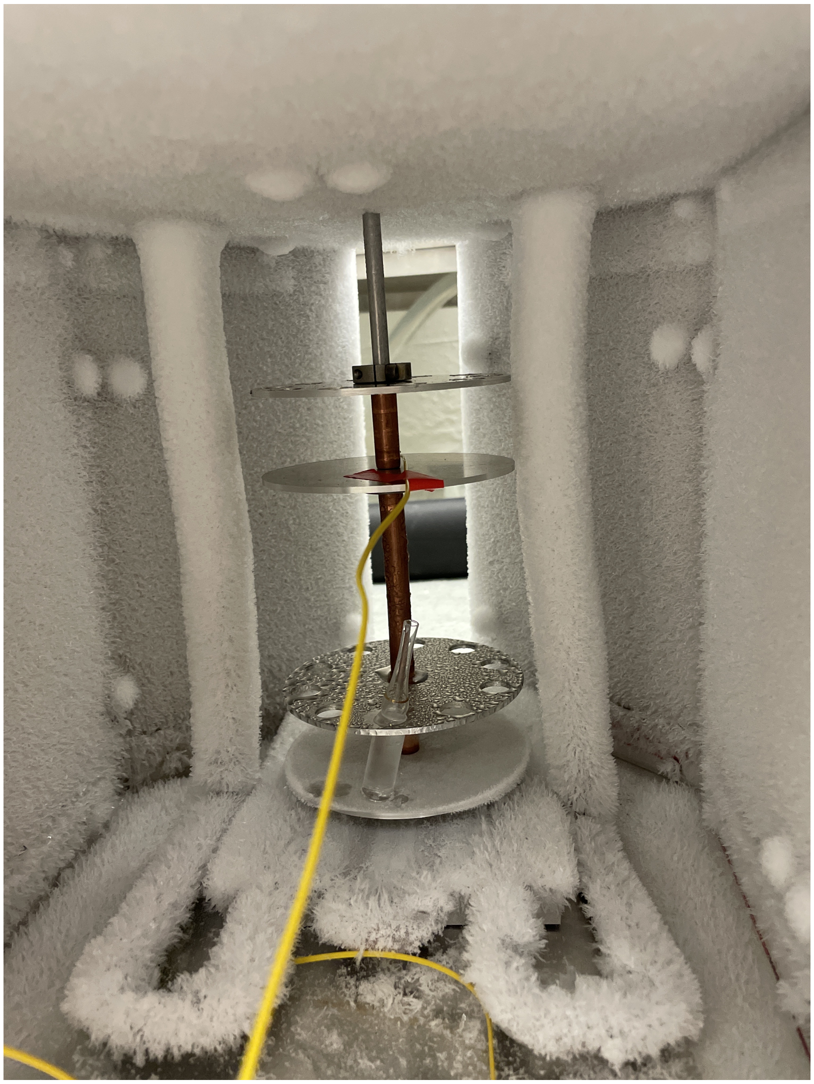

Figure 6.2: Interior of cyrocooler for gamma irradiator under cooling from closed cycle cooler.

thaw issues and water damage. This will not solve the main problem of freezing of the pneumatic source system due to the low water content needed for this issue and positioning of the system. A redesign of the sample cooler is the most economic solution for this system. The recirculating chiller can handle a larger thermal load and alleviates the issue of shock freezing and so should be maintained in the new design. The lack of condensation and thermal insulation provided by the two part polyurethane foam is of significant benefit. The proposed solution is a combination of previous designs. A smaller metal frame work, with different aluminium block with copper recirculating piping to allow for this smaller design with an exterior layer of polyurethane foam, could be used. No interior foam should be used since this will insulate the samples from the aluminium cooling blocks. A smaller turnstile would be needed as well as a method for position repeatability. The source intensity varies greatly with position so location placement is critical. Deterioration of the polyurethane foam could be a factor in this two-part design. The foam would have to be removed and reapplied to provide the same insulation. This redesign and testing is a possible project for an undergraduate researcher or, with the inclusion of long term gamma irradiation studies, a graduate student.

References

1. Daub, K., Zhang, X., Noël, J. & Wren, J. Gamma-radiation-induced corrosion of carbon steel in neutral and mildly basic water at 150 °C. *Corrosion Science* **53,** 11–16. doi:`10.1016/j.corsci.2010.09.048` (Jan. 2011).
2. Litovchenko, V. Y., Vasutin, N. A., Tashlykov, O. L., Kozlov, A. V. & Seleznev, E. N. *Modeling radiation protection of containers for transporting isotopes with high-energy beta irradiation* in. PHYSICS, TECHNOLOGIES AND INNOVATION (PTI-2019): Proceedings of the VI International Young Researchers' Conference (Ekaterinburg, Russia, 2019), 020134. doi:`10.1063/1.5134285`.
3. Kebukawa, Y., Asano, S., Tani, A., Yoda, I. & Kobayashi, K. Gamma-Ray-Induced Amino Acid Formation in Aqueous Small Bodies in the Early Solar System. *ACS Central Science* **8,** 1664–1671. doi:`10.1021/acscentsci.2c00588` (Dec. 28, 2022).
4. Bonales, L. J., Muñoz-Iglesias, V., Prieto-Ballesteros, O. & Mateo-Martí, E. Preservation of glycine coordination compounds under a gamma radiation dose representative of natural mars radioactivity. *Scientific Reports* **12,** 13677. doi:`10.1038/s41598-022-17802-y` (Aug. 11, 2022).
5. Pavlov, A. A. *et al.* Rapid Radiolytic Degradation of Amino Acids in the Martian Shallow Subsurface: Implications for the Search for Extinct Life. *Astrobiology* **22,** 1099–1115. doi:`10.1089/ast.2021.0166` (Sept. 1, 2022).
6. Ramos-Ballesteros, A. *et al.* Gamma radiation-induced defects in KCl, MgCl $_2$, and ZnCl $_2$ salts at room temperature. *Physical Chemistry Chemical Physics* **23,** 10384–10394. doi:`10.1039/D1CP00520K` (2021).
7. Tani, A., Hasegawa, N., Norizawa, K., Yada, T. & Ikeya, M. Radiation-induced radicals in hydrated magnesium sulfate. *Radiation Measurements* **47,** 890–893. doi:`10.1016/j.radmeas.2012.03.006` (Sept. 2012).

Appendix A

LIST OF ABBREVIATIONS

AMU	Atomic Mass Units
CCD	Charge Coupled Device
CF	ConFlat
DLaTGS	Deuterated L-alanine doped Triglycene Sulphate
eV	Electron Volts
FITS	Flexible Image Transport System
FTIR	Fourier Transform InfraRed
HST	Hubble Space Telescope
JWST	James Webb Space Telescope
MCT-A	Mercury Cadmium Telluride
NIMS	Galileo Near Infrared Mapping Spectrometer
OFHC	Oxygen-free high thermal conductivity
PTFE	Polytetrafluoroethylene
RGA	Residual Gas Analyzer
SMA	SubMiniature A
TDP	Temperature Programmed Desorption
UHV	UltraHigh Vacuum
UPS	Uninterupted Power Supply

Appendix B

ELECTRONIC INTEGRATION CODE

```
import tkinter as tk
import lamps
import serial
import time
import numpy as np

def uvlamp():
        lswitch=[1,0]
        ls=lamps.get_lamp_status()
        print(ls)
        ls[0]=lswitch[ls[0]]
        lamps.change_lamp_status(ls)
        uvbut.configure(bg=lcolors[ls[0]])
        print(lcolors[ls[0]],ls)

def vislamp():
        lswitch=[1,0]
        ls=lamps.get_lamp_status()
        print(ls)
        ls[1]=lswitch[ls[1]]
        lamps.change_lamp_status(ls)
        visbut.configure(bg=lcolors[ls[1]])
        print(lcolors[ls[1]],ls)

def bye():
        lamps.change_lamp_status([0,0])
        root.destroy()

def DelayCounter():
    global temperature,pressure
```

```
    #ask for the temperature
    tempcont.write(b’KRDG? B \r \n’)
    t=tempcont.readline()
    temperature.set(t)

    #ask for the vacuum
    s=’0280323234300033837’
    vac.write(bytes.fromhex(s)+b’\r \n’)
    v=vac.readline()
    p=float(v[5:13])
    pressure.set(p)

    #get something about the gun. Just the name, for now. energy,
        soure V
    gun.write(b’gmn\r\n’)
    g=gun.readline()
    g=g[5:len(g)-2]

    # maybe turn the pressure red or something.
    # and don’t let anyone turn the gun on.
    if pressure.get()>pressurelimit:
        print(’WARNING: OVER PRESSURE. TURNING OFF EGUN’)
        gun.write(b’sdn\r\n’)

    root.after(10000,DelayCounter) # do it again in 10 second


import serial
import time
#open the temperature controller serial port
tempcont=serial.Serial(’COM4’,57600,serial.SEVENBITS,serial.PARITY_ODD
    ,serial.STOPBITS_ONE,timeout=2)

#open the vacuum serial port
vac=serial.Serial(’COM5’,9600,serial.EIGHTBITS,serial.PARITY_NONE,
    serial.STOPBITS_ONE,timeout=2)

#open the gun
```

```
gun=serial.Serial(’COM8’,19200,serial.EIGHTBITS,serial.PARITY_NONE,
    serial.STOPBITS_ONE,timeout=2)


pressurelimit=1.e-6 # this is the failsafe limit!!!
ls=lamps.get_lamp_status()
print(ls)
lcolors=[’red’,’green’]

##############################
root=tk.Tk()
root.title(’control panel’)
frame1=tk.Frame(root,padx=1,pady=1)
frame2=tk.Frame(root,padx=1,pady=1)
frame3=tk.Frame(root,padx=1,pady=1)

frame1.grid(row=0,column=0)
frame2.grid(row=1,column=0)
frame3.grid(row=0,column=1)



#Frame 1, lamp buttons
uvbut=tk.Button(frame1,text=’UV lamp’,command=uvlamp,bg=lcolors[ls
    [0]])
uvbut.grid(row=0,column=0)
visbut=tk.Button(frame1,text=’vis lamp’,command=vislamp,bg=lcolors[ls
    [1]])
visbut.grid(row=0,column=1)


#Frame 2, death
tk.Button(frame2,text=’KILL ME NOW (lamps off)’,command=bye,bg=’blue’)
    .grid()

#Frame 3, vac,temp,e-gun readouts

tk.Label(frame3,text=’pressure:’).grid(row=0,column=0)
```

```
pressure=tk.DoubleVar()
plab=tk.Label(frame3,textvariable=pressure)
pressure.set(1000.)
plab.grid(row=0,column=1)

tk.Label(frame3,text='temp:').grid(row=1,column=0)
temperature=tk.DoubleVar()
tlab=tk.Label(frame3,textvariable=temperature)
temperature.set(300.)
tlab.grid(row=1,column=1)

#set up delay counter
DelayCounter()

root.mainloop()
```